NASA
Technical
Paper
2588

1987

Comparison of Wind Tunnel and Flight Test Afterbody and Nozzle Pressures for a Twin-Jet Fighter Aircraft at Transonic Speeds

Jack Nugent
Ames Research Center
Dryden Flight Research Facility
Edwards, California

Odis C. Pendergraft, Jr.
Langley Research Center
Hampton, Virginia

CONTENTS

SUMMARY

Afterbody and nozzle pressures measured on a 1/12-scale model and in flight on a twin-jet fighter aircraft were compared as Mach number varied from 0.6 to 1.2, Reynolds number varied from 17.5 million to 302.5 million, and angle of attack varied from 1° to 7°.

At Mach 0.6 and 0.8, nozzle pressure coefficient distributions and nozzle axial force coefficients agreed and showed good recompression.

At Mach 0.9 and 1.2, flow complexity caused a loss in recompression for both flight and wind tunnel nozzle data. The flight data exhibited less negative values of pressure coefficient and lower axial force coefficients than did the wind tunnel data. Reynolds number effects were noted only at these Mach numbers. Jet temperature and mass flux ratio did not affect the comparisons of nozzle axial force coefficient.

At subsonic speeds, the levels of pressure coefficient distributions on the upper fuselage and lower nacelle surfaces for flight were less negative than those for the model.

The model boundary layer thickness at the aft rake station exceeded that for the forward rake station and increased with increasing angle of attack. The flight boundary layer thickness at the aft rake station was less than that for the forward rake station and decreased with increasing angle of attack.

INTRODUCTION

Integrating a propulsion system into a new twin-jet fighter aircraft continues to require extensive development efforts. Blending the inlets and nozzles with the airframe frequently creates flow interferences not amenable to analytical prediction and for which experimental data may be lacking. In the nozzle-afterbody region, several factors contribute to flow interference. They include close proximity of the nozzles, afterbody, and tails. Variable geometry and sensitivity of the local flows to Mach number, Reynolds number, angle of attack, and the hot jet efflux are additional factors. Similar flow complexities exist in the inlet forebody region. Accordingly, experimental research programs are necessary to acquire a better understanding of propulsion system and airframe flow interference.

To improve the technology base for future fighter aircraft and to acquire a better understanding of propulsion system and airframe flow interference, the U.S. Air Force and NASA have completed an experimental program involving wind tunnel tests using subscale F-15 airplane models and flight tests with the full-scale F-15 airplane. The objective was to create data bases from which comparisons of wind tunnel and flight test data could be made. Reference 1 presents selected results of the overall program, and reference 2 presents a comparison of measurements made in the inlet airframe region.

For the nozzle-afterbody region, wind tunnel tests were conducted at the NASA Langley Research Center using a propulsion model, and flight tests were conducted at the Dryden Flight Research Facility of the NASA Ames Research Center. The tests were carefully coordinated so that the test configurations, instrumentation locations, and test conditions of the model and aircraft were as similar as possible. This was done to reduce differences in the test results that could be attributed to these factors. References 3 to 7 present results from the model and flight tests of the nozzle and afterbody region that were previously obtained from this program. Tests were also conducted in a water tunnel using a separate flow visualization model to provide additional test data.

The purpose of this report is to compare and analyze model and flight data obtained for the nozzle and afterbody

regions of the F-15 airplane. These data include surface pressures on the aft fuselage and nozzle, boundary layer surveys on the upper nacelles, and flow visualization on the upper fuselage. Excluding the low-speed water tunnel tests, the Mach number range of the correlation extended from 0.6 to 1.2 over an angle-of-attack range of 1° to 7°. The test Reynolds number range extended from 17.5 million for the propulsion model to 302.5 million in flight, based on the length of the fuselage. Sideslip angle was essentially zero.

To provide a range of test values, several nozzle boattail angles were included in the comparison. At subsonic speeds, the largest boattail angle was a nominal 18.4°, corresponding to the dry or military power throttle setting and the smallest opening at the nozzle exit. Also included was a nominal boattail angle of 15.1°, corresponding to a low afterburning throttle setting and a larger nozzle opening. At Mach number $M = 1.2$, the boattail angle was a nominal 7.7°, corresponding to a higher afterburning throttle setting and a still larger nozzle opening. Nozzle pressure ratio varied from unity (jet off) to about 7. The effects of the major test variables on each comparison were systematically investigated and analyzed.

NOMENCLATURE

A_n projected area in the axial direction assigned to each of the 42 nozzle surface pressures, cm^2

BTL   boattail chord angle of the left nozzle for airplane, or terminal boattail angle for model, deg

BTR   boattail chord angle of the right nozzle for airplane, or terminal boattail angle for model, deg

C   constant

C_a left nozzle axial force coefficient referenced to wing area,

$$\sum_{n=1}^{42} \frac{(C_p \times A_n)}{S_w}$$

C_p pressure coefficient,

$$\frac{P - P_\infty}{q_\infty}$$

C_p* pressure coefficient at sonic speed,

$$\frac{0.7547 \left(1 + 0.2M_\infty^2\right)^{3.5} - 1.4286}{M_\infty^2}$$

$C_{p_{avg}}$ average value of pressure coefficient, for either first or last nozzle orifice

F.S.   fuselage station, cm

H   height of boundary layer rake probe above fuselage surface, cm

H_p pressure altitude, geopotential, m

L_a distance from airplane nose to end of tailboom, 19.05 m

L_m distance from model nose to end of tailboom, 158.689 cm

M   Mach number in boundary layer at height H

MFRA   ratio of jet mass flux to free-stream mass flux, airplane

MFRM   ratio of jet mass flux to free-stream mass flux, model

M_∞ free-stream Mach number; in this report, also assumed to be the Mach number at the edge of the boundary layer

NPRL	left nozzle total pressure divided by P_∞	T_{t_∞}	total temperature in the free stream, K
P	surface static pressure, N/cm^2	U	local velocity in the boundary layer at height H, m/sec
P_i	pitot pressure in boundary layer at height H, N/cm^2	U_∞	free-stream velocity; in this report, also assumed to be the local velocity in the boundary layer at a given boundary layer thickness δ, m/sec
P_∞	free-stream static pressure, N/cm^2		
P_{t_i}	total pressure in the boundary layer at height H, N/cm^2	X	distance from airplane nose, m, and distance from model nose, cm
P_{t_∞}	free-stream total pressure, N/cm^2	X/L	nondimensional distance from nose for the airplane (X/L_a) and the model (X/L_m)
P_i/P_{t_∞}	pitot pressure ratio in the boundary layer at height H, N/cm^2	Y	transverse distance from airplane plane of symmetry, m, and distance from model plane of symmetry, cm
q_∞	free-stream dynamic pressure, N/cm^2		
R	gas constant	Y/L	nondimensional transverse distance from fuselage plane of symmetry for the airplane (Y/L_a) and for the model (Y/L_m)
Re	Reynolds number		
Re_a	Reynolds number for airplane, based on L_a	α	angle of attack, deg
Re_m	Reynolds number for model, based on L_m	γ	ratio of specific heats
		Δ	incremental change
S_w	wing area (airplane, 55.839 m^2; model, 0.3923 m^2)	ΔC_p	a measure of average recompression on the external surface of the nozzle
T	static temperature in boundary layer at height H, K		
T_a	total temperature of jet exhaust, airplane, K	δ	boundary layer thickness, cm
T_m	total temperature of jet exhaust, model, K	ϕ	circumferential angle around the left nozzle measured clockwise when viewed from the rear, deg
T_∞	static temperature in free stream; in this report, also assumed to be the static temperature at the edge of the boundary layer, K		

DESCRIPTION OF APPARATUS

16-Foot Transonic Wind Tunnel

Wind tunnel tests compared in this report were conducted in the NASA Langley 16-Foot Transonic Wind Tunnel, which is

3

a single-return, continuous-flow, atmospheric wind tunnel with a slotted octagonal test section measuring 4.8 m diametrically to midflat centerline. With the aid of a compressor system, which draws air out through slots in the test section for Mach numbers greater than 1.05, the test section airspeed is continuously variable from subsonic speeds up to Mach 1.3. Additional details of the wind tunnel and its operation are given in reference 8.

Propulsion Model

Figure 1 is a photograph of the 1/12-scale F-15 aircraft propulsion model mounted on a strut in the NASA Langley 16-Foot Transonic Wind Tunnel, and figure 2 shows geometric details of the model. Room-temperature air at high pressure was used to simulate the jet exhaust. The air was ducted through the support strut, routed internally in the model, and exhausted through the test nozzles. There was no inlet flow through the model; fairings were placed on the model where the inlets were normally located on the airplane. The model was tested with and without a noseboom, afterburner fuel vent fairings, nozzle flap actuator fairings, and a 0.127-cm step upstream of each nozzle simulating the engine bay vent on the airplane. The model contained a six-component afterbody balance that measured the net force and moment on all surfaces downstream of the metric break (fig. 2), including the afterbody, test nozzles, and tail surfaces.

Figure 3 is a photograph illustrating afterbody details and the dry, or military, power nozzles. The afterbody consists of closely spaced nozzles, widely spaced tailbooms, and large vertical and horizontal tail surfaces. A wedge-shaped interfairing is located between the two nozzles. The wedge has a 20° included angle and terminates close to the exit plane of the nozzle. The development of this configuration is discussed in reference 9. Additional

details of the model are given in references 3 and 7.

Figure 4 shows geometric details of the three test nozzles used in the correlation: the military power nozzle (fig. 4(a)) with a terminal boattail angle of 18.4° and the two partial afterburning power nozzles with terminal boattail angles of 15.1° (fig. 4(b)) and 7.7° (fig. 4(c)). The internal geometry and area ratio of these nozzles simulated those for the full-scale nozzles.

F-15 Airplane

The F-15 is an air-superiority fighter airplane capable of transonic cruise and supersonic dash to speeds greater than Mach 2. Distinguishing airplane features include a high-mounted sweptback wing, twin vertical stabilizers, and a large horizontal stabilator. A photograph and a three-view drawing of the airplane are shown in figures 5 and 6, respectively. The variable-geometry inlets use horizontal ramps mounted at the wing level. Each inlet is automatically controlled using independent controllers; however, the left inlet was manually controllable in the test airplane.

The powerplants for the F-15 airplane are two prototype Pratt and Whitney F100-PW-100 engines that are twin-spool, afterburning turbofans in the 110,000-N thrust class. Both the fan and the compressor use variable geometry for high performance and distortion attenuation. The nominal bypass ratio is approximately 0.7 for military (maximum nonaugmented) power at sea-level, standard-day conditions. The engine controls consist of a hydromechanical unit and a supervisory digital control unit.

Figure 7 is a rear-view photograph of the F-15 airplane. Exhaust nozzles are variable geometry with a convergent-divergent internal flow path. To vary the nozzle geometry, the engine control continuously maintains a scheduled rela-

tionship between the throat area and the ratio of the exit area to the throat area. Nozzle surfaces consist of variable flaps and seals that slide in a circumferential direction to maintain a circular internal path at the throat and exit as the geometry is varied.

Details of the nozzle geometry are shown in figure 8. The three-dimensional fuselage surface ends at nondimensional distance $X/L = 0.886$. Aft of this station, the exposed nozzle is axisymmetric. The nozzle is fixed geometry forward of $X/L = 0.900$ where the terminal angle is $13.2°$. Nozzle geometry varies with power setting downstream of $X/L = 0.900$. This variation results in a discrete change in nozzle external shape at $X/L = 0.900$. The nozzle boattail angle ranges from about $18.4°$ at military power to about $1°$ to $2°$ with full afterburning power. In determining the nozzle boattail angle, the nozzle flaps are assumed to be straight lines. Additional F-15 airplane details are given in reference 6.

Comparison of Propulsion Model and Airplane

Although the overall program was closely coordinated, there were some unavoidable differences between the propulsion model and the airplane. Figure 9 compares the model and airplane inlets. For the model (fig. 9(a)), the inlet was replaced with a fairing that extended forward on the forebody. Figures 9(b) and 9(c) show one of the airplane's inlets and its external variable geometry, which consisted of a variable-angle cowl and a two-position bypass door. The model inlet simulated an undeflected cowl; therefore, as shown in figure 9(c), flight tests were made with the cowl aligned with the nacelle surface and with the bypass door closed.

Photographs of the engine compartment vent on the airplane and its simulation on the model are shown in figure 10. The model simulated the rearward-facing step created by the vent but did not simulate the flow exiting from the vent and flowing downstream over the nozzle. As previously mentioned, the model jets simulated the airplane's hot jet exhaust with room-temperature air.

Figure 11 compares the airplane and model nozzle external surfaces. The wind tunnel model nozzles were smoothly machined, whereas the airplane nozzle had variable flaps and seals. The flaps and seals resulted in gaps near the trailing edge that varied with nozzle boattail angle.

Flow Visualization Model

Because the differences in the inlet configurations of the propulsion model and airplane were thought to affect the boundary layer profiles on the upper fuselage, a flow visualization study was conducted. The 1/48-scale flow visualization model of the F-15 airplane used in reference 10 was suitably modified to simulate the propulsion model and the airplane. Figure 12(a) shows the faired-inlet configuration, and figure 12(b) shows the flowing-inlet configuration. With the inlet fairing installed, there was no internal flow. The model was equipped with surface orifices through which various colored dyes were ejected from inside the model to flow downstream over the fuselage surface, thus illustrating the flow patterns.

INSTRUMENTATION

Figure 13 shows the locations of the surface pressure orifices on the upper and lower fuselage of the model and airplane. The locations are shown in terms of nondimensional distances X/L, measured downstream from the nose, and Y/L, measured from the plane of symmetry. Table 1 lists the locations in tabular form and shows the good agreement between the model and airplane for surface pressure orifice locations. Note that on the upper nacelle, the airplane had four more orifices than the model. These were installed for the companion inlet-airframe interactions program (ref. 2).

Figure 13(a) also shows the locations of the boundary layer rake on each of the upper nacelles. Drawings and photographs of the model and airplane rakes shown in figure 14 display differences in the rake configurations. The model rakes (figs. 14(a) and 14(b)) used five pitot tubes, with the uppermost pitot tube of each rake about 2.5 cm above the model surface. This value scales to about 30.0 cm (when multiplied by 12) to compare with the airplane rakes. Heights of the individual pitot tubes varied slightly between the two model rakes. The airplane rakes (figs. 14(c) and 14(d)) used 10 pitot tubes, with the uppermost tube 38.4 cm above the airplane surface. The model rakes used a tube that measured static pressure at the top of the rake; the tube was lacking on the airplane rake.

Figure 15 shows the angular locations of the eight rows of surface pressure orifices on the left nozzles of the model and airplane. The axial locations, in terms of X/L, of the 42 pressure orifices are given in table 2 for each of the angular rows. The model and airplane orifice locations show excellent agreement.

In addition to the fuselage, boundary layer, and nozzle pressures, numerous other parameters were measured during the model and flight tests. For the model tests, these included the free-stream parameters, horizontal tail deflection, and jet nozzle parameters. For the flight tests, free-stream parameters, surface deflections, inlet parameters, and engine parameters were measured. A detailed discussion of these measurements is presented in references 3, 6, and 7.

TESTS

Propulsion Model Tests

Two test series were planned and conducted to obtain pressure distributions for the model data base. The first series conducted before the flight tests yielded a matrix of Mach number and angle-of-attack test points using several test nozzles. These were to be matched during the flight tests. The test points were attempted in flight, but several could not be flown because of q limitations and the inability to stabilize the airplane transonically because of excess thrust at the partial afterburning power settings.

Following the flight tests, the second model test series was conducted. In this series the exact test points that were flown were duplicated in the tunnel using smaller nozzles. In addition, a noseboom was added and other model changes were made to better match the airplane configuration. The data from these tests were used in the comparison presented in this paper.

Model data were taken at Mach 0.60, 0.80, 0.87, 0.90, and 1.2. Data were obtained with the boundary layer rakes mounted and removed. Model angle of attack varied from -2° to 7°. The ratio of jet total pressure to free-stream static pressure was varied from 1, jet off, to about 7. Horizontal tail or stabilator angle varied from 2.5° to -4.0° leading edge down. For the comparison, data at horizontal tail angle settings of -2°, 0°, and 2° were used. Reynolds number varied from 17.5 million to 21 million for the Mach number range tested. Force and moment data were not obtained. Additional test information is given in references 3 and 7.

Flight Tests

Although the Mach number range for this comparison is 0.60 to 1.2, the flight test Mach number range extended from 0.60 to 2.0 (ref. 6). The flight tests were conducted to obtain quasi-steady-state data to match the model data. To aid the pilot in stabilizing on a test point, in-flight measurements of airplane parameters were transmitted in real time by way of a telemetry down-link to the ground-station computer. Ground-computed parameters in real time

were uplinked to the pilot's console, allowing him to make rapid corrections to his flightpath and thus stabilize on the desired test point. This technique proved successful in stabilizing Mach number, altitude, angle of attack, and angle of sideslip at the desired values. Details of this technique are given in reference 11.

To achieve a variation in Reynolds number, nominal test altitudes of 6100, 10,700, and 13,700 m were flown. As shown in figure 16, the flight test Reynolds number range for the data presented herein extended from less than 80 million to 302.5 million. Comparing the Reynolds number test ranges for model and flight reveals the large range in Reynolds number that existed for the comparison.

The boattail angle of the instrumented left nozzle was calculated in real time in the ground-station computer using the downlinked measurement of the nozzle throat area. This value was then up-linked to a pilot display. The relation between boattail angle and throat area was obtained from a ground calibration prior to the flight tests. For each test point, the pilot set the left nozzle boattail angle by adjusting the throttle and observing his display. Figure 17 shows typical variations of test values of the left nozzle boattail angle as a function of Mach number. The four boattail angles are identified by the horizontal lines designated as 18.4°, 14.6°, 9.5°, and 7.7°. From a free-stream Mach number M_∞ of 0.6 to 1.2, with a boattail chord angle BTL of 18.4°, 14.6°, and 7.7°, the data show the pilot was able to set the boattail angle to within ±0.5° of the target values the majority of the time.

In most cases the right engine power settings, and hence the nozzle boattail angle, closely matched those for the left engine. Although the nozzle pressure ratio was systematically varied in the wind tunnel tests, this was not possible for the flight tests. The ratio was generally fixed by the test point. Figure 18, obtained from reference 6, shows a typical variation of left nozzle total pressure (NPRL) with M_∞ for a number of test points. The data represent several boattail angles.

The left inlet cowl was set to 0° and the bypass door closed to simulate the faired-inlet configuration of the model. However, the right cowl and bypass door were in the automatic control mode, subjecting the upper fuselage flow field to slight geometric asymmetry.

In flying the test points, the stabilator and rudders were varied as required. The average stabilator position varied from 2.1° leading edge up to 3.2° leading edge down, and the average rudder trailing edge position varied from 2.5° airplane nose right to 1.4° airplane nose left.

Water Tunnel Tests

The flow visualization model was tested in the water tunnel described in reference 10. The purpose of the tests was to identify similarities and differences in the flow patterns on the upper fuselage caused by the difference in inlet configurations. Colored dye was ejected from orifices on the forebody, nacelle, and wing leading edges to create flow patterns that were photographed under steady test conditions. The angle of attack extended from 0° to 10°, and the angle of sideslip was 0°. The test Reynolds number was 40,000, based on the length of the model.

DATA REDUCTION

Axial Force Coefficient

All data presented in this report were obtained during stabilized test conditions. Surface pressures were reduced to pressure coefficients C_p.

To determine nozzle axial force coefficient, each of the 42 orifices was assigned the appropriate aft-facing projected area predetermined from a nozzle calibration. This area varied with the nozzle boattail angle. The axial force coefficient was obtained by summing the 42 products of the local area and the pressure coefficient and then dividing that sum by the wing area.

Boundary Layer Profiles

Profiles of pitot pressure ratio were obtained from the boundary layer rakes. Individual pitot pressures were divided by the respective free-stream total pressure P_{t_∞} from model or flight test, and the ratios were plotted as a function of pitot tube position. To compare model and flight data, the pitot tube positions for the model rake were multiplied by 12 because the model was 1/12-scale size. Both sets of data were compared with a reference boundary layer profile. This reference profile was calculated using the boundary layer thickness obtained from the flight test condition and an assumed turbulent velocity distribution. The derivation of the expression for this profile is given in the appendix.

Boundary layer thicknesses for the flight data were obtained from velocity ratio profiles as discussed in reference 6. For the model, the thicknesses were obtained by inspecting the profiles

of pitot pressure ratio since the instrumentation was insufficient to calculate velocity ratio profiles.

Nozzle Pressure Ratio

For the model, nozzle pressure ratio was obtained by dividing the measured nozzle entrance pressure by free-stream static pressure P_∞. For the airplane, the appropriate F100-PW-100 engine status deck was used to obtain nozzle entrance pressure as well as other engine parameters. These were obtained as a function of Mach number, pressure altitude, and power setting for a given test point.

Additional discussion of the data reduction procedures is given in references 3, 5, and 6.

UNCERTAINTY

Model

Accuracies of several parameters obtained in the wind tunnel tests were determined by the root-sum-square method for combining errors from independent sources. The errors are given in the table below.

Airplane

Reference 6 presents a detailed discussion and analysis of the estimated errors for the measured and calculated

Parameter	M_∞			
	0.60	0.80	0.90	1.2
	Standard deviation error			
M_∞	±0.0017	±0.0016	±0.0016	±0.0019
C_a	±0.00009	±0.00006	±0.00005	±0.00004
C_p	±0.009	±0.006	±0.006	±0.004
P_∞, N/cm^2	±0.001	±0.0006	±0.0005	±0.0003
q_∞, N/cm^2	±0.0014	±0.0014	±0.0014	±0.0016

quantities in flight. The results of this analysis are summarized in figure 19, which is a plot of the left nozzle C_p and left nozzle axial force coefficient (C_a) errors as functions of free-stream dynamic pressure q_∞. Both errors show a strong dependency on q_∞. The errors corresponding to four nominal test points are shown on each error curve. The highest errors occur at low q_∞, corresponding to low M_∞ at the higher altitudes (for example, $M_\infty = 0.6$ at 10,700 m). Conversely, the lowest errors occur at high q_∞, corresponding to flight at high M_∞ at the lower altitudes (for example, $M_\infty = 0.9$ at 6,000 m). For these latter conditions, the error in C_p is less than 0.015, while the error in C_a remains less than 0.0001. These errors approach the model errors.

RESULTS AND DISCUSSION

Presentation of Results

The results in this paper are presented as follows: comparisons of afterbody pressure coefficient distributions, boundary layer profiles and thicknesses, and flow visualization. These are followed by comparisons of afterbody and nozzle pressure coefficient distributions, pressure coefficient distributions on the nozzle external surface, recompression on the nozzle, and nozzle axial force.

To analyze the effects of the several test variables on the comparisons, the data were organized and plotted so that only one test variable changed while the other test variables were relatively constant. Similarities and differences between the model and flight data, therefore, became functions of the particular test variable that changed. The test variables analyzed in this way were Mach number, angle of attack, left nozzle boattail angle and pressure ratio, and Reynolds number.

The test conditions for the model and flight data are presented in table 3 for surface pressures and in table 4 for boundary layer profiles. Table 5 lists the pitot pressure ratios from the boundary layer tests. Table 6 lists the several boundary layer thicknesses for the flight boundary layer profiles presented. Table 7 lists the data figures, content of the figures, and the test conditions selected from tables 3 and 4 used in each of the figures. Table 7 aids in relating the plotted and tabulated data.

Pressure coefficient distributions on the external surfaces of the afterbody and nozzle are plotted against X/L. Except for model test points 21 to 25 of table 3, these data were obtained with the boundry layer rakes removed. As indicated in reference 7, the addition of the boundary layer rakes generally did not change the surface pressure distributions on the left afterbody and nozzle.

Comparison of Afterbody Pressure Coefficient Distributions

Afterbody pressure coefficient distributions from model and flight were analyzed and interpreted. The local flow fields were then classified as being either compression or expansion fields. The compression or expansion was caused by interference flows from nearby surfaces as well as the local surface curvature. In figure 20, the flow field classifications are shown, along with the adjacent vehicle components influencing them. On the upper fuselage, the upstream expansion field (fig. 20(a)) is believed to be influenced by the forward portion of the wing. Farther downstream, the observed compression field, as interpreted, illustrates the effects of the nacelle curvature and wing trailing edge shock waves. In the afterbody and nozzle region, either an expansion-recompression or an expansion field is indicated. Interference effects from the tail surfaces, tailboom, nozzle interfairings, afterbody boattailing, and variable-

geometry nozzles all influence the complex flow effects observed. Figure 20(b) shows a similar interpretation for the lower fuselage.

Effect of Mach Number

The effect of Mach number on the comparison of afterbody pressure coefficient distributions is shown in figure 21. Data are presented at angle of attack $\alpha \approx 1°$ for BTL $\approx 18.4°$ at subsonic speeds and for BTL $\approx 7.7°$ at $M_\infty \approx 1.2$ for an NPRL test range of 2.0 to 5.0.

In figure 21(a) the afterbody pressure coefficient distributions for $M_\infty \approx 0.6$ and $\alpha \approx 1°$ may be used to illustrate the interpretations discussed in figures 20(a) and 20(b). Thus for the upper fuselage in figure 21(a), both sets of data are similar and show the expansion and compression regions between $X/L = 0.456$ and $X/L = 0.684$. These are followed by the expansion and subsequent recompression to near ambient pressure downstream of $X/L = 0.900$.

The upper nacelle data are similar to the upper fuselage data downstream of $X/L = 0.530$ with the negative gradients steeper for flight. The greater steepness is believed to be due to the closer proximity, and therefore stronger influence, of the expansion field of the leading edge of the vertical tail. The flow field for the upper left tailboom shows a steep recompression to near ambient pressure at the last orifice. This is believed to be influenced by the compression field of the trailing edge of the vertical tail.

The lower fuselage distributions for model and flight illustrate the expansion-recompression field downstream of $X/L = 0.684$. For the lower nacelle, both sets of data also show a compression followed by an expansion. The fuel dump vent at $X/L = 0.800$ causes only a slight effect on the pressure distributions.

In figure 21(b), at $M_\infty \approx 0.8$, the overall pressure distribution trends for both sets of data resemble those at $M_\infty \approx 0.6$. On all three upper surfaces, the reductions in C_p for stations downstream of $X/L \approx 0.800$ are probably due to compressibility effects caused by the increase in free-stream Mach number from $M_\infty \approx 0.6$ to $M_\infty \approx 0.8$.

On the lower surfaces, the model data exhibit minimal change from the data at $M_\infty \approx 0.6$. The flight data exhibit slightly more negative values of C_p than for $M_\infty \approx 0.6$ at all values of X/L. On the lower nacelle, flow losses caused by the fuel dump vent for both sets of data are increased compared to those at $M_\infty \approx 0.6$.

In figure 21(c), as Mach number increases to $M_\infty \approx 0.9$, compressibility effects on the pressure coefficient distributions are more pronounced. Local Mach numbers become supersonic over the upper nacelle and tailboom because the local flow expansions reduce the C_p levels below the pressure coefficient at sonic speed (C_p^*). The model data do not become as negative as the flight data. The sharp rises in C_p at $X/L \approx 0.870$ on the upper tailboom are attributed to standing shock waves recompressing the flow; this may be partially caused by the compression field of the vertical tail. The rise for the flight data exceeds the rise for the model data, suggesting a higher local Mach number immediately preceding the shock wave for the airplane than for the model.

On the lower fuselage at $M_\infty \approx 0.9$, the flight data exhibit a loss of recompression beyond $X/L \approx 0.800$. Other changes for both sets of data are minimal except for the flow losses caused by the fuel dump vent, which increase from those at $M_\infty \approx 0.8$.

At $M_\infty \approx 1.2$ (fig. 21(d)) both sets of upper fuselage and upper nacelle data display steeper gradients in C_p relative to $M_\infty \approx 0.9$. The gradients induced by flow expansion and compression are increased; those caused by compression are probably intensified by standing local shock waves. On the upper tailboom the standing shock wave evident at $M_\infty \approx 0.9$ has disappeared.

On the lower surfaces, both sets of data also demonstrate steep gradients similar to those on the upper surfaces. On the lower fuselage, the flow accelerates downstream of $X/L = 0.684$, causing large reductions in C_p. The expansion for the flight data exceeds that for the model data.

Effect of Angle of Attack

The effect of angle of attack on the comparison of afterbody pressure coefficient distributions for $M_\infty \approx 0.8$ is shown in figure 22. Data are presented for angles of attack of 1°, 3°, 5°, and 7° (figs. 22(a) to 22(d), respectively), at BTL $\approx$ 18.4°, and with NPRL ranging from 2.5 to 3.7. The increase in angle of attack from 1° to 7° produced the following results. On the upper fuselage and nacelle the shapes of the pressure coefficient distributions for the model and flight data do not change significantly. Upstream of $X/L = 0.800$, the level of C_p decreases with increasing angle of attack; downstream of $X/L = 0.800$, a minimal change is noted. On the upper tailboom, the effect of the angle-of-attack change is small.

For the lower nacelle, the level of C_p increases slightly upstream of $X/L = 0.700$ for both sets of data. For the flight data on the lower fuselage, increasing the angle of attack slightly increases the level of pressure coefficient upstream of $X/L = 0.800$. Simultaneously, the aftmost C_p level is reduced from positive values to negative values.

Effect of Left Nozzle Boattail Angle

Figure 23 presents the effects of an increase in the left nozzle boattail angle on afterbody pressure coefficient distributions for an angle-of-attack range of 1° to 2° and an NPRL range of 2.5 to 5.0. In figures 23(a) and 23(b), data are shown for $M_\infty \approx 0.6$, illustrating BTL values of 15.1° and 18.4°, respectively. Changes in C_p level are minimal at locations immediately upstream of the nozzle. In figures 23(c) and 23(d), BTL values of 15.1° and 18.4°, respectively, are presented for $M_\infty \approx 0.9$. The effects of the boattail angle change are minimal at locations immediately upstream of the nozzle.

Summary

The effects of the test variables on the comparison of pressure coefficient distribution on the afterbody surfaces are summarized as follows. The C_p patterns for model and flight data are similar over the Mach number test range. On the upper surfaces and the lower nacelle at subsonic speeds, the flight values of C_p are generally less negative than those of the model. The effects of the variations in angle of attack and boattail angle on the level and trend of afterbody pressure coefficient distributions are generally small.

Comparison of Boundary Layer Profiles and Thicknesses

The effects of Mach number and angle of attack on the comparison of pitot pressure ratios, boundary layer profiles, and boundary layer thicknesses were determined and are shown in figures 24 and 25. Data are presented for several boattail angles in military and partial afterburning power and an NPRL range of 2.0 to 5.0. For the model data, the measured heights of the pitot tubes were multiplied by 12 to compare them with the

flight data. Also shown in these figures is the reference turbulent boundary layer profile; its height is the boundary layer thickness measured in flight.

Effect of Mach Number

The effect of Mach number on boundary layer profiles and thicknesses for an angle of attack of approximately 3° is shown in figure 24. At the forward rake location (fig. 24(a)) and at $M_\infty \approx 0.6$, the model, flight, and reference turbulent profiles agree closely. As Mach number increases, there is increasing disagreement between the three curves. At $M_\infty \approx 0.8$ and 0.9, the model data display higher pitot pressure ratios than either the flight data or the reference profile, except near the fuselage surface. At $M_\infty \approx 1.2$ the model profile undergoes a dramatic loss in pitot pressure ratio relative to the flight and reference profiles. The model boundary layer thickness is insensitive to Mach number at subsonic speeds and increases at $M_\infty \approx 1.2$.

As shown in the flight data in figure 24(a), an increase in M_∞ causes an increased loss in the pitot pressure ratio in the boundary layer $\left(P_i/P_{t_\infty}\right)$ relative to a reference turbulent profile, particularly near the surface. This result suggests flow losses near the surface in excess of those attributable to a turbulent boundary layer. The flight boundary thicknesses are relatively insensitive to Mach number.

At the aft rake location (fig. 24(b)), the model levels of P_i/P_{t_∞} exhibit a greater sensitivity to Mach number than was the case at the forward rake. The model profiles have the lowest levels of P_i/P_{t_∞} relative to the flight and turbulent profiles for all test Mach numbers and show an increasing departure from a turbulent shape as M_∞ increases from 0.6 to 1.2. The trend of P_i/P_{t_∞} above 24 cm

shows that interference effects from the fuselage flow field are negligible at $M_\infty \approx 0.6$ and increase slightly as M_∞ increases from 0.8 to 1.2. The flight pitot pressure profiles have a turbulent boundary layer shape and display an increasing loss relative to the reference turbulent profiles with an increase in Mach number. The thicknesses for the model data do not change as Mach number is increased. The flight data display a small decrease in thickness as Mach number is increased. The model data thickness exceeds that for flight at all Mach numbers.

Effect of Angle of Attack

Figure 25 presents the effect of angle of attack on boundary layer profiles and thickness for $M_\infty \approx 0.8$. In figure 25(a), at the forward rake location, profiles for model and flight show reasonable agreement with the reference turbulent profile as angle of attack increases from 1° to 7°. At $\alpha \approx 7°$, interference from the fuselage flow field reduces P_i/P_{t_∞} above a height of 24 cm for the flight data (ref. 6). Boundary layer thickness for the model is constant with increasing angle of attack, but the thickness for flight decreases with increasing angle of attack above 3°. At an angle of attack of 7°, the thickness for the flight is less than the model thickness.

As shown in figure 25(b), both sets of data indicate that angle-of-attack effects on the aft rake exceed those on the forward rake. As angle of attack increases, the model profiles increasingly fall below the reference turbulent and flight profiles. This indicates flow losses near the model surface exceeding those for a turbulent boundary layer. With increasing angle of attack, boundary layer thickness increases markedly for the model. The flight profiles have a turbulent shape and agree with the reference profiles throughout the angle-

of-attack range. Interference effects from the fuselage are noted at $\alpha \approx 3°$ and 7°, and thickness decreases as angle of attack increases from 3° to 7°. Reference 6 presents additional data on boundary layer thickness measured in flight.

Summary

Mach number and angle of attack affected the model boundary layer profiles and thicknesses more than for the flight profiles and thicknesses at both rake stations. For the model, an increase in Mach number reduced P_i/Pt_∞ near the fuselage surface for both rakes. An increase in angle of attack had a similar effect on the aft rake. The boundary layer thickness at the aft rake station exceeded that for the forward rake station and increased markedly with angle of attack.

For the flight data, an increase in Mach number reduced the level of P_i/Pt_∞ for both rakes, but the effect was less than that for the model data. An increase in angle of attack from 3° to 7° reduced boundary layer thickness for both rakes, an effect opposite of that for the model. Boundary layer thickness at the aft rake station was less than that for the forward rake station and, relative to scale, was considerably less than the boundary layer thickness at the aft rake station on the model.

Flow Visualization

An insight into the flow behavior on the fuselage upper surface can be obtained by examining the flow visualization photographs obtained from the water tunnel tests. Figures 26 and 27 show plan and side views of the flowing-inlet and faired-inlet configurations, respectively, photographed in the water tunnel at angles of attack of 1°, 3°, and 7°. The flow patterns are illustrated by the paths traced by the dye streams as they flow downstream over the model surfaces.

As indicated on the figures, the dye ports are located on the upper cowl, the juncture of the wing and the glove, the forward portion of the inlet fairing, and the forebody. A dye port is located at each of the boundary layer rake locations. The dye streams issuing from the boundary layer rake locations are useful in interpreting flow direction at the forward and aft boundary layer rake locations.

For the flowing-inlet configuration, which is similar to that of the airplane (figs. 26(a) to 26(c)), increasing the angle of attack causes an increase in spanwise wing flow outboard near the wing trailing edge. This is evident immediately ahead of the flow channel created by the twin vertical tails. An examination of the side views indicates that the spanwise wing flow lifts upward from the wing surface with increasing angle of attack (figs. 26(d) to 26(f)).

The dye stream issuing from the location of the forward rake initially shows an outboard flow direction (figs. 26(a) to 26(c)). Farther downstream between the two vertical tails the flow is deflected into a streamwise direction. Finally, near the nozzle, the flow exhibits a sharp change in flow direction outboard and downward. This trend is duplicated at the location of the aft rake. Another factor that may influence the flow pattern between the vertical tails is flow that propagates downstream from the boundary layer diverter, the gap located between the inlet and the forebody.

It is believed that the boundary layer at the forward rake location is reduced in thickness by the increasing spanwise wing flow with increasing angle of attack. At the aft rake location the additional reduction in boundary layer thickness may be caused by the large

increase in outboard and downward flow as angle of attack is increased.

For the faired-inlet configuration (figs. 27(a) to 27(c)), which is similar to the propulsion model, the effect of an increase in angle of attack on the spanwise wing flow differs from the flowing-inlet configuration. Although the flow patterns are similar at $\alpha \approx 1°$ (figs. 26(a) and 27(a)), they begin to differ at $\alpha \approx 3°$ (figs. 26(b) and 27(b)). For the faired-inlet configuration, the flow in the outboard direction begins to break down as noted by the inboard streamlines on each wing. At $\alpha \approx 7°$ (fig. 27(c)), the spanwise flow is reversed and flows inboard toward the channel created by the vertical tails. Examining the side views (figs. 27(d) to 27(f)), the flow on top of the fuselage at $\alpha \approx 7°$ (fig. 27(f)) appears to be separating from the surface, which could result in a boundary layer having low energy.

Corresponding changes in flow direction are noted at the dye streams originating at the locations of the boundary layer rakes. At $\alpha \approx 1°$ (fig. 27(a)), the dye streams are flowing directly downstream. At $\alpha \approx 3°$ (fig. 27(b)), the flow changes to an inboard direction, particularly at the aft rake. Finally, at $\alpha \approx 7°$ (fig. 27(c)), the flow shows a strong inboard flow direction for both dye streams.

For the faired-inlet configuration, it is believed that the thickening of the boundary layer at the aft rake with increasing angle of attack is influenced by the wing flow. As angle of attack increases, the wing flow near the trailing edge reverses from a generally outboard direction to an inboard direction. The flow is channeled by the vertical tails toward the center of the airplane and the nozzles. The general flow direction between the vertical tails is inboard, as opposed to outboard for the flowing-inlet configuration. This apparently thickens the boundary layer. A

vortex shed from the leading edge of the inlet fairing may also contribute to the flow pattern between the two vertical tails.

Comparison of Afterbody and Nozzle Pressure Coefficient Distributions

As shown in figure 20, flow interactions between nacelle and nozzle can influence the pressure coefficient distributions obtained from model and flight tests. Figure 28 illustrates several possible variations in pressure coefficient distribution. Curve 1 shows that the flow expanding over the afterbody reaches a minimum level upstream of the afterbody and nozzle juncture. The subsequent pressure rise downstream of the juncture to a positive value of C_p illustrates good recompression and attached flow.

Curve 2 is the same as curve 1 except for the downstream nozzle flow. The decrease in slope and lack of recompression suggests flow separation. Note that the loss in pressure is due entirely to flow over the nozzle and not to any change in the upstream flow.

Curve 3 illustrates a lower minimum pressure than curves 1 and 2, followed by a sharp pressure jump. The sharp jump indicates a standing compression shock wave. Following the shock wave, the flow separates in a manner similar to curve 2. Note that downstream of the separation point the level of C_p for curve 3 may lie below that for curve 2 because of the lower value of C_p immediately ahead of the separation point. Consequently, the large loss in C_p from curve 1 to curve 3 is due to an upstream influence as well as flow losses on the nozzle.

Effect of Mach Number

The effect of Mach number on the comparison of afterbody and nozzle pressure coefficient distributions at $\alpha \approx 1°$ is shown in figure 29. Data are presented

14

for an NPRL test range of 2.0 to 5.0 at BTL $\approx$ 18.4° for subsonic speeds and BTL $\approx$ 7.7° at $M_{\infty} \approx$ 1.2.

Figure 29(a) presents data for $M_{\infty} \approx$ 0.6, BTL $\approx$ 18.4°, and NPRL $\approx$ 2.0 to 3.0. Data are presented for the upper nacelle and nozzle row 350° and for the lower nacelle and nozzle row 182°. Note the break in the X/L axis and the scale increase for the nozzle pressure distribution. This allows a more detailed examination of the variation in C_p on the nozzle. The data at X/L = 0.897 (the first nozzle pressure orifice) appear on both sides of the plots for the flight data and for nozzle row 182° for the model data.

The pressure distributions shown for the upper and lower surfaces illustrate the example of curve 1 in figure 28, namely, good recompression to positive levels of C_p on the downstream portion of the nozzle. As previously discussed, on the nacelle surfaces the C_p level for the flight data is greater than that for the model, that is, the values of C_p are less negative. The difference in the fuselage vent configurations between model and flight may be contributing to the lower pressure coefficients immediately upstream of the nozzle for the model. As discussed in reference 6, when the vent gap was sealed to prevent outflow, the pressure coefficients on the first and second nozzle orifices were reduced. This nonflowing vent configuration was simulated on the model.

Despite the slightly larger levels of C_p at X/L greater than 0.850 shown by the flight data on the nacelle surfaces, the recompression processes on both nozzle rows are very similar for both sets of data. The flight data exhibit slightly higher values.

As Mach number increases to 0.8 (fig. 29(b)) the trends are similar to those shown in figure 29(a). At

X/L = 0.897 on nozzle row 182°, the flight value of C_p exceeds that for the model, although recompression is similar for both sets of data. On the upper nacelle the recompression for the model is slightly more efficient, yielding a slightly greater value of C_p at X/L = 0.937 than for flight.

For a Mach number of 0.9 (fig. 29(c)), both sets of data indicate that the difference in levels of C_p for both nozzle rows exceeds that at $M_{\infty} \approx$ 0.8. On the upper nacelle the flight data exhibit a standing shock wave immediately ahead of the nozzle. Downstream of the shock wave there is a large loss in recompression compared to that at $M_{\infty} \approx$ 0.8; this loss is attributed to flow separation. The amount of recompression does not differ greatly between model and flight; that is, the distributions are roughly parallel. As a result, the difference in C_p existing at upstream nozzle locations remains about the same everywhere along the nozzle.

Similar results are evident on the lower nacelle and nozzle. The recompression at $M_{\infty} \approx$ 0.9 is about the same for model and flight. The flight data are less negative than the model data at X/L = 0.897 and remain this way as X/L increases; that is, the distributions are roughly parallel. Therefore, it would appear that the differences in the pressure distributions are caused by upstream influences.

At $M_{\infty} \approx$ 1.2 (fig. 29(d)), recompression deteriorates on both nozzle surfaces for the model and flight data. The flight data indicate that a standing shock wave is located downstream of the first nozzle orifice, that is, downstream of the juncture between the fixed and movable nozzles. This is indicated by the sharp rise in C_p. The model data also show this result for nozzle row 182°. The flow separates downstream of this orifice for model and flight because of the shock

wave. The level of C_p for flight is less negative than for the model downstream of the juncture on both surfaces. The average level of C_p on the lower nozzle surface is less negative than the average level of C_p on the upper nozzle surface for both sets of data.

Effect of Angle of Attack

The effect of angle of attack on the comparison of afterbody nozzle pressure coefficient distributions at $M_\infty \approx 0.8$ is presented in figure 30 for angles of attack of 1°, 3°, 5°, and 6° to 7°. The overall effects of angle of attack on recompression on the upper and lower surfaces are small for both sets of data.

Effect of Left Nozzle Boattail Angle

The effect of left nozzle boattail angle on the comparison of afterbody nozzle pressure coefficient distributions is illustrated in figure 31 for an angle-of-attack range of 1° to 2° and an NPRL range of 2.5 to 5.0. Figures 31(a) and 31(b) present data at $M_\infty \approx 0.6$ for nominal boattail angles of 15.1° and 18.4°, respectively. On nozzle row 350°, for both sets of data, a loss in recovery (that is, a decrease in slope) is noted for X/L greater than 0.920 as boattail angle is increased.

Figures 31(c) and 31(d) show corresponding data at $M_\infty \approx 0.9$. A decrease in slope is shown for both nozzle rows because of the boattail angle increase. The loss in recompression is larger for nozzle row 350° than it is for nozzle row 182°.

Summary

The effects of the test variables on the comparisons of afterbody nozzle pressure coefficient distributions are summarized as follows. Flight C_p levels

on the upstream nozzle orifices were generally less negative than those for the model because of the upstream nacelle flow. For both model and flight data at $M_\infty \approx 0.6$ and 0.8, good recompression existed for nozzle rows 182° and 350°. At $M_\infty \approx 0.9$ and 1.2, recompression deteriorated because of flow separation and flow complexity. The upstream differences in the C_p levels between model and flight were retained along both nozzle surfaces. These results demonstrate upstream influences on the nozzle pressures. At $M_\infty \approx 0.6$ and 0.9, increasing boattail angle reduced the recompression at both nozzle rows, but the effect was larger at nozzle row 350°. The effects of angle of attack were small.

Comparison of Pressure Coefficient Distributions on the Nozzle External Surface

The effects of the test variables on all eight rows of the surface pressure orifices of the nozzles are discussed in the following sections.

Effect of Mach Number

Figure 32 shows the effect of Mach number on nozzle pressure coefficient distributions for the eight nozzle rows. Data are presented at $\alpha \approx 1°$ for an NPRL range of 2.0 to 5.0, for BTL $\approx 18.4°$ and BTL $\approx 7.7°$. For $M_\infty \approx 0.6$ (fig. 32(a)), the pressure coefficient distributions for both sets of data agree reasonably well. Highest recompression is at the bottom rows (for example, rows 230°, 182°, and 134°) and the top rows (302° and 350°). For the model, row 86° appears to be separated. The value of C_p is positive for all eight rows at the last orifice. Where data are available at X/L = 0.897, C_p for flight exceeds C_p for the model except for the separated row. This is attributed to upstream effects.

At $M_\infty \approx 0.8$ (fig. 32(b)), model and flight data exhibit a slight loss of recompression compared with $M_\infty \approx 0.6$ on all rows; agreement is good. At all rows for both sets of data, the value of C_p at the last orifice is smaller than at $M_\infty \approx 0.6$. At row 86°, both sets of data indicate separation.

At $M_\infty \approx 0.9$ (fig. 32(c)), the pressure coefficient distributions show a significant loss of recompression for both sets of data (except for row 182°). The flat profiles for several of the rows suggest an increasing amount of separated flow on the nozzle surface. The model and flight C_p profiles appear to be almost parallel rather than coincident, which was the case at $M_\infty = 0.8$. Row 182° shows a positive value of C_p at $X/L = 0.931$; the values of C_p for all other rows at $X/L = 0.931$ are either zero or negative.

At $M_\infty \approx 1.2$ (fig. 32(d)), the pressure coefficient distributions for both sets of data at all rows exhibit larger negative C_p levels, as well as increased flow complexity relative to the subsonic data (figs. 32(a), (b), and (c)). At all rows, the profiles for the flight data are less negative than those for the model data. Row 182° reveals a standing shock wave and shock-induced separation for both model and flight.

Effect of Angle of Attack

The effect of angle of attack on the comparison of nozzle pressure coefficient distributions is shown in figure 33 for angles of attack of 1°, 3°, 5°, and 6° to 7°. The model and flight data show reasonable agreement in level and trend for all angles of attack. The angle-of-attack variation has minimal effect on both sets of data.

Effect of Left Nozzle Boattail Angle

Figure 34 displays the effect of left nozzle boattail angle on the comparison of nozzle pressure coefficient distribution for an angle-of-attack range of 1° to 2° and an NPRL range of 2.5 to 5.0. Figures 34(a) and 34(b) present data at $M_\infty \approx 0.6$ for nominal boattail angles of 15.1° and 18.4°, respectively. The profiles indicate that overall recompression is reduced as the boattail angle is increased at all nozzle rows except 182° and 230°. For the flight data in figures 34(c) and 34(d), for $M_\infty \approx 0.9$, the results also display a loss in recompression as the boattail angle is increased as well as an increasing tendency toward separation.

Summary

The effects of the test variables on the comparisons of pressure coefficient distributions on the nozzle external surface are summarized as follows. At $M_\infty \approx 0.6$ and 0.8, there was reasonably good agreement between the model and flight in level and trend. At $M_\infty \approx 0.9$ and 1.2, both sets of data showed increasing evidence of flow separation, flow complexity, and a loss in recompression. The trends exhibited by the model and flight data were the same, but the flight data exhibited less negative levels of C_p than the model on all the nozzle rows. This is attributed to upstream effects. Increasing left nozzle boattail angle generally caused losses in recompression for all rows, except rows 182° and 230°. The effects of angle of attack on the data were minimal.

Comparison of Recompression on the Nozzle External Surface

The comparison of recompression on the nozzle external surface and the

effects of Mach number and left nozzle boattail angle are discussed in the following sections.

Effect of Mach Number

The effect of Mach number on nozzle recompression is shown in figure 35. The pressure coefficients for the first and last nozzle orifices of each row are plotted against circumferential position on the nozzle for several test Mach numbers (figs. 35(a) to 35(d)) and against Mach number (fig. 35(e)).

Available data are presented for the eight rows at α ranging from 1° to 2°, BTL $\approx$ 18.4° and 7.7°, and an NPRL range of 2.0 to 5.0. Shown to the right of each distribution (as a solid symbol) is the average value for each of the circumferential distributions. The lengths and relative heights of the vertical lines connecting the solid symbols for the first and last orifices are interpreted as a measure of the recompression on the nozzle for model and flight. Therefore, comparing the vertical lines yields a comparison of recompression on the nozzle.

At $M_\infty \approx$ 0.6 with BTL $\approx$ 18.4° (fig. 35(a)), the C_p at the first nozzle orifices for flight are less negative than those for the model, except at ϕ = 86°. Figure 32(a) shows that the model flow is separated at row 86°. In figure 35(a), it is believed that the positive level of C_p near the nozzle exit at row 86° for the model propagate upstream in the subsonic field through the separated region, raising the level of C_p at the first nozzle orifice. Otherwise, the level would be more negative than that for flight.

The C_p levels for the last nozzle orifice agree reasonably well for model and flight. Highest C_p levels are noted for orifice row 182° at the bottom of the nacelle. This row is farthest from interference effects of the tails, tail-boom, or nozzle interfairing than are any of the other nozzle rows. Therefore, the highest pressure coefficients are achieved. The vertical recompression lines show that recompression for flight exceeds that for the model.

At $M_\infty \approx$ 0.8 with BTL $\approx$ 18.4° (fig. 35(b)), the data show slightly less recompression than at $M_\infty \approx$ 0.6 for model and flight, as indicated by the shorter vertical lines. The shapes of the C_p plots against ϕ are not greatly changed from those at $M_\infty \approx$ 0.6 for model and flight.

The data in figure 35(c) are for $M_\infty \approx$ 0.9 with BTL $\approx$ 18.4° and show an increasing loss in recompression compared with $M_\infty \approx$ 0.8 for both sets of data, as indicated by the shorter vertical lines. In addition, the model C_p profile for the first orifice is considerably more negative than that for flight except at row 86°, the row with separated flow. At the last nozzle orifice the flight C_p profile is consistently less negative than the model C_p profile.

At $M_\infty \approx$ 1.2 and BTL $\approx$ 7.7° (fig. 35(d)), the levels of recompression indicated by the vertical lines do not differ greatly, for either set of data, from the respective values at $M_\infty \approx$ 0.9. Therefore, the more negative C_p values at the last nozzle orifice relative to $M_\infty \approx$ 0.9 (fig. 35(c)) are caused by the more negative C_p occurring at the first nozzle orifice. This is true for both sets of data.

Figure 35(e) summarizes the effect of Mach number on nozzle recompression for an α range of 1° to 2°, an NPRL range of 2.0 to 5.0, and BTL $\approx$ 18.4° and 7.7°. Data are shown for the test conditions of figures 35(a) to (d) and the addi-

tional test conditions shown in table 7. The data were averaged for the several test conditions of the eight nozzle orifice rows yielding single values $\left(C_{p_{avg}}\right)$ for the pressure coefficients at the first and last orifices at each Mach number. As defined in the upper part of figure 35(e), ΔC_p is a measure of the average recompression on the nozzle.

For subsonic speeds at the first nozzle orifice, $C_{p_{avg}}$ for flight exceeds that for the model and increases slightly with Mach number. At $M_\infty \approx 1.2$ the increment of $C_{p_{avg}}$ for flight over that for the model is greatly increased. The increments for subsonic speeds and $M_\infty \approx 1.2$ are attributed to upstream effects.

For subsonic speeds at the last orifice, $C_{p_{avg}}$ for flight slightly exceeds $C_{p_{avg}}$ for the model. Both values of $C_{p_{avg}}$ exhibit a steady decrease with M_∞, and at $M_\infty \approx 0.84$ to 0.85 the values become negative. At $M_\infty \approx 1.2$, the $C_{p_{avg}}$ points are more negative than those at subsonic speeds particularly for the model.

The recompression curves, that is, the ΔC_p curves, show a steady loss in recompression over the subsonic Mach number range. Recompression for the model exceeds that for flight. At $M_\infty \approx 1.2$, recompression for model and flight agree and are comparable to the flight value for $M_\infty \approx 0.9$.

Effect of Left Nozzle Boattail Angle

The effect of left nozzle boattail angle on the comparison of nozzle recompression is shown in figure 36. Data are presented for left nozzle boattail angles of 15.1° and 18.4° and $M_\infty \approx 0.6$ and 0.9. Angles of attack ranged from 1° to 2°,

and NPRL ranged from 2.5 to 5.0. At $M_\infty \approx 0.6$, the average C_p level at the first orifice is approximately the same for both boattail angles for the model and flight data. A slight loss in recompression results from the increase in boattail angle and is about the same for the model and flight data. At $M_\infty \approx 0.9$, the loss in recompression caused by the boattail angle increase exceeds that at $M_\infty \approx 0.6$. This is particularly true for the flight data.

Summary

The effects of the test variables on the comparison of nozzle recompression are summarized as follows. An increase in subsonic Mach number caused a steady loss in nozzle recompression for the model and flight data. At $M_\infty \approx 0.84$ to 0.85, the average C_p at the last nozzle orifice went from positive to negative. At $M_\infty \approx 0.6$ and 0.9, an increase in boattail angle from 15.1° to 18.4° caused a loss in recompression.

Comparison of Nozzle Axial Force Coefficient

The effects of the test variables on nozzle axial force coefficient are discussed in the following sections.

Effect of Mach Number and Left Nozzle Boattail Angle

Figure 37 shows the effects of Mach number and left nozzle boattail angle on the comparison of nozzle axial force coefficient C_a. In figure 37(a), data are shown for $\alpha \approx 1°$ to 2° and for BTL $\approx 18.4°$ and 7.7° over an NPRL range of 2.5 to 5.0. The fairing for the flight data gives more weight to the 6100-m data points because the data at 10,700 m are subject to greater error (fig. 19). For BTL $\approx 18.4°$ and M_∞ ranging from 0.6 to 0.8, the faired values of the model and flight data agree and increase slightly with Mach

number. The increase in C_a is caused by the increasingly negative C_p levels with Mach number increase shown in figures 32(a) and 32(b) and the loss in recompression shown in figure 35(e).

As M_∞ increases to 0.9, C_a for both sets of data increases, but C_a for the model data increases more than for the flight data. As indicated in figure 32(c), levels of C_p for the model data are considerably lower than those for the flight data. This is attributed to upstream effects. As shown in figure 35(e), both sets of data exhibit a loss in recompression as M_∞ increases from 0.8 to 0.9.

In figure 37(a), at $M_\infty \approx 1.2$ with BTL $\approx 7.7°$, C_a values for both sets of data exceed the respective subsonic levels. C_a for the model is greater than the C_a level for the flight data. This result is also explained by figures 32(d) and 35(e).

Figure 37(b) shows the effect of left nozzle boattail angle on nozzle axial force coefficient for subsonic Mach numbers. The lines shown are the fairings of figure 37(a) for BTL $\approx 18.4°$; the data points are for the lower boattail angles. At $M_\infty \approx 0.6$, C_a for the lower boattail angles is only slightly less than C_a for BTL $\approx 18.4°$, with good agreement noted between the model and flight points. At $M_\infty \approx 0.9$, the decrement in C_a is about 3×10^{-4} units because of the reduction in boattail angle. The decrement is the same for the model and flight data.

Effect of Angle of Attack

The effect of angle of attack on the comparison of nozzle axial force coefficient is shown in figure 38 for three subsonic Mach numbers with BTL $\approx 18.4°$ and an NPRL range of 2.5 to 5.0. At $M_\infty \approx 0.6$, no effect of angle of attack is evident; at $M_\infty \approx 0.8$, C_a increases slightly as angle of attack increases from 1° to 7°. At $M_\infty \approx 0.9$, the data scatter and small variation in angle of attack preclude any interpretation.

Effect of Nozzle Pressure Ratio

The effect of nozzle pressure ratio (NPRL) on the comparison of nozzle axial force coefficient is shown in figure 39. Test data are for $\alpha \approx 1°$ to 2° and BTL $\approx 18.4°$ and 7.7° for several test Mach numbers. The design pressure ratio shown for each nozzle is the solid vertical line. In figures 39(a) to 39(c), for the subsonic test points, the model data were obtained over an NPRL range extending from jet off, through the overexpanded region where NPRL is greater than approximately 1.9 and less than the design NPRL, into the underexpanded region where NPRL is greater than the design value.

With the jet operating, peak levels of C_a occur near the design value of NPRL = 3.4. As explained in references 12, 13, and 14, jet interference effects for values of NPRL less than that at peak C_a are influenced primarily by entrainment of the nozzle external flow caused by viscous shear and mixing. Entrainment tends to reduce the pressure on the nozzle external surface. As NPRL increases, jet interference effects are increasingly influenced by the physical presence of the jet plume acting as a solid body and less by entrainment. The jet plume increases in size after leaving the nozzle and tends to raise the pressure on the nozzle external surface, thereby reducing C_a. These jet flow phenomena appear to explain the variation in C_a exhibited by the model data.

Flight test data are shown in figures 39(a) to 39(c) for two altitudes at values of NPRL close to the design value.

The fairing for the four test points in figure 39(c) for $M_\infty \approx 0.9$ favors the data obtained at 6100 m. Figure 39 also shows the jet temperature and mass flux ratio for a model and a flight test point for each of the four correlations (that is, the eight shaded points). As discussed in references 13 and 14, the product of the jet gas constant and the jet temperature and the ratio of the jet-to-free-stream mass flux are two parameters that can be used to analyze the effects of jet temperature on nozzle axial force during overexpanded flow. In this study, only the jet temperature was used because the gas constant for the model and the flight data are virtually identical (table 3).

At $M_\infty \approx 0.6$ and 0.8 (figs. 39(a) and 39(b), respectively), excellent agreement in C_a exists between the flight data at 6100 m and the model data. At $M_\infty \approx 0.9$ (fig. 39(c)), the model data exceed the faired flight data by about 5×10^{-4} units of C_a. These results suggest there is no apparent effect of jet temperature on the agreement of C_a between model and flight. There is negligible change in the jet parameters going from $M_\infty \approx 0.8$ to $M_\infty \approx 0.9$, yet the agreement is excellent at $M_\infty \approx 0.8$ and relatively poor at $M_\infty \approx 0.9$.

Figure 39(d) shows C_a as a function of NPRL obtained at $M_\infty \approx 1.2$. The NPRL test range for the model data extended from 5.0 to 7.0, which includes the design NPRL of 6.1. Over this range, the model C_a decreases from 20×10^{-4} to 15×10^{-4} units, indicating that jet interference is dominated by the jet plume shape rather than by entrainment. This is explained as follows. As shown in figure 21(d), model and flight fuselage pressure coefficient distributions close to the jet exhaust are at large negative levels. Since the jet is exhausting into a region where pressure is considerably less than atmospheric

pressure, the effective nozzle pressure ratio probably exceeds the calculated values. This causes the jet to be under-expanded and explains the sharp reduction in C_a.

At an NPRL value of 5.0 (fig. 39(d)), the flight level of C_a is about 5×10^{-4} units less than the model data. This disagreement is the same as that noted at $M_\infty \approx 0.9$. Examining the jet parameters from $M_\infty \approx 0.9$ to 1.2, the data show there is essentially no change for the model parameters, but there is an increase in jet temperature and a reduction in mass flux ratio for the flight test data. Because the jet is operating in an underexpanded condition, any change in entrainment caused by the change in jet mass flux ratio for the flight data is not considered to be significant. In addition, since there is no change in the difference in C_a between model and flight, and despite the increase in jet temperature going from $M_\infty \approx 0.9$ to 1.2, the increase in jet temperature is like-wise not considered to be significant.

Effect of Reynolds Number

Figure 40 shows the effect of Reynolds number on nozzle axial force coefficient. Data are presented for several Mach numbers at $\alpha \approx 1°$ to $2°$. The NPRL range is from 2.0 to 3.6 at BTL $\approx 18.4°$ (figs. 40(a), 40(b), and 40(c)); the NPRL is 5.0 for BTL $\approx 7.7°$ (fig. 40(d)). In figures 40(a) and 40(b), for $M_\infty \approx 0.6$ and 0.8, respectively, there appears to be a negligible effect of Reynolds number on the data. This result follows from the good agreement of model and flight values of C_a shown in figure 39 at these Mach numbers. At $M_\infty \approx 0.9$ (fig. 40(c)) and at $M_\infty \approx 1.2$ (fig. 40(d)) the data indicate a decrease in C_a of approximately 4×10^{-4} to 5×10^{-4} units over the test range. The decreases in C_a shown are attributed to differences in

the upstream flows between the model and the flight data.

Effect of Mach Number on the Sensitivity of Axial Force Coefficient to Reynolds Number

The effect of Mach number on the sensitivity of nozzle axial force coefficient to Reynolds number ($\Delta C_a/\Delta Re$) is shown in figure 41. The parameter $\Delta C_a/\Delta Re$ was obtained by taking the slopes of the fairings in figure 40. As indicated in figure 41, the rate of change of C_a with Re is zero up to $M_\infty \approx 0.8$, decreases to a minimum at $M_\infty \approx 0.9$, and increases slightly with further increase in M_∞ to 1.2.

Summary

The effects of the test variables on nozzle axial force coefficient are summarized as follows. As M_∞ increased from 0.6 to 0.8, at $\alpha \approx 1°$ to 2°, model and flight C_a obtained at 6100 m agreed closely and increased slightly. Above $M_\infty \approx 0.8$, C_a increased for both sets of data; the model data were 4 to 5×10^{-4} units higher than the flight data at $M_\infty \approx 0.9$ and 1.2. At $M_\infty \approx 0.6$ and 0.9, reducing the BTL reduced C_a. At subsonic speeds, peak values of C_a occurred near the design pressure ratio for the model data. At $M_\infty \approx 1.2$, the jet appeared to be expanding into a region well below atmospheric pressure, which increased the effective nozzle pressure ratio. Reynolds number effects were noted only for $M_\infty \approx 0.9$ and 1.2, and jet temperature, mass flux ratio, and angle of attack had negligible effects on nozzle axial force.

CONCLUSIONS

Aft fuselage, boundary layer, and nozzle pressures were measured on a 1/12-scale propulsion model in a wind tunnel and in flight on a twin-jet fighter aircraft over a Mach number range of 0.6 to 1.2, a Reynolds number range of 17.5 million to 302.5 million, and an angle-of-attack range of 1° to 7°. These tests provided data bases from which data were selected and compared to yield the following conclusions.

1. For Mach 0.6 and 0.8, at an angle of attack of 1° to 2°, model values of nozzle axial force coefficient agreed closely with flight values obtained at an altitude of 6100 m. Above Mach 0.8, nozzle axial force coefficients increased for both sets of data, but the model data were 5×10^{-4} units higher than the flight data at Mach 0.9 and 1.2. Reynolds number effects on nozzle axial force coefficient were noted only at Mach 0.9 and 1.2. Variations in jet temperature and mass flux ratio did not affect the comparisons of nozzle axial force coefficient.

2. For Mach 0.6 and 0.8, pressure coefficient distributions on the external nozzle surface of the left nozzles of the model and the airplane agreed in level and trend. Recompression was good. At Mach 0.9 and 1.2, both sets of data showed flow separation, increasing flow complexity, and a loss in recompression. Although pressure distributions agreed in trend, differences in the level of pressure coefficient caused by effects upstream of the nozzle propagated along the nozzle surface. This caused the flight data to exhibit less negative levels of pressure coefficient than the model data on all the nozzle rows.

3. Pressure coefficient distributions on the aft fuselage surfaces for model and flight were similar over the Mach number and angle-of-attack test ranges. At subsonic speeds, flight levels of C_p were generally less negative than those of the model on the upper surfaces and the lower nacelle.

4. Mach number and angle of attack affected the model boundary layer pro-

files and thicknesses at the forward and aft rake stations more than for flight.

For the model, boundary layer thickness at the aft rake station exceeded that at the forward rake station and increased markedly with angle of attack. In flight, the boundary layer thickness at the aft rake station was less than that at the forward rake station and decreased with angle of attack.

5. Except for the effect of angle of attack on the boundary layer parameters, its overall effects on the comparisons of the pressure coefficient distributions and nozzle axial force were small.

APPENDIX — DERIVATION OF PITOT PRESSURE
RATIO IN THE BOUNDARY LAYER FOR AN
ASSUMED VELOCITY RATIO DISTRIBUTION

$$\frac{\left(5 + M^2\right)^{1/2}}{M} = \frac{\left(5 + M_\infty^2\right)^{1/2}}{M_\infty} \frac{1}{\left(\frac{H}{\delta}\right)^{1/n}}$$

$$\frac{5 + M^2}{M^2} = \frac{5 + M_\infty^2}{M_\infty^2} \frac{1}{\left(\frac{H}{\delta}\right)^{2/n}} = c$$

where

$$c = \frac{5 + M_\infty^2}{M_\infty^2} \frac{1}{\left(\frac{H}{\delta}\right)^{2/n}}$$

$$5 + M^2 = CM^2$$

$$M^2 - CM^2 = -5$$

$$M^2(1 - C) = -5$$

$$M^2 = \frac{5}{C - 1}$$

$$M = \sqrt{\frac{5}{C - 1}} \qquad (2)$$

M was evaluated in the boundary layer
by equation (2), using values of H from 0
to δ where M_∞ and δ were obtained from
the flight test point. The value of n
selected was 9.
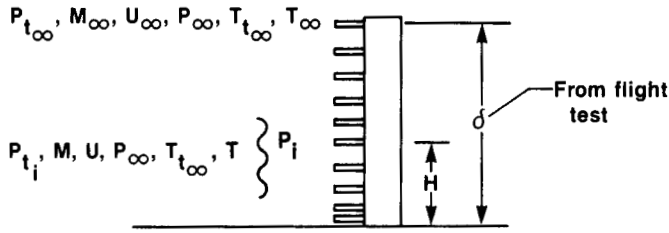
The Mach number in the boundary layer is
first derived as follows. Assume a
velocity distribution with index n:

$$\left(\frac{H}{\delta}\right)^{1/n} = \frac{U}{U_\infty} \qquad (1)$$

Also assume that the total temperature
and static pressure in the boundary layer
are equal to the free-stream values:

$$\left(\frac{H}{\delta}\right)^{1/n} = \frac{M \sqrt{\gamma R T}}{M_\infty \sqrt{\gamma R T_\infty}} = \frac{M \sqrt{T} \sqrt{T_{t_\infty}}}{M_\infty \sqrt{T_\infty} \sqrt{T_{t_\infty}}}$$

$$= \frac{M \sqrt{T_{t_\infty}/T_\infty}}{M_\infty \sqrt{T_{t_\infty}/T}}$$

$$= \frac{M \left(1 + 0.2 M_\infty^2\right)^{1/2}}{M_\infty \left(1 + 0.2 M^2\right)^{1/2}}$$

Rearranging gives

To calculate the pitot pressure ratio
with M subsonic,

$$P_i = P_{t_i}$$

$$P_i = \frac{P_{t_i}}{P_\infty} P_\infty$$

$$= \left(1 + 0.2M^2\right)^{3.5} P_\infty$$

$$P_{t_\infty} = \frac{P_{t_\infty}}{P_\infty} P_\infty$$

$$= \left(1 + 0.2M_\infty^2\right)^{3.5} P_\infty$$

$$\frac{P_i}{P_{t_\infty}} = \frac{\left(5 + M^2\right)^{3.5} P_\infty}{\left(5 + M_\infty^2\right)^{3.5} P_\infty}$$

$$\frac{P_i}{P_{t_\infty}} = \left(\frac{5 + M^2}{5 + M_\infty^2}\right)^{3.5} \quad (3)$$

With M supersonic,

$$\frac{P_i}{P_{t_i}} = \left(\frac{6M^2}{5 + M^2}\right)^{3.5} \left(\frac{6}{7M^2 - 1}\right)^{2.5}$$

$$\frac{P_i}{P_{t_\infty}} = \frac{P_i}{P_{t_i}} \frac{P_{t_i}}{P_{t_\infty}}$$

$$= \left(\frac{6M^2}{5 + M^2}\right)^{3.5} \left(\frac{6}{7M^2 - 1}\right)^{2.5}$$

$$\times \left(\frac{5 + M^2}{5 + M_\infty^2}\right)^{3.5}$$

$$\frac{P_i}{P_{t_\infty}} = \left(\frac{6M^2}{5 + M_\infty^2}\right)^{3.5} \left(\frac{6}{7M^2 - 1}\right)^{2.5} \quad (4)$$

REFERENCES

1. Webb, Lannie D.; and Nugent, Jack: Selected Results of the F-15 Propulsion Interactions Program. AIAA Paper 82-1041, June 1982.

2. Webb, Lannie D.; Varda, Dominic A.; and Whitmore, Stephen A.: Flight and Wind Tunnel Comparisons of the Inlet/Airframe Interaction of the F-15 Airplane. NASA TP-2374, 1984.

3. Pendergraft, Odis C., Jr.: Fuselage and Nozzle Pressure Distributions on a 1/12-Scale F-15 Propulsion Model at Transonic Speeds. NASA TP-1521, 1979.

4. Nugent, Jack; Taillon, Norman V.; and Pendergraft, Odis C., Jr.: Status of a Nozzle Airframe Study of a Highly Maneuverable Fighter. AIAA Paper 78-990, July 1978.

5. Plant, Thomas J.; Nugent, Jack; and Davis, Robert A.: Flight Measured Effects of Boattail Angle and Mach Number on the Nozzle Afterbody Flow of a Twin-Jet Fighter. AIAA Paper 80-0110, Jan. 1980.

6. Nugent, Jack; Plant, Thomas J.; Davis, Robert A.; and Taillon, Norman V.: Pressures Measured in Flight on the Aft Fuselage and External Nozzle of a Twin-Jet Fighter. NASA TP-2017, 1983.

7. Pendergraft, Odis C., Jr.; and Carson, George T., Jr.: Fuselage and Nozzle Pressure Distributions of a 1/12-Scale F-15 Propulsion Model at Transonic Speeds — Effect of Fuselage Modifications and Nozzle Variables. NASA TP-2333, 1984.

8. Peddrew, Kathryn H.: A User's Guide to the Langley 16-Foot Transonic Tunnel. NASA TM-83186, 1981.

9. Martins, Richard E.: F-15 Nozzle Afterbody Integration. AIAA Paper 74-1100, Oct. 1974.

10. Lorincz, Dale J.: A Water Tunnel Flow Visualization Study of the F-15. NASA CR-144878, 1978.

11. Swann, M.R.; Duke, E.L.; Enevoldson, E.K.; and Wolf, T.D.: Experience With Flight Test Trajectory Guidance. AIAA Paper 81-2504, Nov. 1981.

12. Bergman, D.: Effects of Engine Exhaust Flow on Boattail Drag. J. Aircraft, vol. 8, no. 6, pp. 434-439, June 1971.

13. Peters, W. L.: A Comparison of Jet Temperature Effects on Afterbody Drag With Those From Jet Molecular Weight and Nozzle Area Ratio Variations. AIAA Paper 80-1161, June 30-July 2, 1980.

14. Compton, William B. III: Effects of Jet Exhaust Gas Properties on Exhaust Simulation and Afterbody Drag. NASA TR R-444.

TABLE 1. — LOCATIONS OF SURFACE PRESSURE
ORIFICES ON FUSELAGE

(a) Upper fuselage centerline

Model		Airplane	
X/L	Y/L	X/L	Y/L
0.077	0	0.079	0
0.155	0	0.154	0
0.217	0	a	---
0.297	0	a	---
0.382	0	a	---
0.456	0	0.455	0
0.534	0	0.533	0
0.611	0	0.597	0
0.684	0	0.684	0.004
0.808	0	0.810	0.004
0.843	0	0.840	0.003
0.913	0	0.929	0

(b) Lower fuselage centerline

Model		Airplane	
X/L	Y/L	X/L	Y/L
0.684	0	0.684	0
0.808	0	0.807	0
0.843	0	0.844	0
0.913	0	0.930	0

(c) Upper left nacelle centerline

Model		Airplane	
X/L	Y/L	X/L	Y/L
0.534	-0.038	0.533	-0.038
0.611	-0.038	0.609	-0.038
0.684	-0.038	0.677	-0.038
---	---	0.781[b]	-0.036
0.808	-0.036	0.808	-0.036
---	---	0.829[b]	-0.036
0.845	-0.036	0.845	-0.036
---	---	0.857[b]	-0.036
0.873	-0.035	0.872	-0.035
---	---	0.882[b]	-0.035

(d) Lower left nacelle centerline

Model		Airplane	
X/L	Y/L	X/L	Y/L
0.534	-0.038	0.531	-0.039
0.611	-0.038	0.611	-0.038
0.684	-0.038	0.684	-0.038
0.808	-0.036	0.836[c]	-0.036
0.845	-0.037	0.849	-0.036
0.873	-0.035	0.870	-0.035

(e) Upper right nacelle centerline

Model		Airplane	
X/L	Y/L	X/L	Y/L
0.684	0.038	0.684	0.037
---	---	0.867[b]	0.037

(f) Lower right nacelle centerline

Model		Airplane	
X/L	Y/L	X/L	Y/L
0.684	0.038	0.684	0.037

(g) Left side

Model		Airplane	
X/L	Y/L	X/L	Y/L
0.611	-0.134	0.611	-0.134
0.684	-0.134	0.184	-0.134

(h) Right side

Model		Airplane	
X/L	Y/L	X/L	Y/L
0.684	0.134	0.684	0.134

[a]Canopy area not instrumented on the airplane.
[b]Installed for inlet interactions program (ref. 2).
[c]Relocated to clear afterburner vent.

27

TABLE 1. — Concluded

(i) Upper left tailboom

Model		Airplane	
X/L	Y/L	X/L	Y/L
0.843	-0.076	0.839	-0.077
0.873	-0.076	0.871	-0.076
0.913	-0.076	0.919	-0.081

TABLE 2. — LOCATIONS OF SURFACE
PRESSURE ORIFICES ON NOZZLE

(a) BTL = 18.4° and BTL = 15.1°

(1) Rows 350°, 62°, 182°

X/L	
Model	Airplane
0.898[a]	0.897[a]
0.904	0.904
0.912	0.911
0.919	0.919
0.924	0.924
0.931	0.931

(2) Rows 86°, 230°, 278°

X/L	
Model	Airplane
0.898[a]	0.897[a]
0.912	0.911
0.925	0.924
0.932	0.931

(3) Row 134°

X/L	
Model	Airplane
0.912	0.911
0.919	0.919
0.925	0.924
0.932	0.931

(4) Row 302°

X/L	
Model	Airplane
0.898[a]	0.897[a]
0.904	0.904
0.912	0.911
0.919	0.919
0.924	0.924
0.928	0.928
0.931	0.931
0.934	0.934

[a] Located on the fixed portion of the nozzle; all other locations are on the variable portion of the nozzle.

28

TABLE 2. — Concluded

(b) BTL = 7.7°

(1) Rows 350°, 62°, 182°

X/L	
Model	Airplane
0.898[a]	0.897[a]
0.904	0.904
0.912	0.911
0.919	0.919
0.925	0.924
0.932	0.931

(2) Rows 86°, 230°, 278°

X/L	
Model	Airplane
0.898[a]	0.897[a]
0.912	0.911
0.925	0.924
0.932	0.931

(3) Row 134°

X/L	
Model	Airplane
0.912	0.911
0.919	0.919
0.925	0.924
0.932	0.931

(4) Row 302°

X/L	
Model	Airplane
0.898[a]	0.897[a]
0.904	0.904
0.912	0.911
0.919	0.919
0.925	0.924
0.928	0.928
0.932	0.931
0.935	0.934

[a]Located on the fixed portion of the nozzle; all other locations are on the variable portion of the nozzle.

TABLE 3. — TEST CONDITIONS USED FOR THE COMPARISONS

(a) Model test conditions for comparisons of surface pressures[a]

Test point	M_∞	α, deg	BTL, deg	BTR, deg	NPRL	$Re_m \times 10^{-6}$	$C_a \times 10^{-4}$
1	0.60	0.99	18.4	18.4	1.00	17.7	8
2	0.60	1.00	18.4	18.4	1.50	17.8	3
3	0.60	0.99	18.4	18.4	2.00	17.8	5
4	0.60	0.99	18.4	18.4	3.00	17.9	6
5	0.60	0.97	18.4	18.4	3.90	17.9	5
6	0.60	2.98	18.4	18.4	3.00	17.9	6
7	0.60	4.98	18.4	18.4	3.00	17.8	6
8	0.80	1.00	18.4	18.4	1.00	20.3	13
9	0.80	1.00	18.4	18.4	2.50	20.3	8
10	0.80	1.01	18.4	18.4	3.50	20.3	8
11	0.80	1.00	18.4	18.4	4.60	20.4	7
12	0.80	3.00	18.4	18.4	2.50	20.3	9
13	0.80	4.99	18.4	18.4	2.50	20.3	9
14	0.80	7.01	18.4	18.4	3.50	20.3	10
15	0.90	1.00	18.4	18.4	0.99	21.8	17
16	0.90	0.99	18.4	18.4	2.50	21.4	15
17	0.90	0.99	18.4	18.4	3.60	21.3	16
18	0.90	1.01	18.4	18.4	4.50	21.2	15
19	0.90	1.01	18.4	18.4	5.03	21.1	14
20	0.90	2.98	18.4	18.4	2.51	21.4	17
21[b]	0.60	1.00	15.1	18.4	3.90	17.1	4
22[b]	0.90	1.97	15.1	18.4	5.00	20.2	12
23[b]	1.20	1.00	7.72	7.72	4.99	21.0	20
24[b]	1.20	1.00	7.72	7.72	6.53	20.8	16
25[b]	1.20	1.00	7.72	7.72	7.05	20.7	15

[a]Stabilator position was 0° for these tests.
[b]Rakes were installed.

TABLE 3. — Continued

(b) Airplane test conditions for comparison of surface pressures

Test point	M_∞	α, deg	H_p, m	BTL, deg	BTR, deg	NPRL	$Re_a \times 10^{-6}$	$C_a \times 10^{-4}$
1	0.63	1.09	6,266	18.2	19.5	2.65	143.8	6
2	0.63	1.23	6,251	18.2	19.5	2.65	143.1	5
3	0.64	1.00	10,169	18.1	19.7	2.84	100.0	8
4	0.60	3.11	6,081	17.8	19.7	2.76	148.1	7
5	0.61	3.22	6,120	18.2	19.6	2.42	139.4	7
6	0.60	3.00	10,279	18.1	19.5	2.86	92.5	4
7	0.60	5.05	6,303	18.2	19.6	2.57	136.9	8
8	0.60	5.19	6,155	17.8	19.6	2.79	146.9	8
9	0.61	5.38	6,331	18.2	19.6	2.58	137.5	6
10	0.61	5.79	10,520	18.1	19.6	2.74	91.3	6
11	0.81	1.11	6,075	18.8	19.5	2.95	194.4	8
12	0.81	1.12	6,082	18.8	19.6	2.96	193.8	8
13	0.79	1.55	6,291	18.8	19.6	2.59	178.8	8
14	0.82	3.09	6,132	18.0	16.0	2.54	189.4	9
15	0.80	3.12	6,216	17.8	19.6	3.31	194.4	9
16	0.82	3.17	6,151	18.0	16.2	2.55	188.8	9
17	0.80	3.01	10,637	18.2	19.6	2.94	115.6	9
18	0.79	3.02	13,180	17.8	19.3	2.92	82.5	9
19	0.81	5.01	10,660	18.1	18.6	3.29	118.8	10
20	0.81	5.02	10,655	18.1	18.6	3.29	119.4	10
21	0.80	5.00	13,639	17.8	19.2	4.06	75.0	9
22	0.80	5.01	13,713	17.7	19.2	3.74	78.1	9
23	0.80	6.23	13,635	17.8	18.5	3.14	78.8	9
24	0.88	0.89	6,397	18.9	19.7	3.05	201.3	10
25	0.87	0.98	6,402	18.9	19.7	3.05	200.0	9
26	0.91	1.05	6,385	18.1	15.4	2.87	203.8	11
27	0.90	1.20	10,699	18.1	19.3	3.63	131.9	14
28	0.91	3.05	5,912	17.9	19.3	4.19	228.1	15
29	0.90	3.10	6,146	17.9	19.2	4.32	221.9	14
30	0.89	3.08	10,663	18.1	19.2	3.61	131.3	13
31	0.89	3.09	10,669	18.1	19.4	3.62	131.3	12
32	0.89	3.09	13,764	17.9	18.5	3.53	86.9	12
33	0.90	3.42	13,565	17.8	19.3	4.20	85.6	13
34	0.61	1.00	10,894	14.1	19.6	4.01	87.5	5
35	0.91	2.20	10,624	14.7	19.5	5.14	130.7	8
36	1.19	0.84	6,008	7.3	8.0	5.00	295.0	15
37	1.22	0.84	6,272	7.2	7.9	4.97	302.5	14

TABLE 3. — Concluded

(c) Thermodynamic properties of jet for
selected test conditions of figure 39

(1) Model tests

Test point	T_m, K	Gas constant, J/kg•K	Ratio of specific heats	MFRM
4	307	287.1	1.4	2.39
9	317	287.1	1.4	1.44
16	282	287.1	1.4	1.30
23	298	287.1	1.4	1.44

(2) Flight tests

Test point	T_a, K	Gas constant, J/kg•K	Ratio of specific heats	MFRA
3	541	287.2	1.38	1.25
11	580	287.2	1.37	1.04
24	620	287.2	1.37	1.07
37	1824	287.5	1.27	0.54

TABLE 4. — TEST CONDITIONS FOR COMPARISON OF BOUNDARY LAYER PROFILES

(a) Model tests

Test point	M_∞	α, deg	BTL, deg	BTR, deg	NPRL	$Re_m \times 10^{-6}$	P_{t_∞}, N/cm^2	T_{t_∞}, K
26[a]	0.60	2.99	18.4	18.4	2.00	17.5	10.23	310
27[a]	0.80	1.00	18.4	18.4	3.51	20.0	10.23	320
28[a]	0.80	2.98	18.4	18.4	3.50	20.0	10.24	320
29[a]	0.80	6.99	18.4	18.4	3.52	20.0	10.24	320
30[a]	0.90	2.99	18.4	18.4	3.60	20.9	10.24	322
31[b]	1.20	2.90	7.72	7.72	5.01	20.9	10.20	336

[a]Stabilator position is -2°.

[b]Stabilator position is 2°.

(b) Flight tests

Test point	M_∞	α, deg	H_p, m	BTL, deg	BTR, deg	NPRL	$Re_a \times 10^{-6}$	P_{t_∞}, N/cm^2	T_{t_∞}, K
38	0.60	3.50	10,684	18.0	19.6	3.1	81.3	2.38	251
39	0.82	1.28	5,910	18.1	19.6	2.8	203.8	7.26	281
40	0.80	3.14	10,581	18.0	19.5	2.0	125.0	2.42	241
41	0.80	6.97	10,686	17.9	19.2	4.4	109.4	2.38	264
42	0.91	3.10	5,949	17.7	19.6	3.7	224.4	7.95	288
43	1.21	2.50	13,884	12.3	9.7	3.4	108.9	3.50	285

TABLE 5. — PITOT PRESSURE RATIOS OBTAINED FROM BOUNDARY LAYER RAKES

(a) Model

(1) Forward rake

H,[a] cm	Test point					
	26	27	28	29	30	31
0	0.7822[b]	0.6667	0.6577	0.6435	0.5995	0.4736
1.82	0.8982	0.8491	0.8363	0.8035	0.8097	0.6778
11.58	0.9958	0.9929	0.9926	0.9837	0.9879	0.8430
17.98	0.9969	0.9931	0.9937	0.9927	0.9891	0.8624
23.46	0.9987	0.9958	0.9965	0.9957	0.9906	0.8901
29.56	0.9946	0.9896	0.9903	0.9898	0.9827	0.8910
41.45	0.7768[c]	0.6681	0.6613	0.6446	0.6117	0.4826

[a]Scaled to flight.

[b]Surface static pressure divided by P_{t_∞}.

[c]Static pressure divided by P_{t_∞}.

(2) Aft rake

H, cm	Test point					
	26	27	28	29	30	31
0	---	---	---	---	---	---
3.05	0.8947	0.8480	0.8207	0.8086	0.7753	0.6063
12.19	0.9640	0.9691	0.9224	0.8800	0.8904	0.7499
18.29	0.9864	0.9905	0.9684	0.9055	0.9523	0.8261
24.38	0.9946	0.9899	0.9880	0.9427	0.9776	0.9003
30.48	0.9877	0.9569	0.9354	0.9388	0.9312	0.8490
41.45	0.7524[c]	0.6507	0.6414	0.6318	0.6176	0.4114

[c]Static pressure divided by P_{t_∞}.

TABLE 5. — Concluded

(b) Flight

(1) Forward rake

H, cm	Test point					
	38	39	40	41	42	43
0	0.795[b]	0.666	0.672	0.664	0.611	0.491
0.76	0.903	0.814	0.826	0.835	0.768	0.647
1.40	0.911	0.823	0.831	0.856	0.781	0.662
3.99	0.942	0.864	0.879	0.914	0.824	0.738
7.87	0.968	0.913	0.928	0.962	0.869	0.824
13.46	0.986	0.974	0.975	0.988	0.937	0.930
19.18	0.997	0.995	0.995	0.992	0.980	0.978
24.64	1.006	1.001	0.999	0.991	0.997	0.984
29.41	1.005	1.003	1.001	0.983	1.001	0.985
33.93	1.007	1.001	0.999	0.975	0.999	0.987
38.43	0.998	0.999	0.991	0.962	0.997	0.985

[b]Surface static pressure divided by P_{t_∞}.

(2) Aft rake

H, cm	Test point					
	38	39	40	41	42	43
0	0.754[b]	0.622	0.626	0.624	0.590	0.432
0.76	0.887	0.815	0.818	0.829	0.773	0.622
1.40	0.914	0.845	0.847	0.868	0.804	0.660
3.94	0.950	0.930	0.929	0.958	0.894	0.819
7.77	0.981	0.973	0.970	0.983	0.951	0.923
13.41	0.990	0.997	0.990	0.978	0.990	0.955
19.18	0.996	0.997	0.992	0.965	0.995	0.956
24.89	0.997	0.998	0.996	0.951	0.991	0.958
29.11	0.995	0.999	0.987	0.940	0.987	0.955
33.83	0.991	0.998	0.977	0.935	0.984	0.956
38.43	0.987	1.001	0.969	0.929	0.987	0.954

[b]Surface static pressure divided by P_{t_∞}.

TABLE 6. — BOUNDARY LAYER THICKNESSES MEASURED IN FLIGHT

Test point	Thickness, cm		Displacement thickness, cm		Momentum thickness, cm	
	Forward rake	Aft rake	Forward rake	Aft rake	Forward rake	Aft rake
38	23.1	17.5	1.8	1.0	1.4	0.7
39	22.3	12.3	2.3	1.0	1.5	0.7
40	22.0	16.1	2.1	0.9	1.4	0.7
41	13.3	7.0	1.1	0.5	0.8	0.4
42	25.5	12.1	3.0	1.0	1.9	0.7
43	20.5	12.4	2.9	1.3	1.6	0.7

TABLE 7. — FIGURE CONTENT AND TEST CONDITIONS OF
FIGURES IN RESULTS AND DISCUSSION SECTION

Figure	Figure content	Test points	
		Model	Flight
21, 29, 32	Comparisons of surface pressure coefficient distributions as Mach number is varied	4, 9, 16, 23	2, 11, 25, 37
22, 30, 33	Comparisons of surface pressure coefficient distributions as angle of attack is varied	9, 12 to 14	11, 14, 22, 23
23, 31, 34	Comparisons of surface pressure coefficient distributions, nozzle recompression, and nozzle axial force as left boattail angle is varied	4, 16, 21, 22	2, 26, 34, 35
24	Comparison of boundary layer profiles and thicknesses as Mach number is varied	26, 28, 30, 31	38, 40, 42, 43
25	Comparison of boundary layer profiles and thicknesses as angle of attack is varied	27 to 29	39 to 41
35(a), (b), (c), (d)	Comparison of recompression on the nozzle circumference as Mach number is varied at $\alpha \approx 1°$ to $2°$	4, 9, 16, 23	2, 11, 25, 37
35(e)	Comparison of recompression on the nozzle circumference as Mach number is varied at $\alpha \approx 1°$ to $2°$	3 to 5, 9 to 11, 16 to 19, 23	1 to 3, 11 to 13, 24 to 27, 36, 37
36	Comparison of recompression on the nozzle as left boattail angle is varied at $\alpha \approx 1°$ to $2°$	4, 16, 21, 22	2, 26, 34, 35
37	Effect of Mach number and left boattail angle on the comparison of nozzle axial force coefficient at $\alpha \approx 1°$ to $2°$, NPRL ≈ 2.5 to 5.0	3 to 5, 9 to 11, 16 to 19, 21 to 23	1 to 3, 11 to 13, 24 to 27, 34 to 37
38	Effect of angle of attack on the comparison of nozzle axial force coefficient at NPRL ≈ 2.5 to 5.0	3 to 7, 9 to 14, 16 to 20	1 to 33
39	Effect of nozzle pressure ratio on the comparison of nozzle axial force coefficient at $\alpha \approx 1°$	1 to 5, 8 to 11, 15 to 19, 23 to 25	1 to 3, 11 to 13, 24 to 27, 36, 37
40	Effect of Reynolds number on nozzle axial force coefficient	3, 4, 9, 10, 16, 17, 23	1 to 3, 11 to 13, 24 to 27, 36, 37
41	Effect of Mach number on the rate of change of nozzle axial force coefficient with Reynolds number	3, 4, 9, 10, 16, 17, 23	1 to 3, 11 to 13, 24 to 27, 36, 37
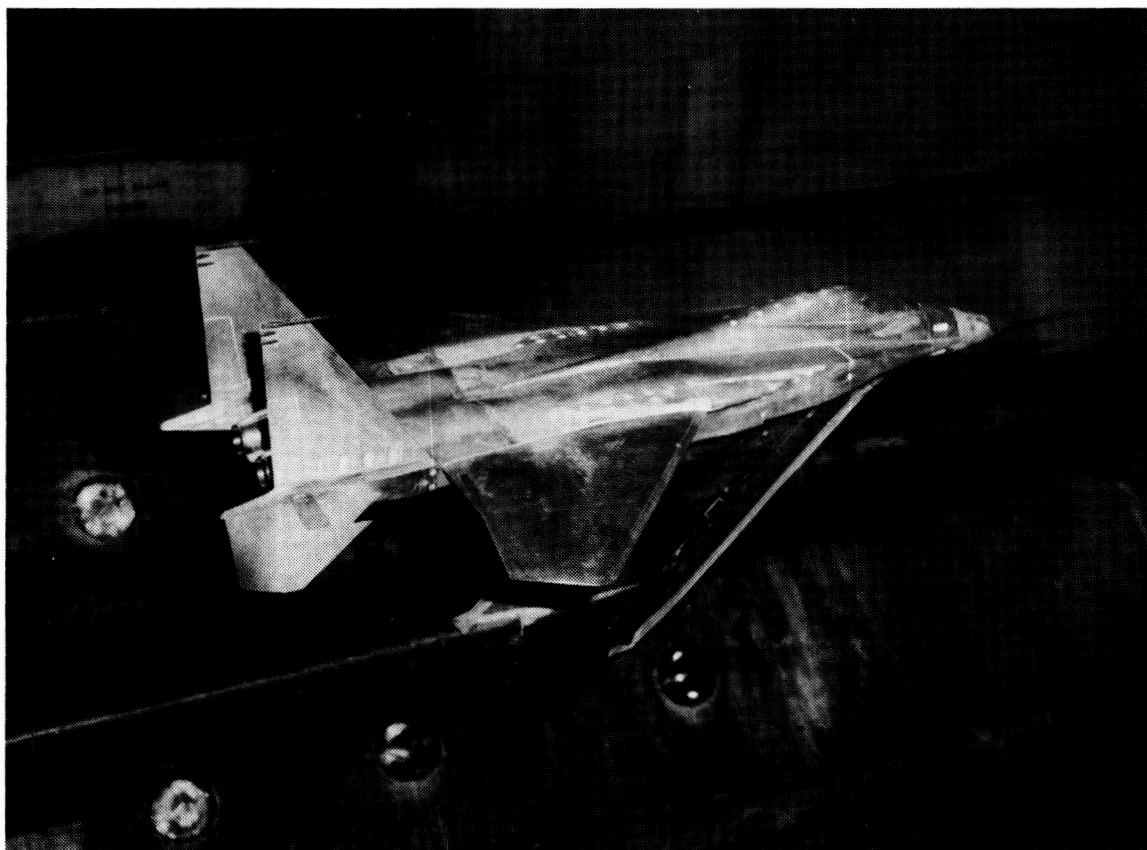
L-81-10,410

Figure 1.   1/12-scale F-15 propulsion model in the NASA Langley transonic wind tunnel.

F.S.
101.915

F.S. 157.134

F.S. 183.302

Interfairing

Nacelle

16.299

14.816

35.878

22.543

Tail
boom

9.851

54.364

14.464

F.S.
150.495

6.481

F.S. 138.107

26.213

F.S.
24.613

F.S.
165.423

158.689

Metric
break

x
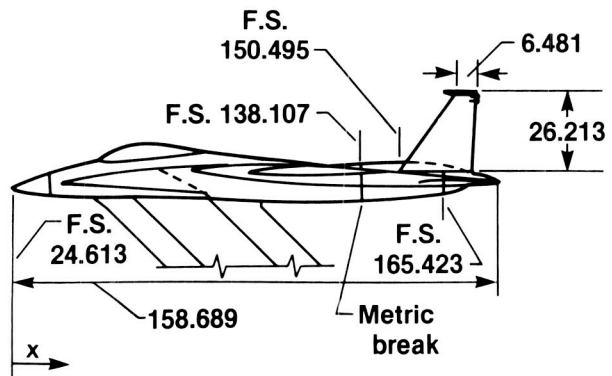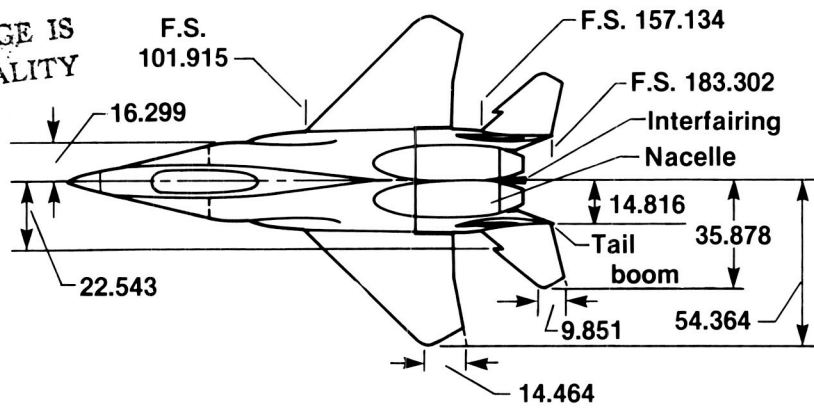
Figure 2. Details of F-15 propulsion model
geometry (dimensions in centimeters).
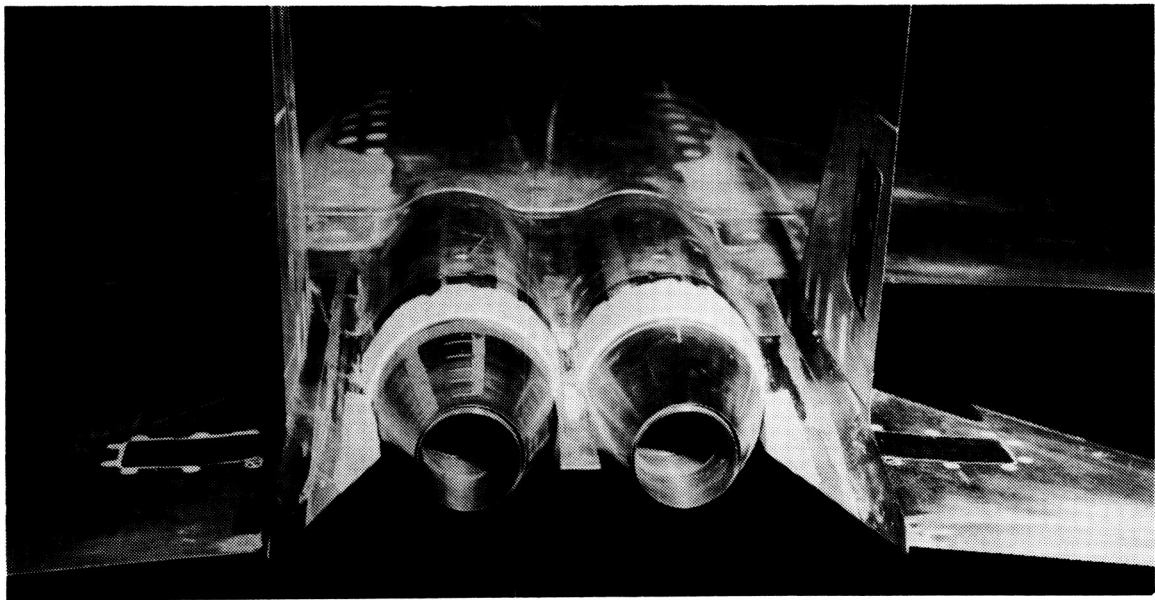
L-81-10,408

Figure 3. View of F-15 propulsion model showing afterbody details and
military power test nozzle; BTL = 18.4°.
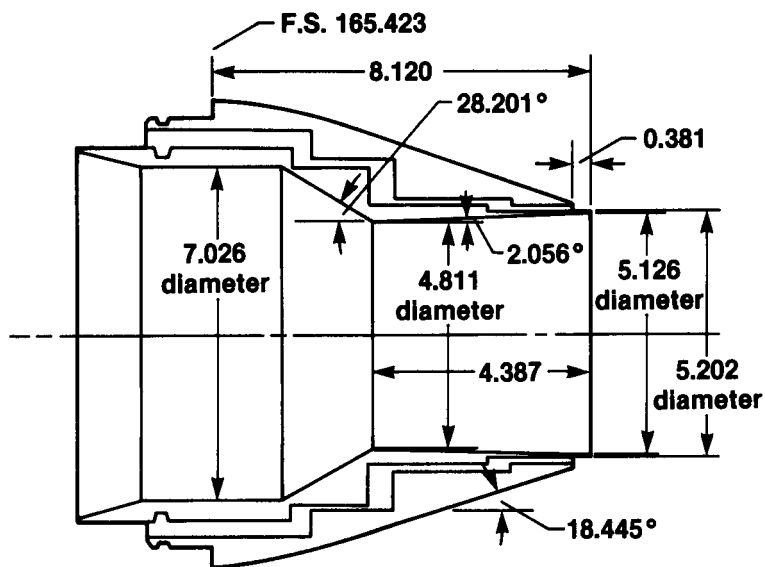
(a) *Military power setting, BTL = 18.4°.*
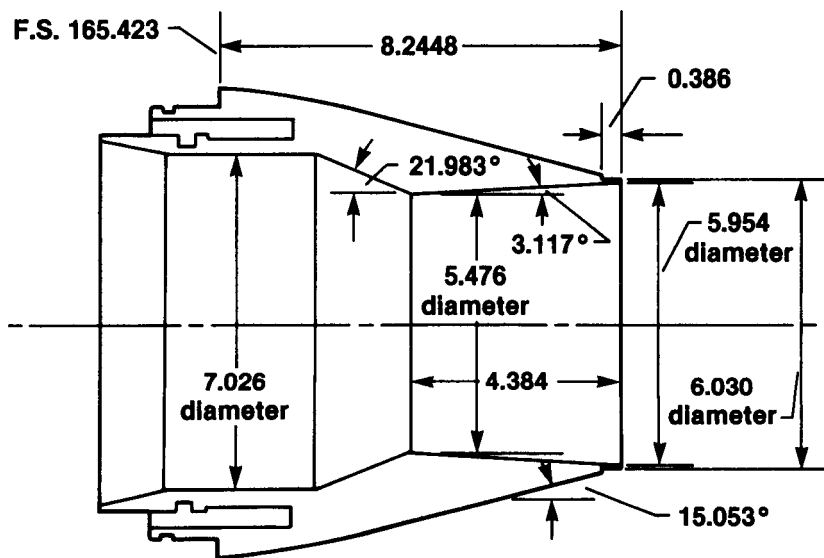
(b) *Partial afterburning power setting,*
BTL = 15.1°.

Figure 4. Drawings of the model nozzles used in the
comparison (dimensions in centimeters).
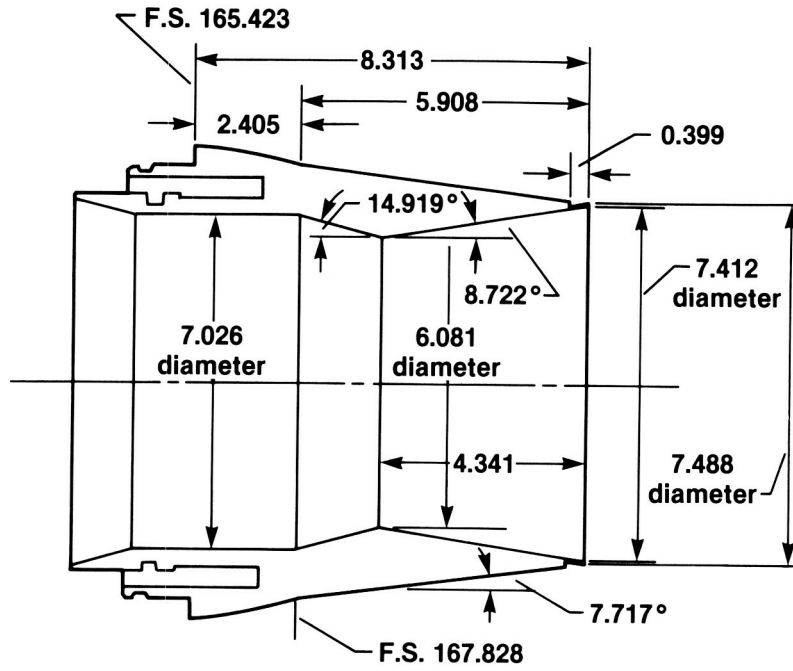
(c) Partial afterburning power setting,
BTL = 7.7°.

Figure 4. Concluded.
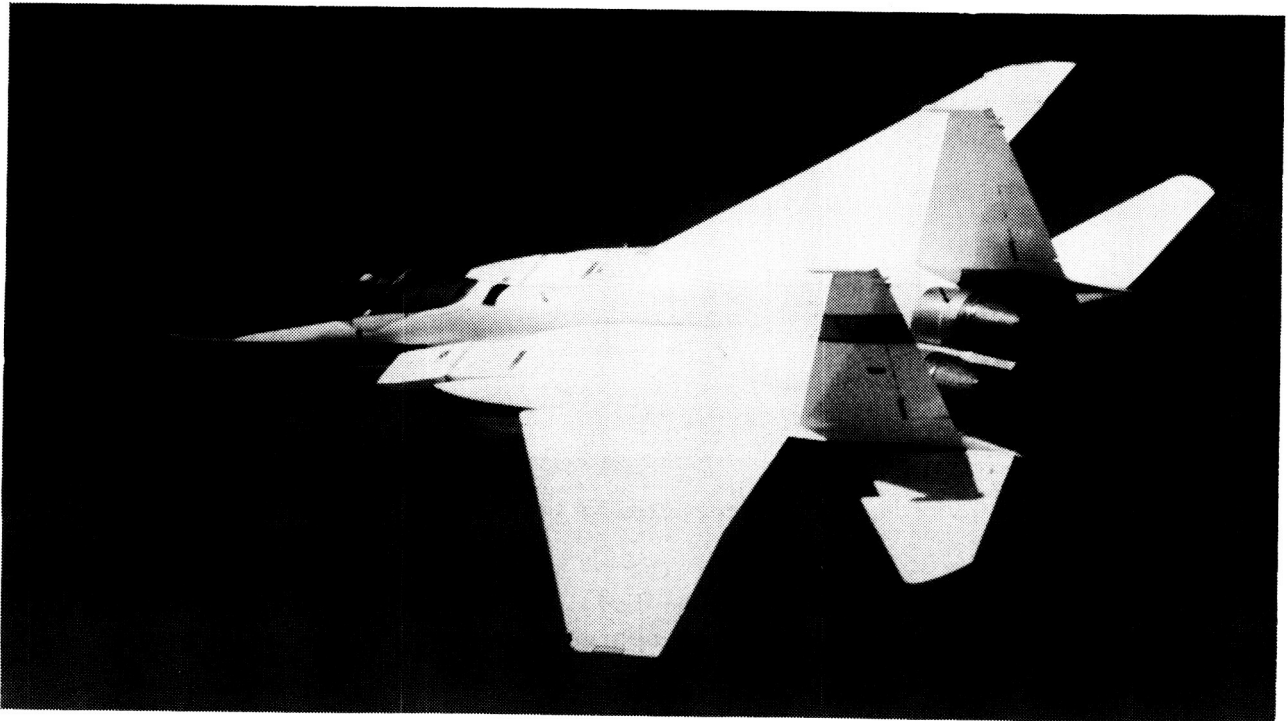
ECN 9325

Figure 5. Photograph of the F-15 airplane in flight.
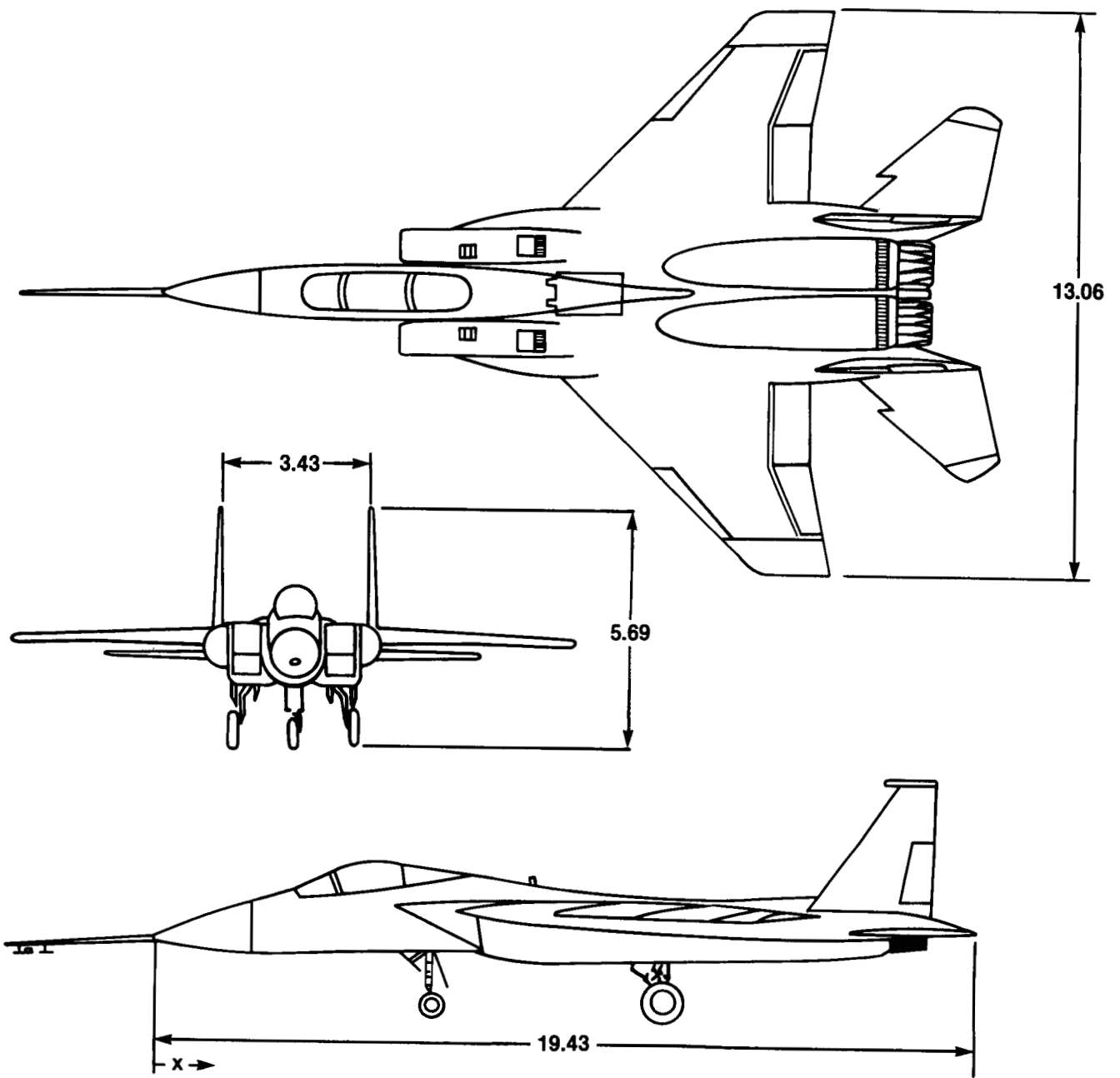
Figure 6. Three-view drawing of the F-15 airplane (dimensions in meters).
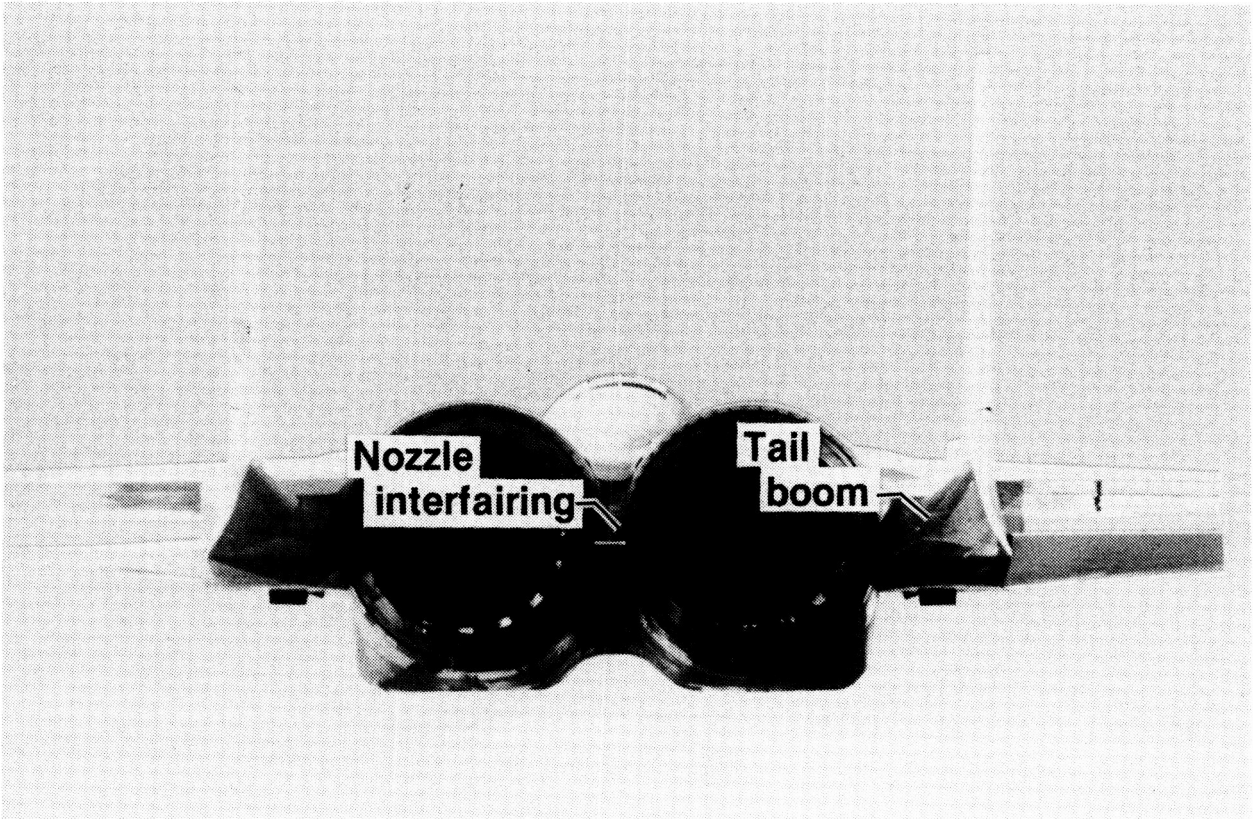
ECN 40415-001

Figure 7. Airplane afterbody showing nozzles in the military power nozzle setting.
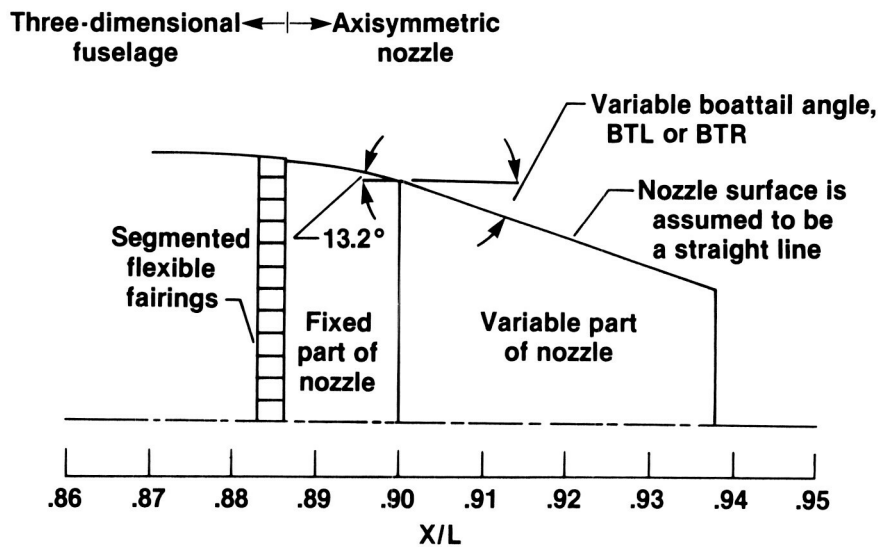
Figure 8. Details of airplane nozzle geometry.
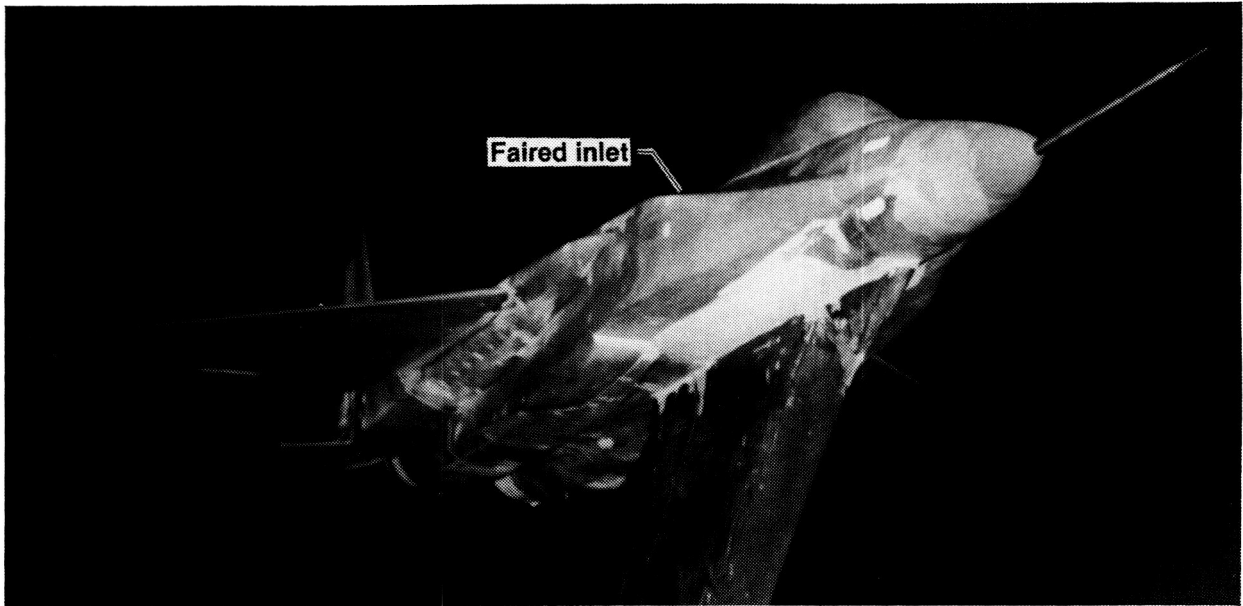
L-81-10,749

(a)   Model inlet replaced by fairing.
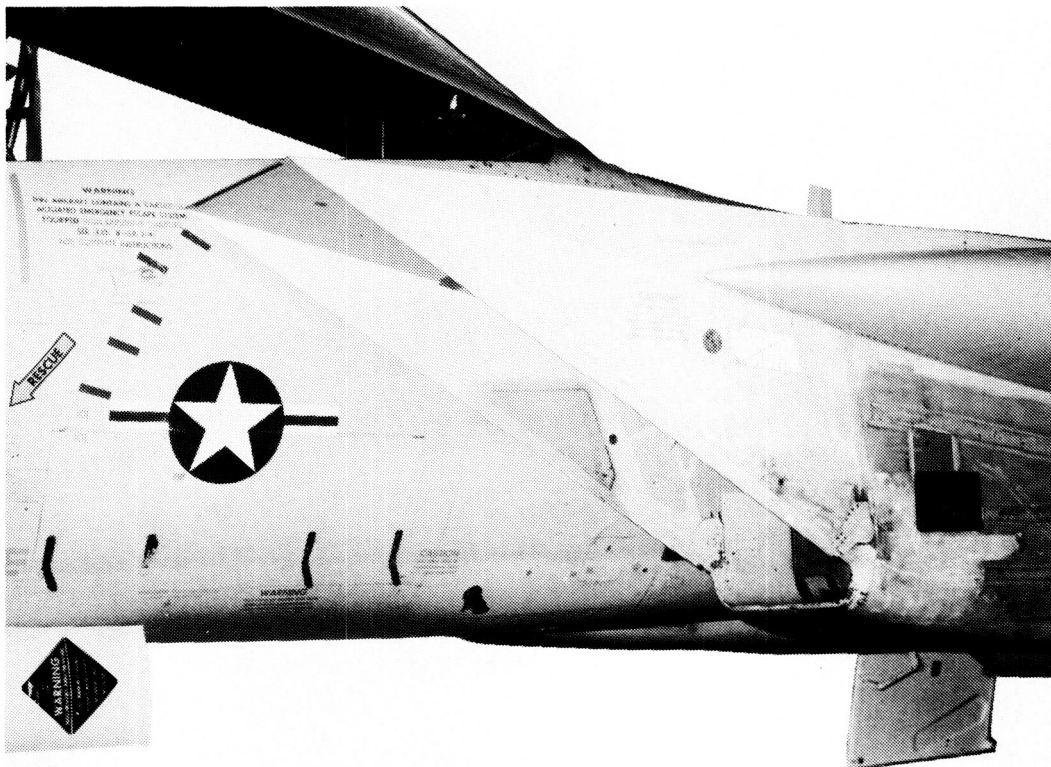
E 29406

(b)   Airplane inlet.

Figure 9.   Model and airplane inlets.
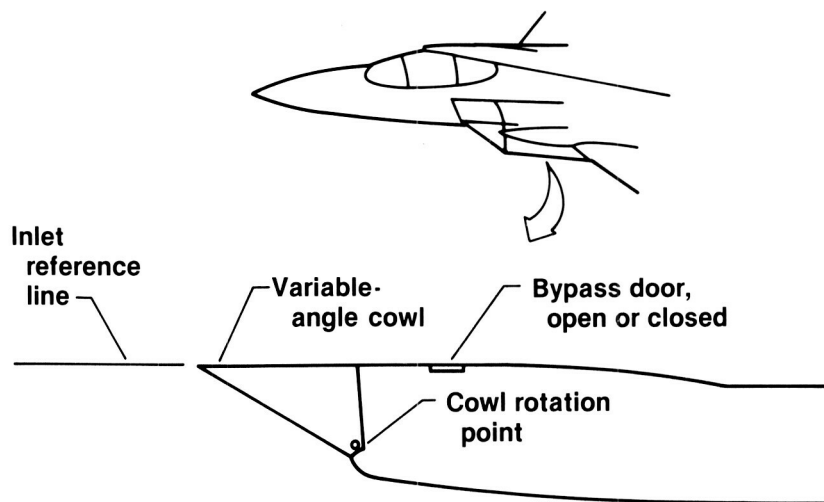
(c) Inlet variable geometry.

Figure 9. Concluded.
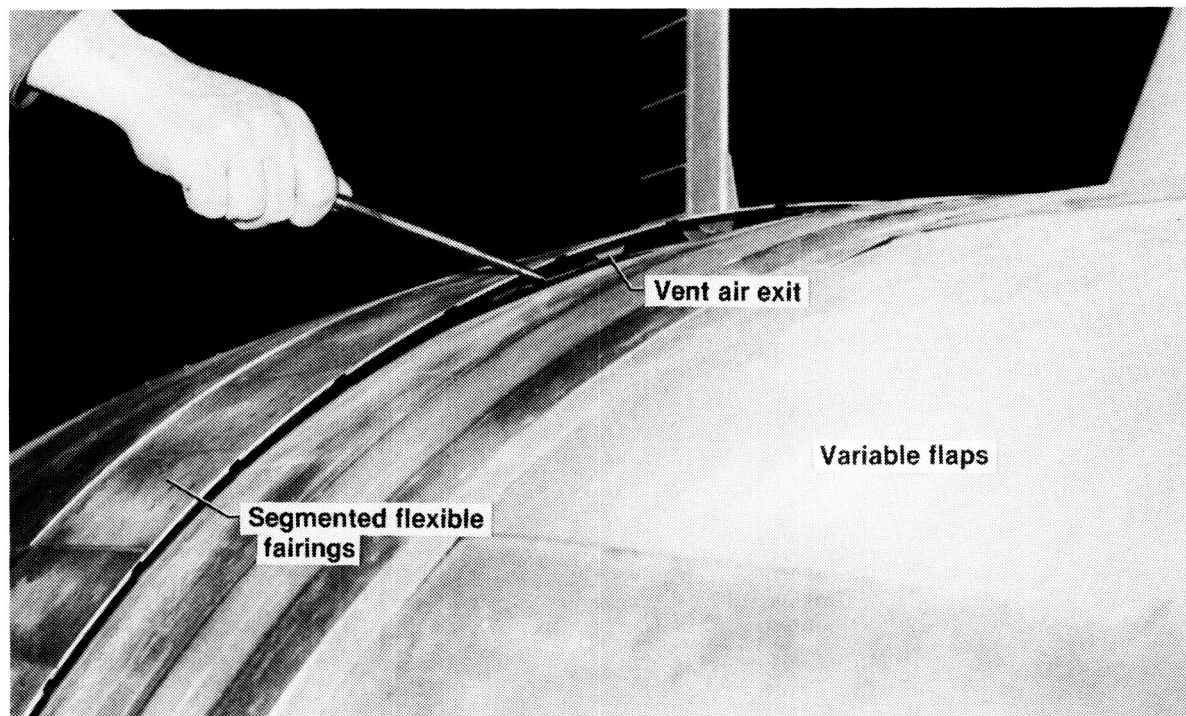
E 35115

(a) Rear view of the engine compartment air vent of F-15 airplane.

Figure 10. Engine compartment air vent.
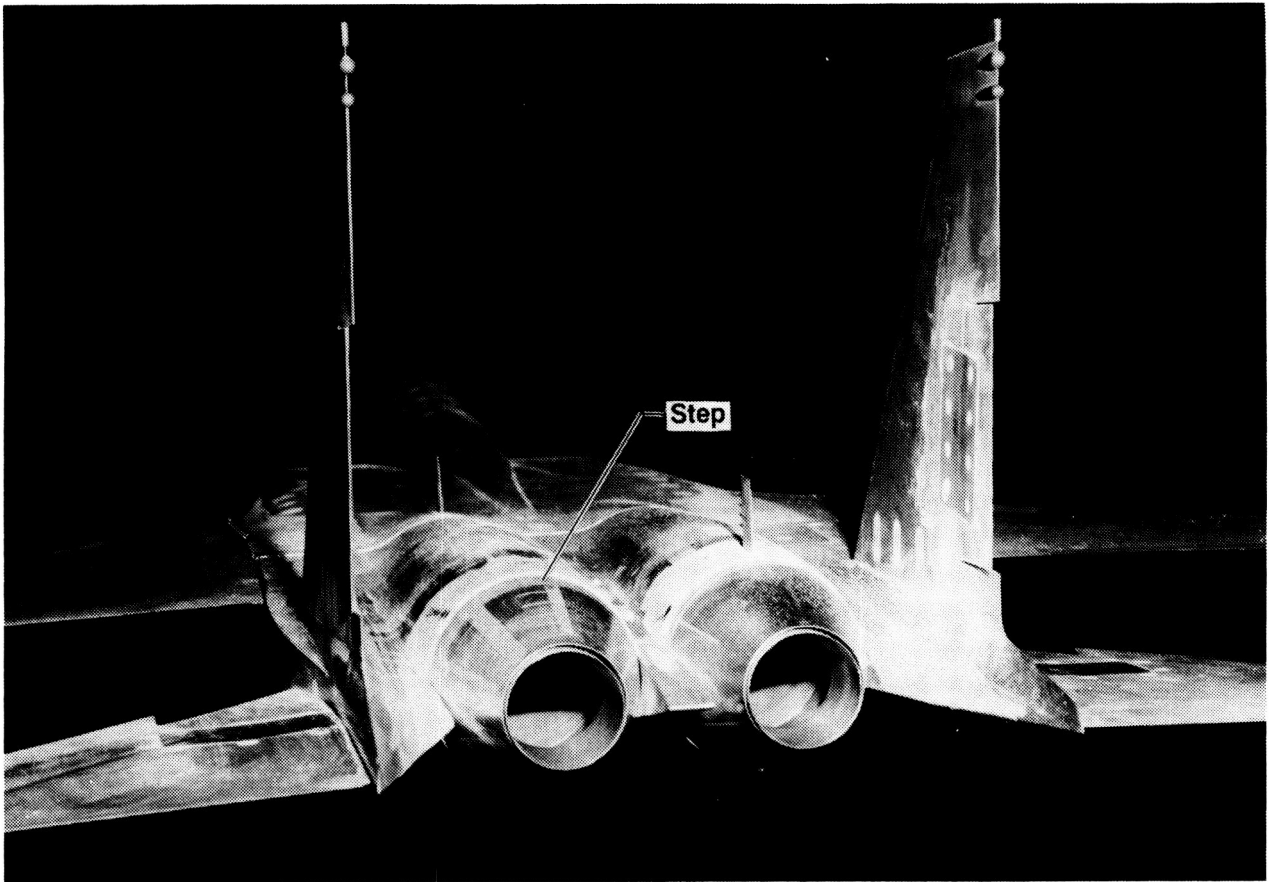
L-81-10,454

(b) Simulation of air vent on model with a rearward facing step.

Figure 10. Concluded.
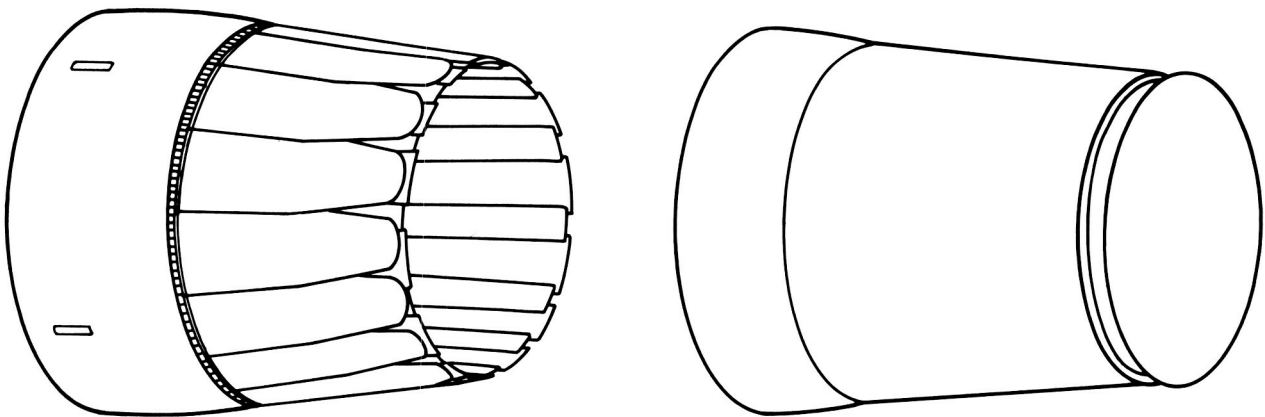
(a) Airplane.   *(b) Model.*

Figure 11. External nozzle surfaces.
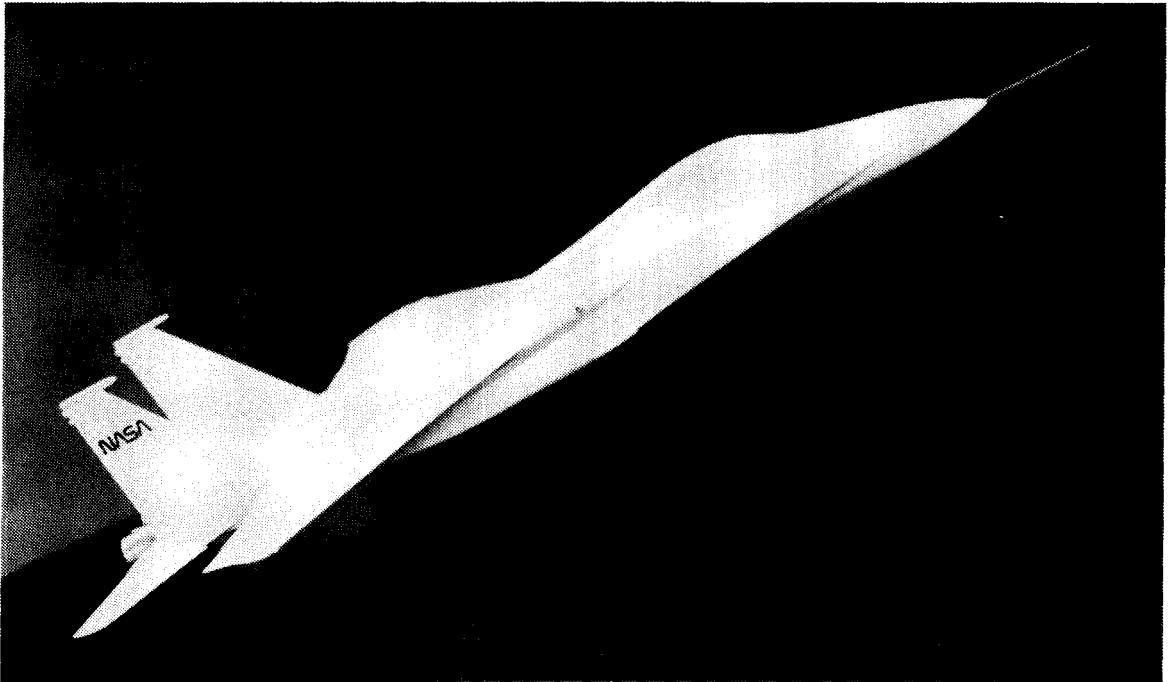
ECN 24134

(a) Faired-inlet configuration.
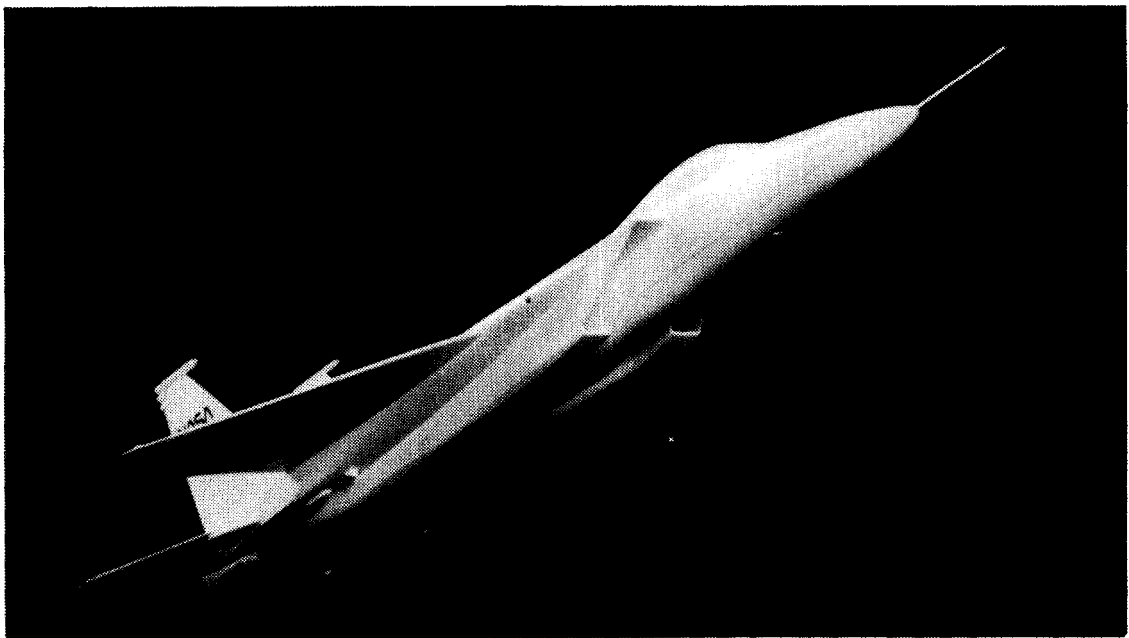
ECN 24136

(b) Flowing-inlet configuration.

Figure 12. 1/48-scale flow visualization model.

.2

.1

Upper fuselage

Y/L   0

-.1

Upper nacelle

-.2

Upper tailboom

| 0 | .1 | .2 | .3 | .4 | .5 | .6 | .7 | .8 | .9 | 1.0 |

X/L

(a)   Upper surface.

Fuel dump
vents

-.2

-.1

Lower nacelle

Y/L   0

Lower fuselage

.1

.2

| 0 | .1 | .2 | .3 | .4 | .5 | .6 | .7 | .8 | .9 | 1.0 |

X/L
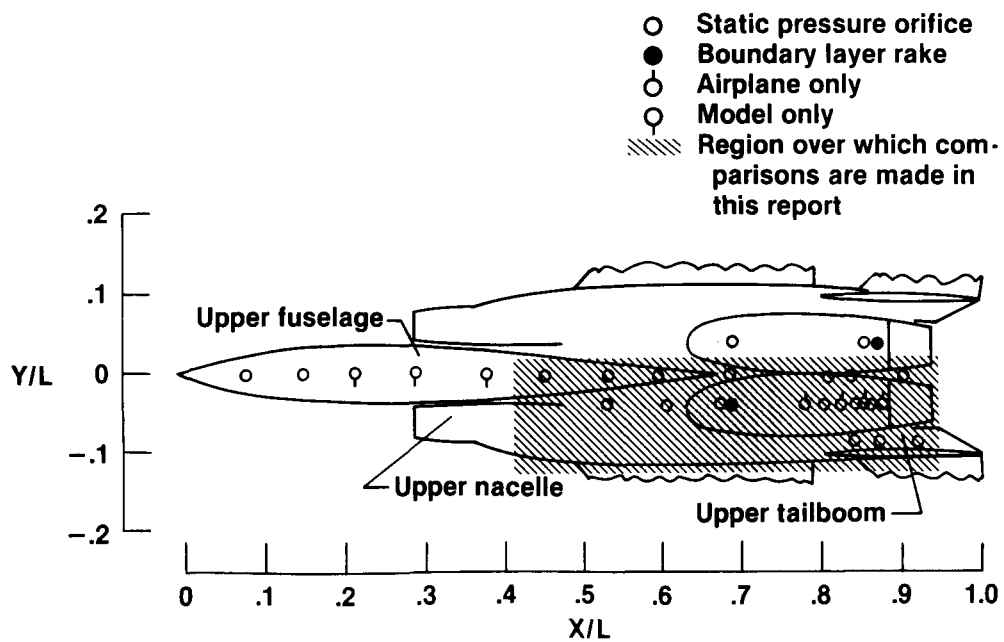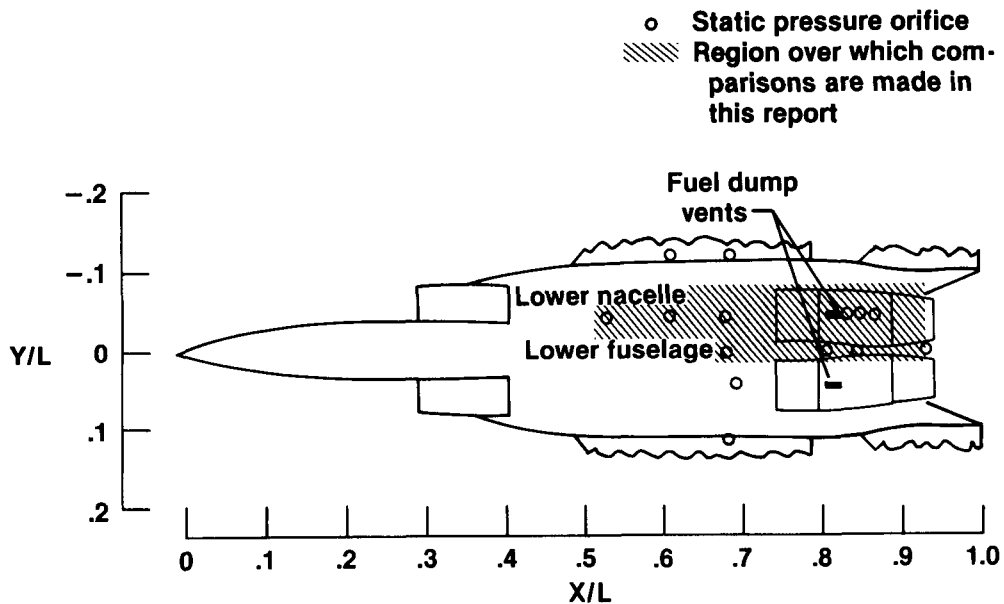
(b)   Lower surface.

Figure 13.   Fuselage surface pressure orifices.

47

X/L = 0.693
X/L = 0.707
0.635
1.397
2.286
3.556
3.454
2.463
1.955
1.498
0.965
4.13°
0.152
Model surface
Parallel to nacelle centerline

Left nacelle, X/L = 0.684

X/L = 0.871
3.048
1.524
X/L = 0.881
0.762
3.454
2.540
2.032
3.632
Parallel to nacelle centerline
1.524
0.457
1.016
5°
Model surface
0.254

Right nacelle, X/L = 0.867
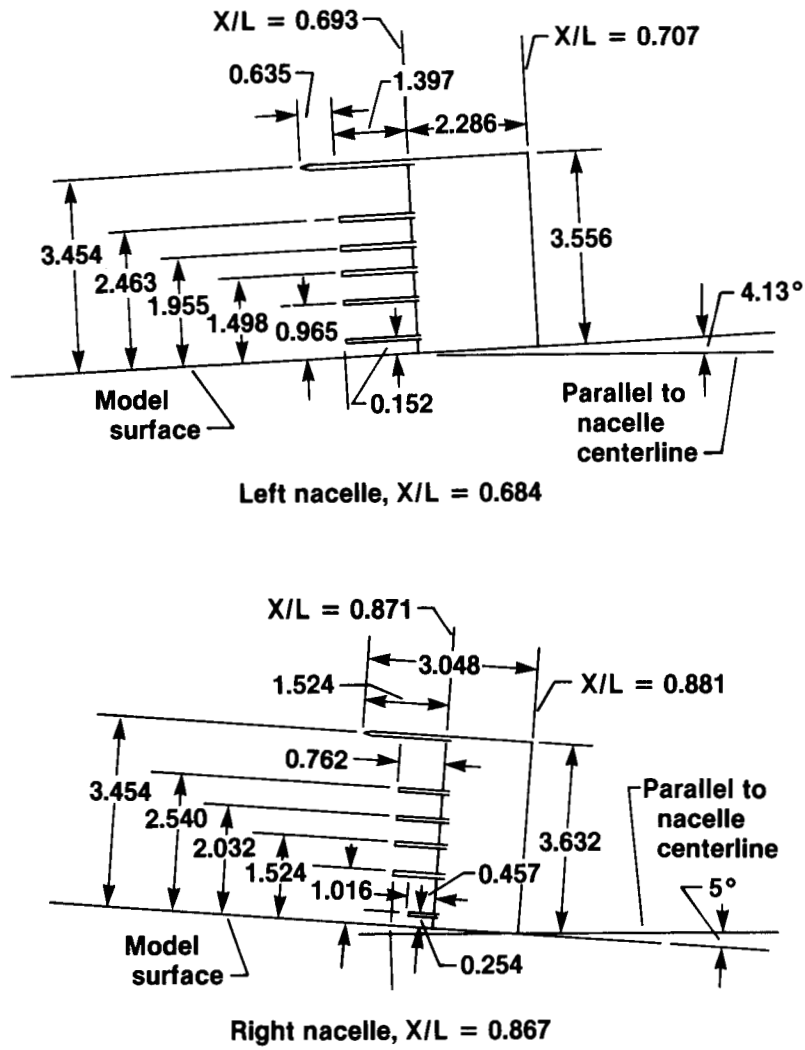
(a)   Drawings of model rakes.

Figure 14.   Boundary layer rakes (dimensions in centimeters).
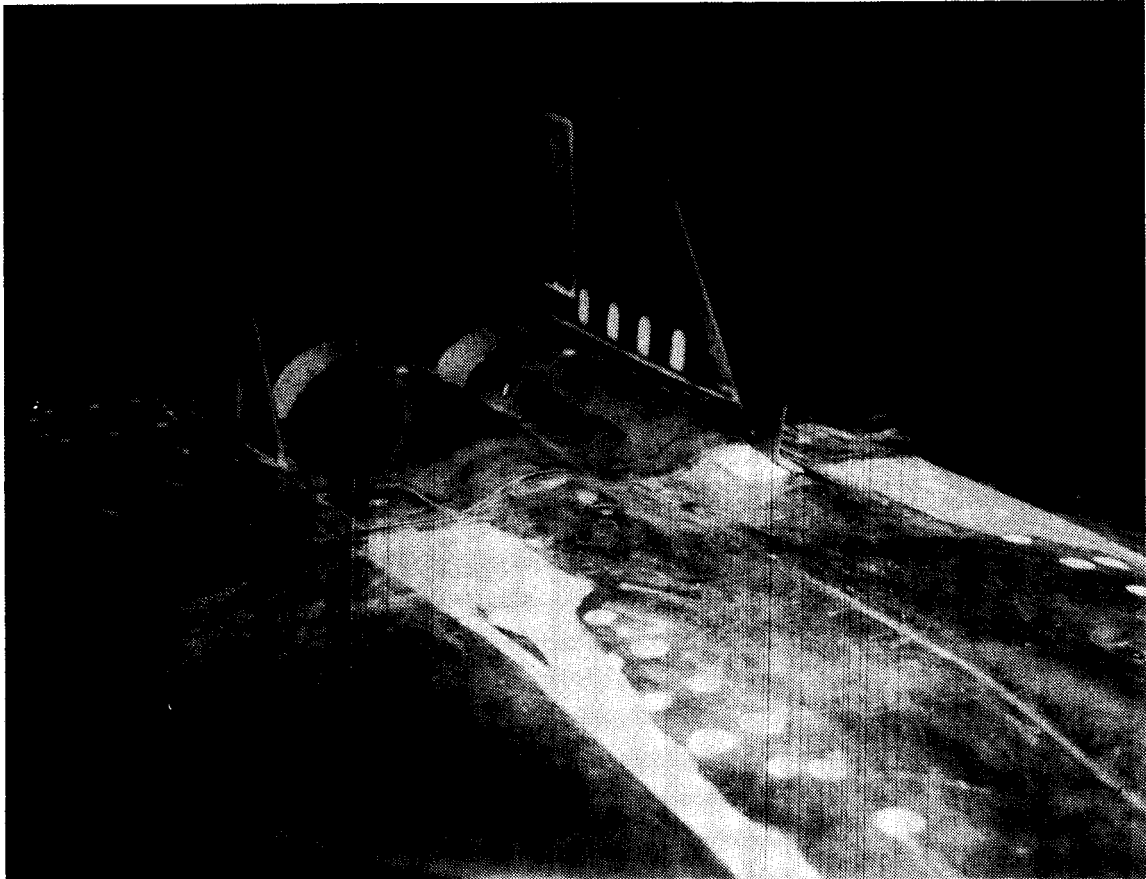
L-81-10,754

(b) Rakes installed on the model.

Figure 14. Continued.
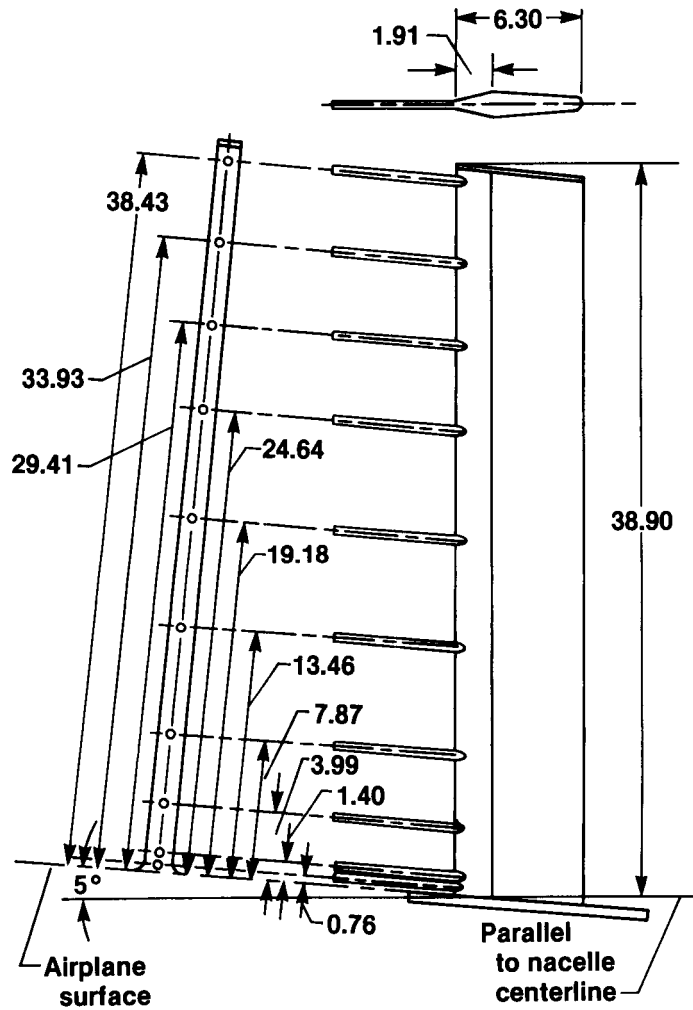
(c)   Drawing of forward airplane rake.

Figure 14.   Continued.
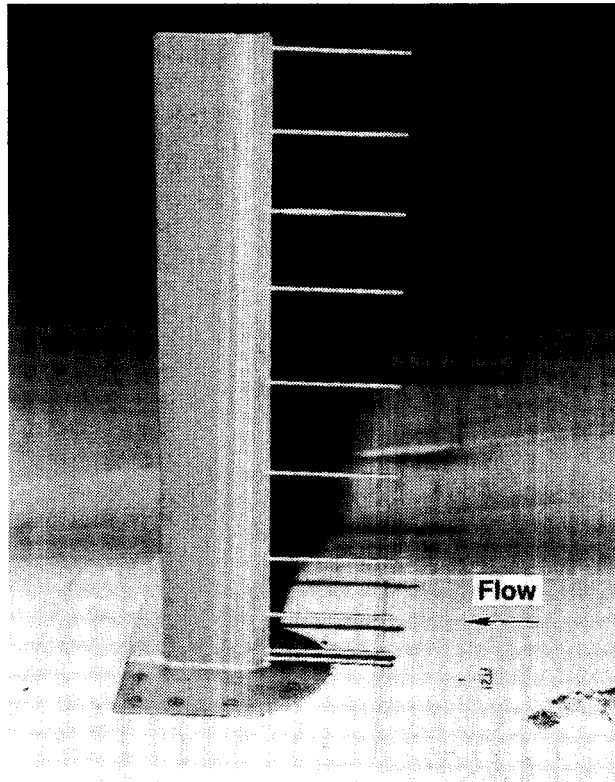
(d) Forward airplane rake on the left nacelle.

Figure 14. Concluded.
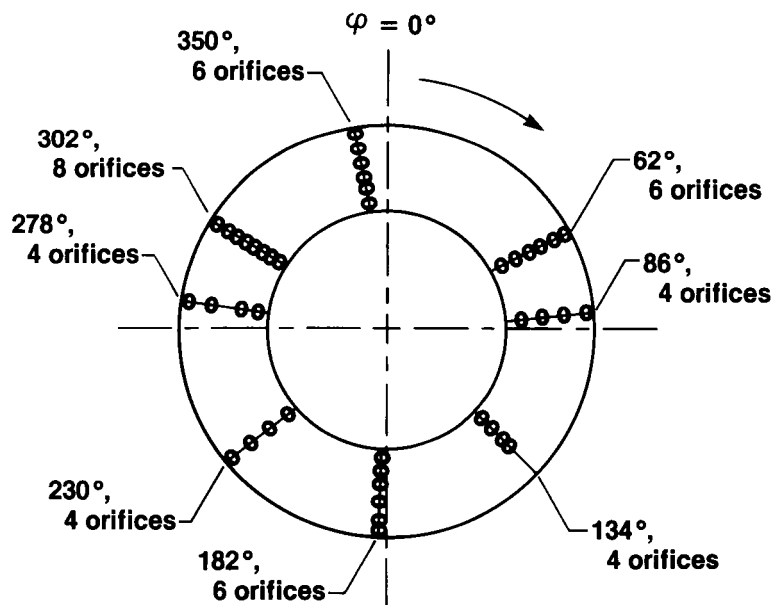
Figure 15. Angular locations of the 42 orifices on the left nozzle surfaces of the model and airplane (looking forward).
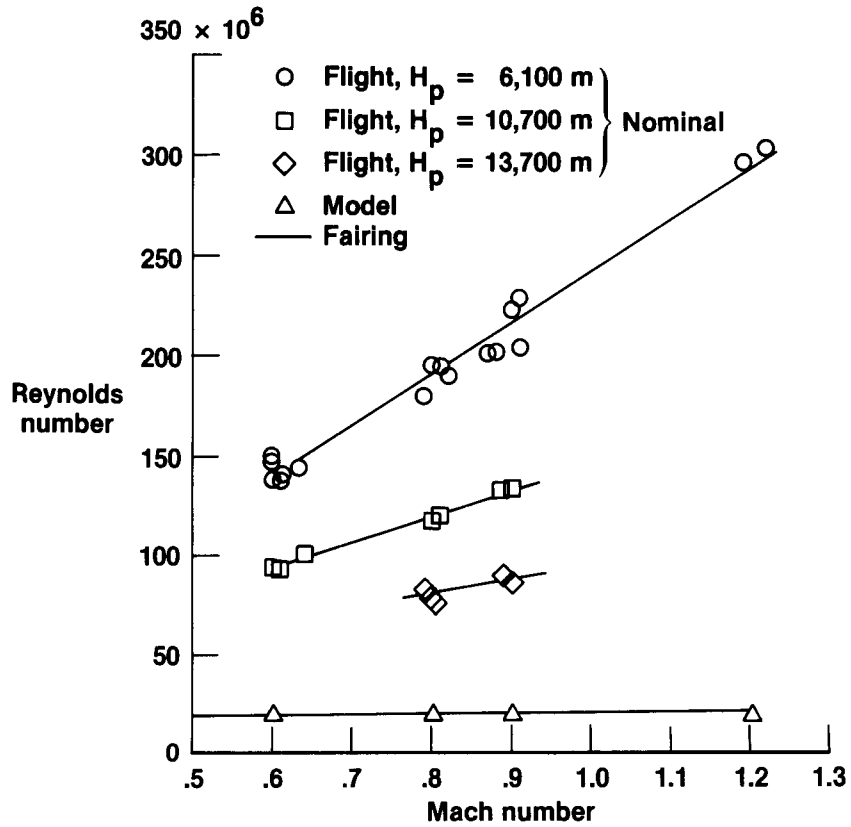
Figure 16. Variation of test Reynolds number with Mach number.
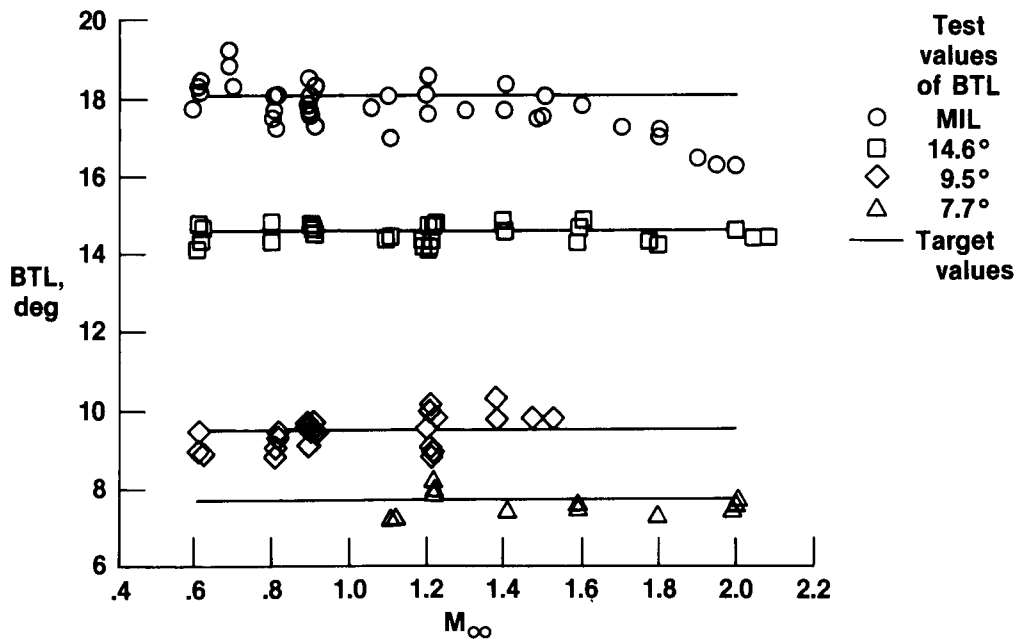
Figure 17. Typical values of left nozzle boattail angle from flight tests (from ref. 6).
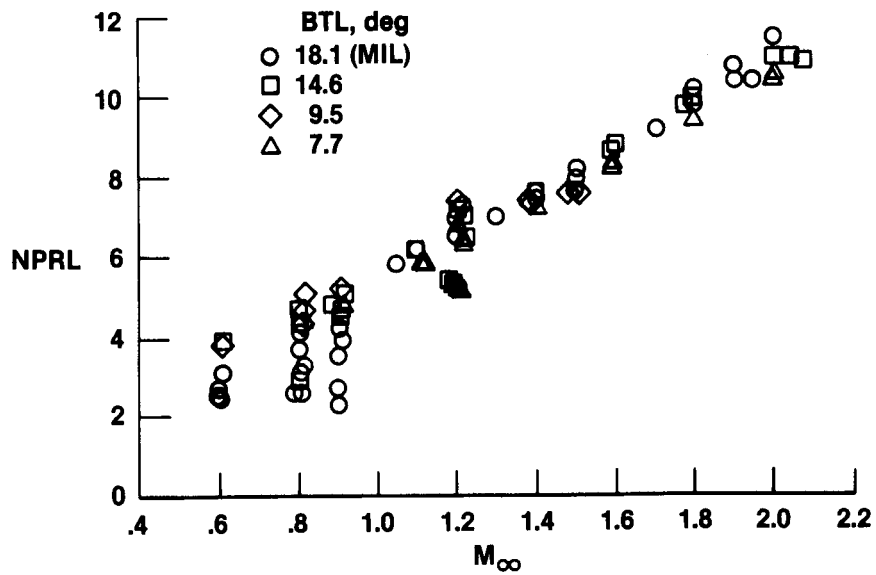
Figure 18. Variation of nozzle pressure ratio with flight test Mach number (ref. 6).
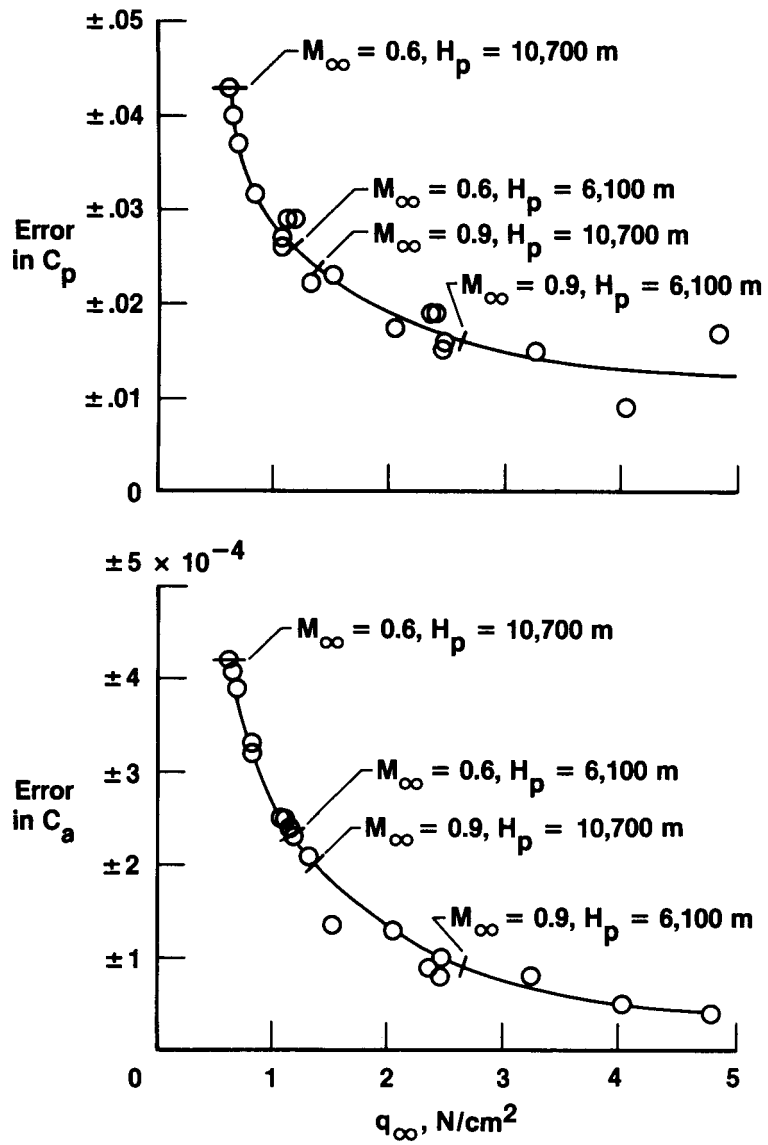
Figure 19. Variation of errors in C_a and C_p with free-stream dynamic pressure (as obtained in ref. 6).

Vehicle component influencing flow	X/L	Type of flow field
	0	
	.1	
	.2	
	.3	
Wing	.4 / .5	Expansion
	.6	
Nacelle, wing	.7	Compression
	.8	
Vertical tail, fuselage and nozzle interfairing, boattailing, nozzle geometry	.9 / 1.0	Expansion-recompression or expansion
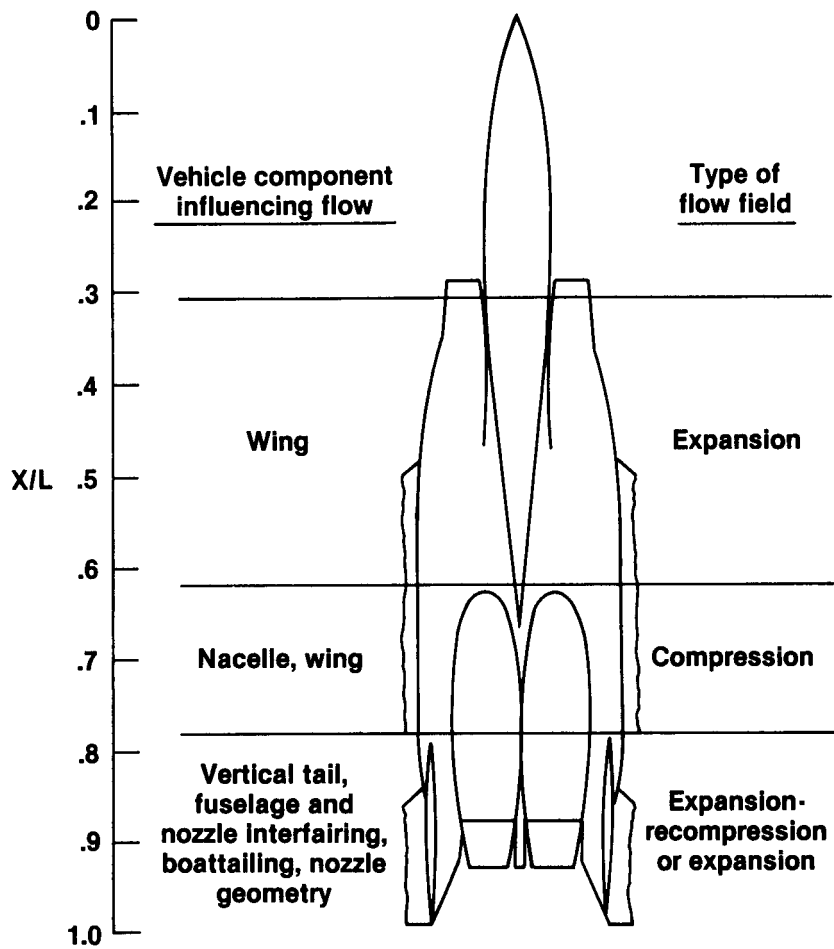
(a)   Upper fuselage.

Figure 20.   Influence of vehicle components on fuselage flow fields.

X/L	Vehicle component influencing flow	Type of flow field
0		
.1		
.2		
.3	**Vehicle component** **influencing flow**	**Type of** **flow field**
.4		
.5		
.6	**Nacelle, wing**	**Compression**
.7		
.8	**Fuselage and** **nozzle interfairing,** **boattailing, nozzle** **geometry**	**Expansion·** **recompression** **or expansion**
.9		
1.0		
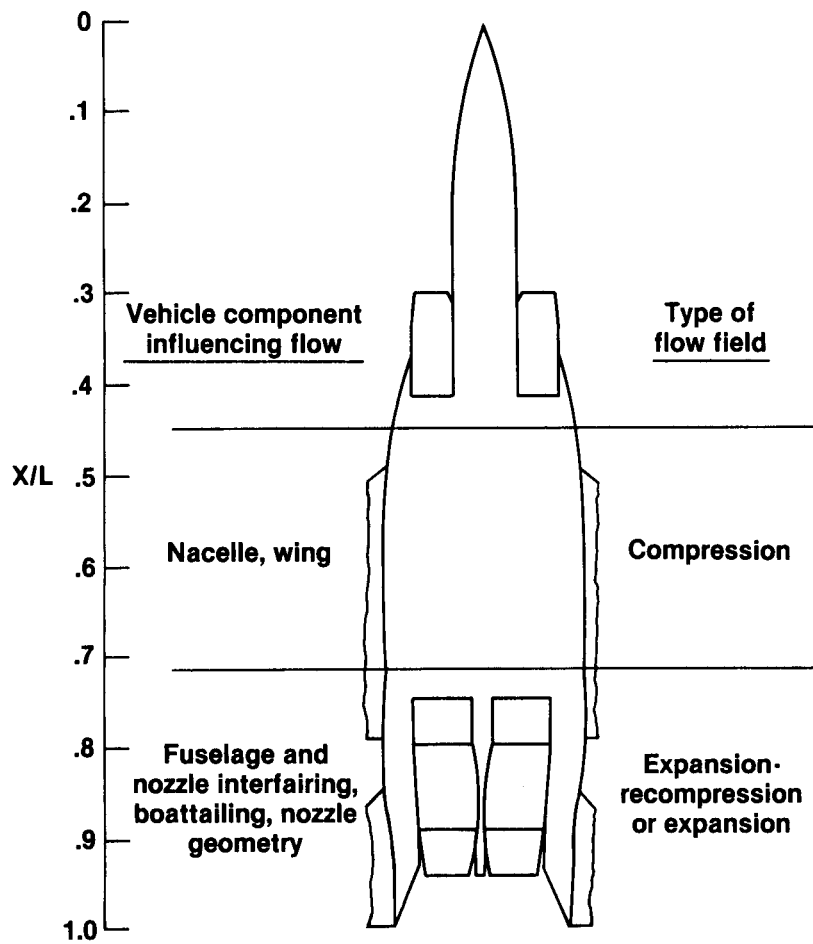
(b) *Lower fuselage.*

Figure 20. Concluded.
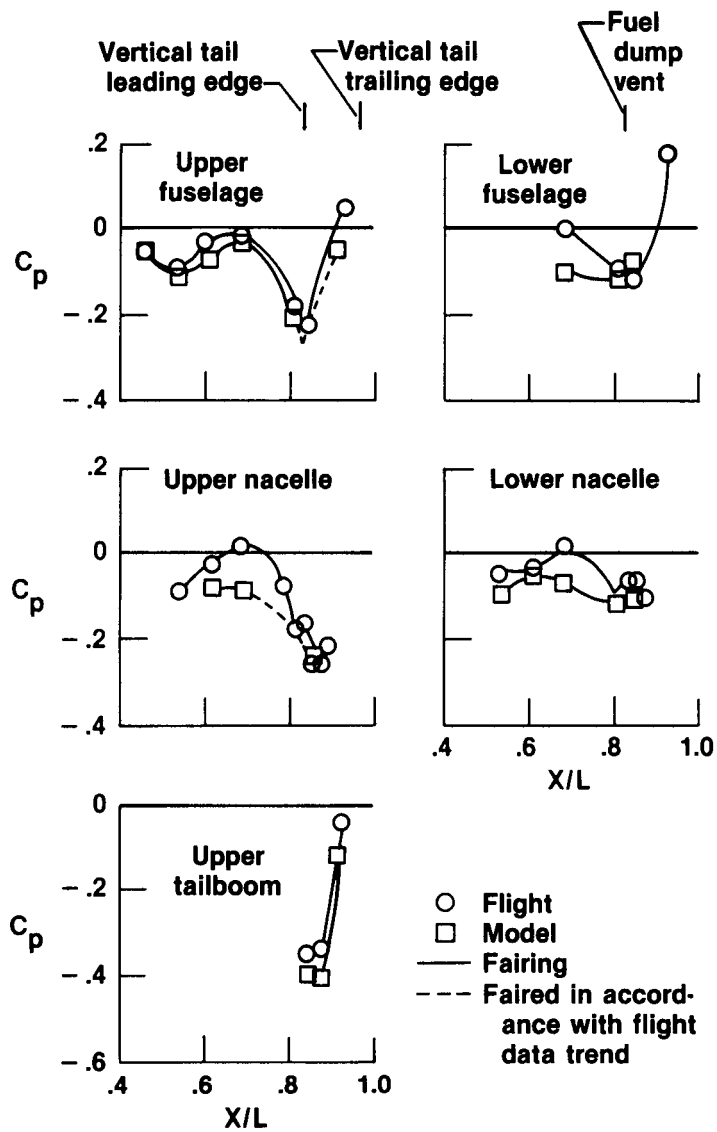
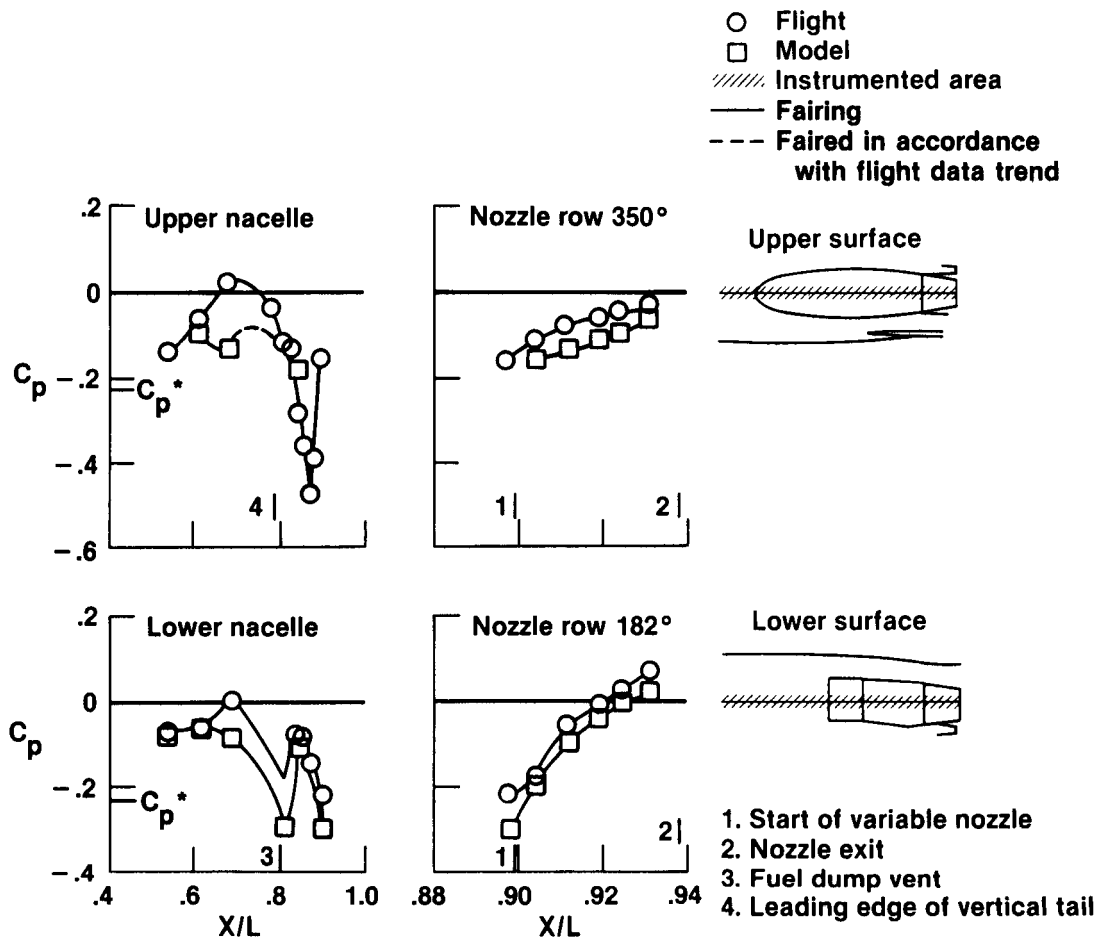*(a)* $M_\infty \approx 0.6$; $BTL \approx 18.4°$; $BTR \approx 18.4°$; and $NPRL \approx 3.0$.

Figure 21. Comparison of afterbody pressure coefficient distributions as Mach number is varied at $\alpha \approx 1°$.
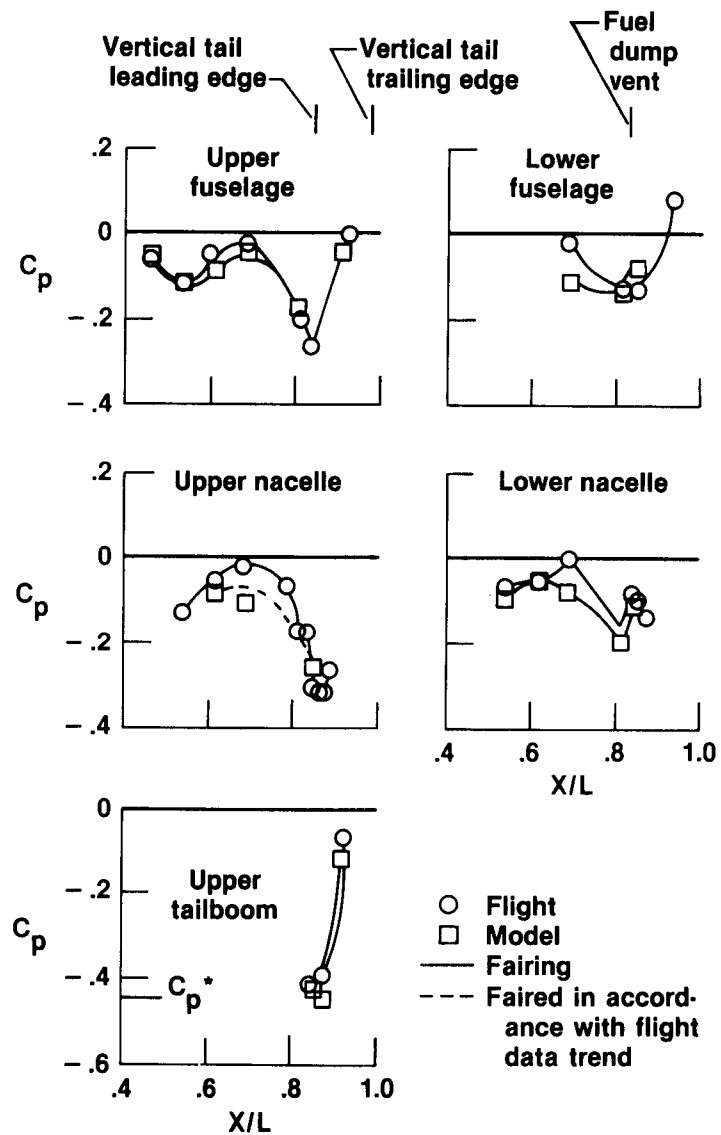
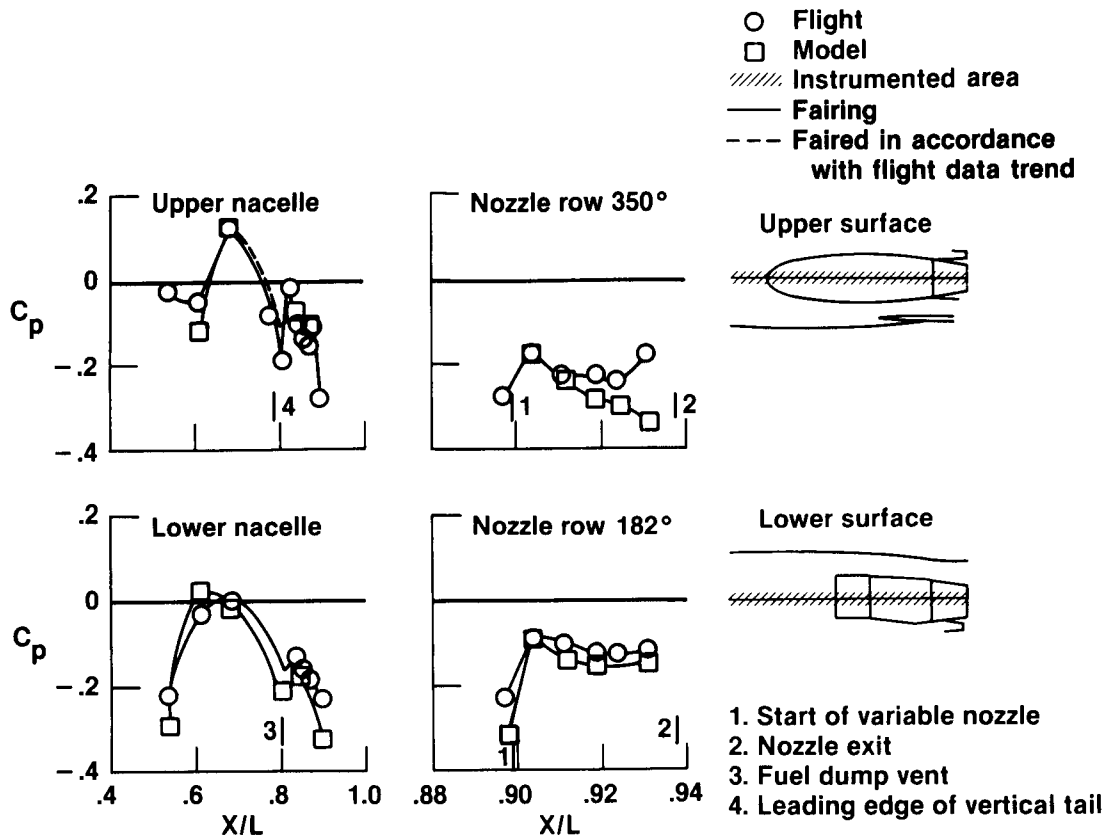(b) $M_\infty \approx 0.8$; BTL $\approx 18.4°$; BTR $\approx 18.4°$ to 19.5°; and NPRL ≈ 2.0 to 3.0.
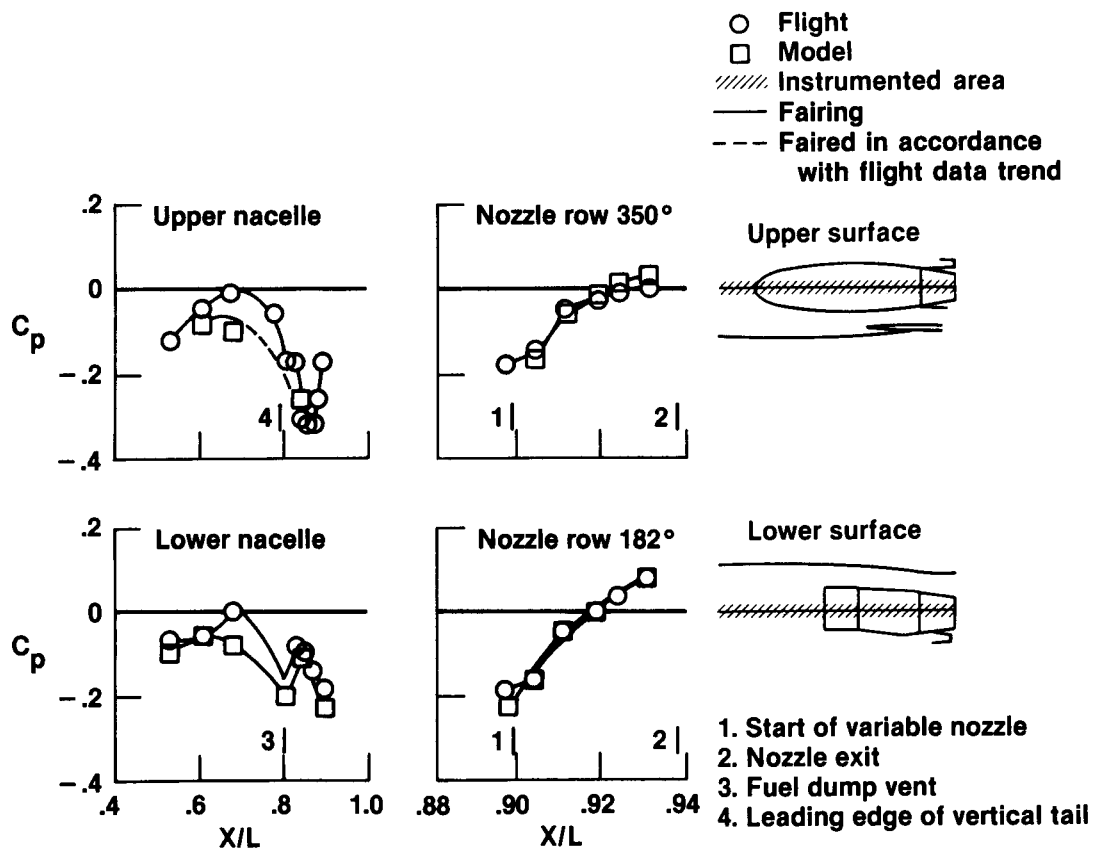
Figure 21. Continued.
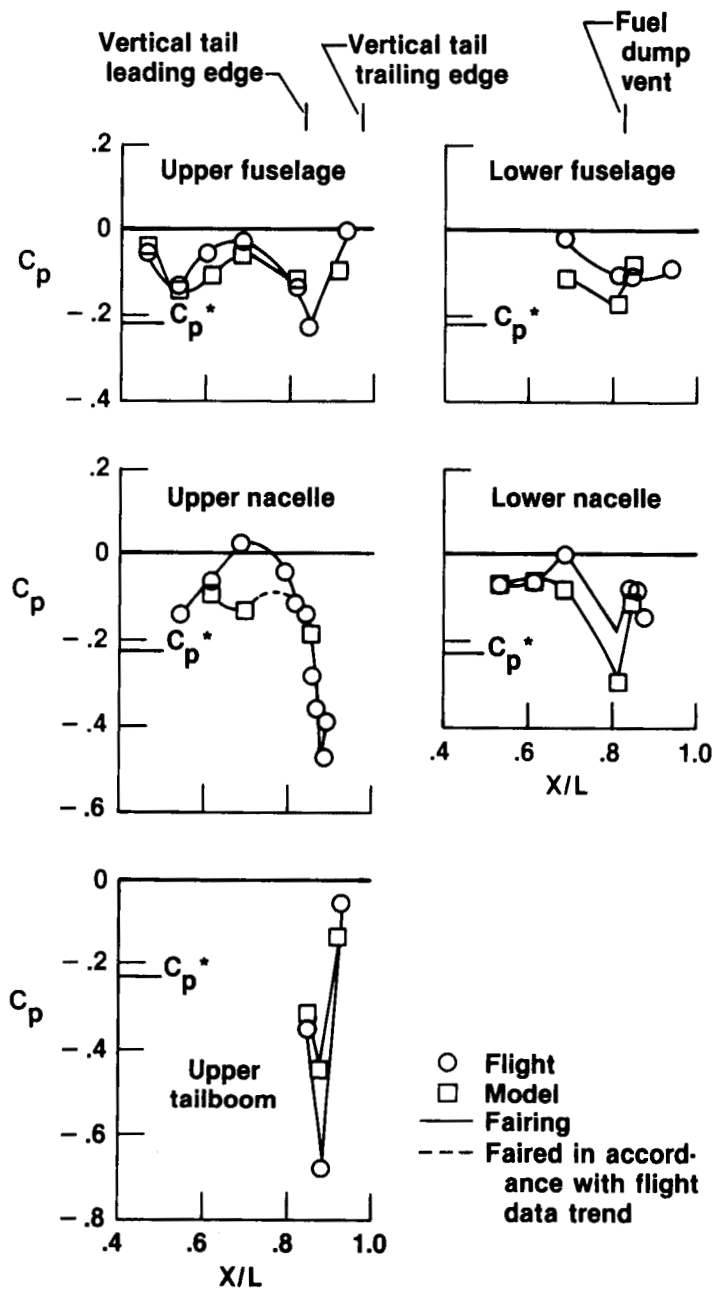
(c) $M_\infty \approx 0.9$; $BTL \approx 18.4°$; $BTR \approx 18.4°$ to $19.7°$; and $NPRL \approx 2.0$ to 3.0.

Figure 21. Continued.
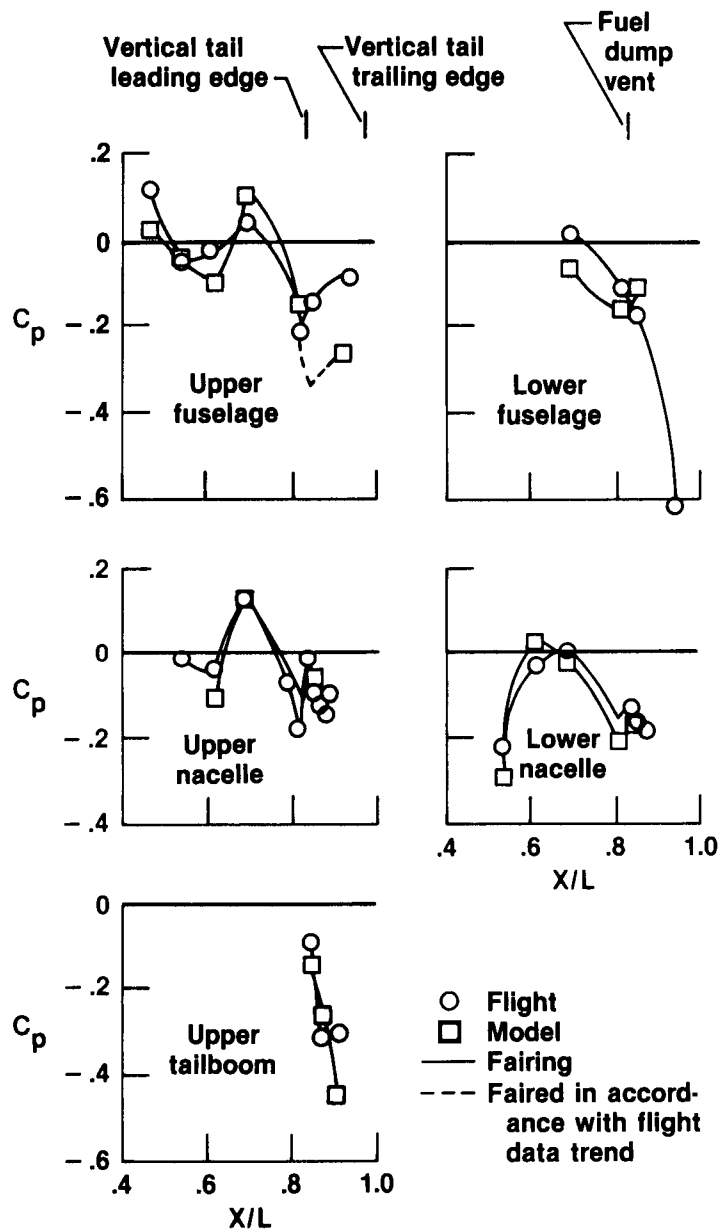
(d) $M_\infty \approx 1.2$; BTL $\approx 7.7°$; BTR $\approx 7.7°$; and NPRL ≈ 5.0.

Figure 21. Concluded.
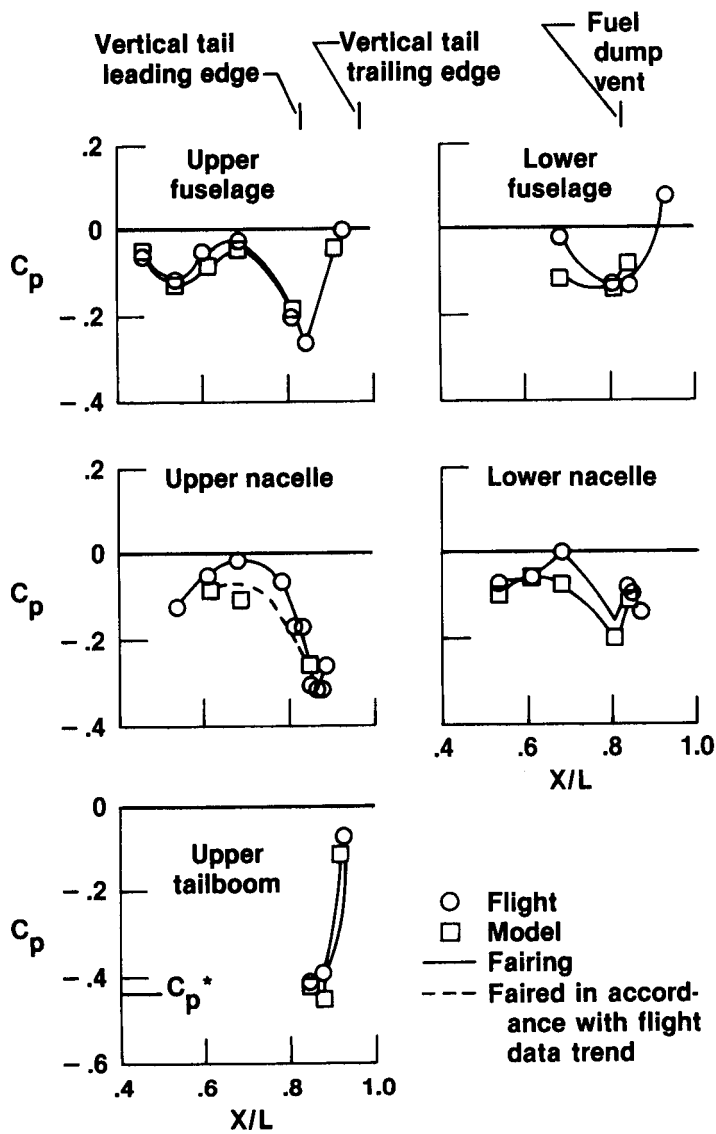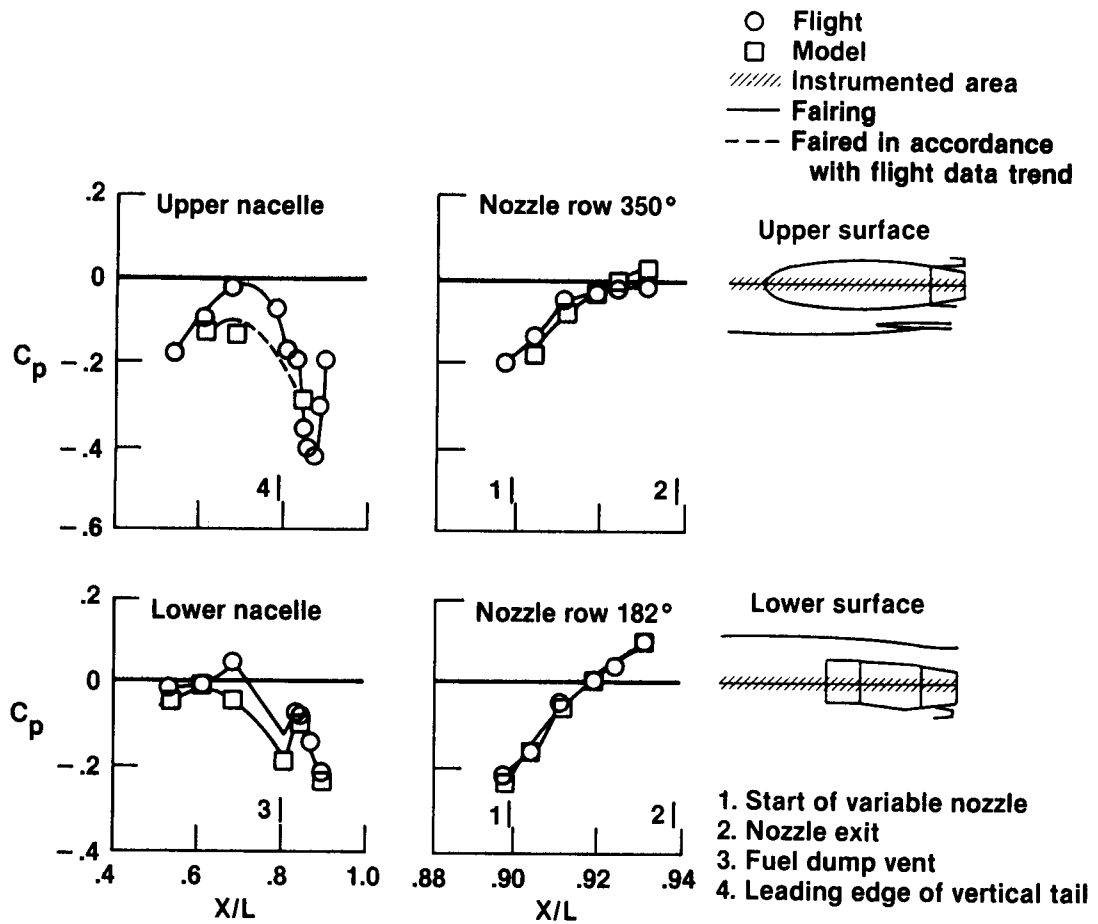
(a) $\alpha \approx 1°$; $BTL \approx 18.4°$; $BTR \approx 18.4°$ to $19.5°$; and $NPRL \approx 3.0$.

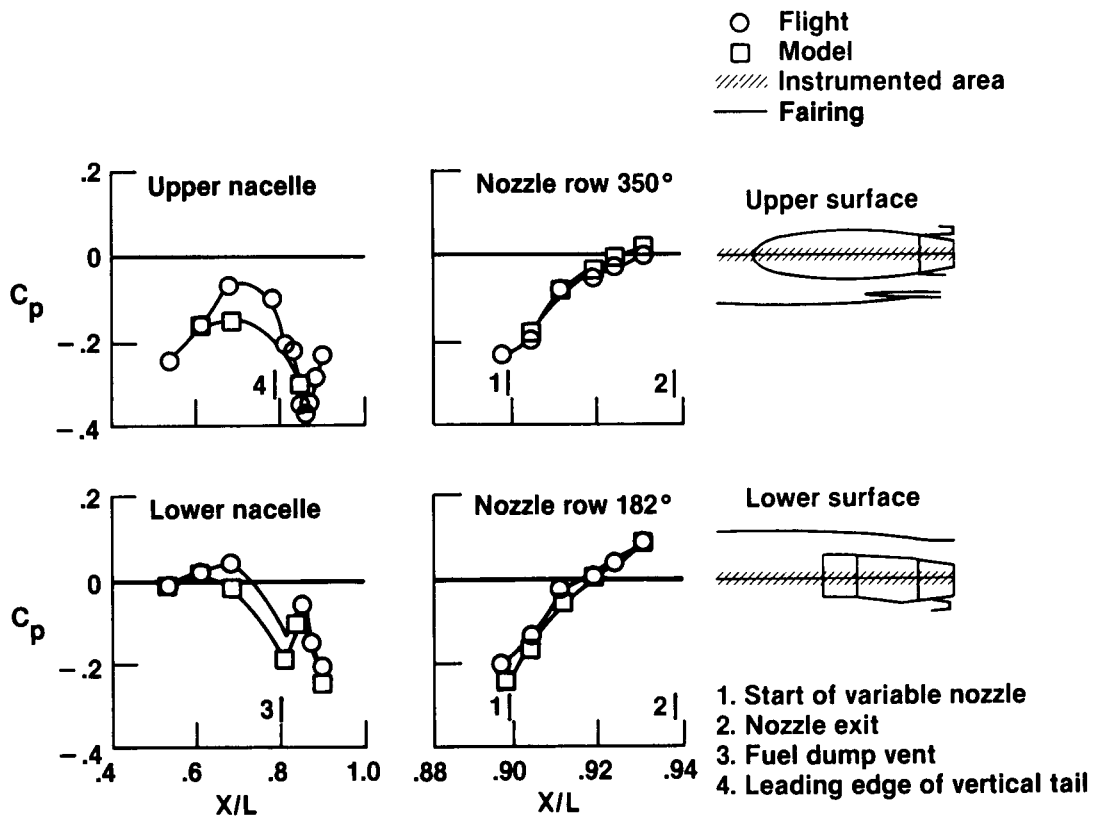*Figure 22. Comparison of afterbody pressure coefficient distributions as angle of attack is varied at $M_\infty \approx 0.8$.*
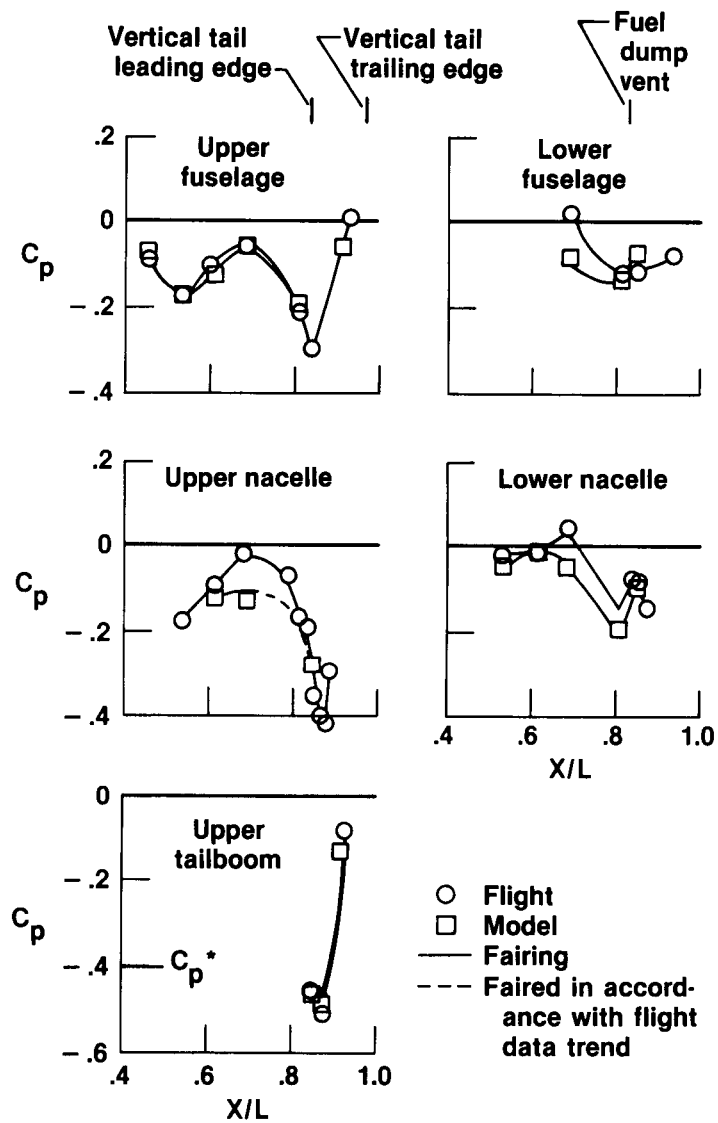
(b) α ≈ 3°; BTL ≈ 18.4°; BTR ≈ 18.4° to
16.0°; and NPRL ≈ 2.5.

Figure 22. Continued.
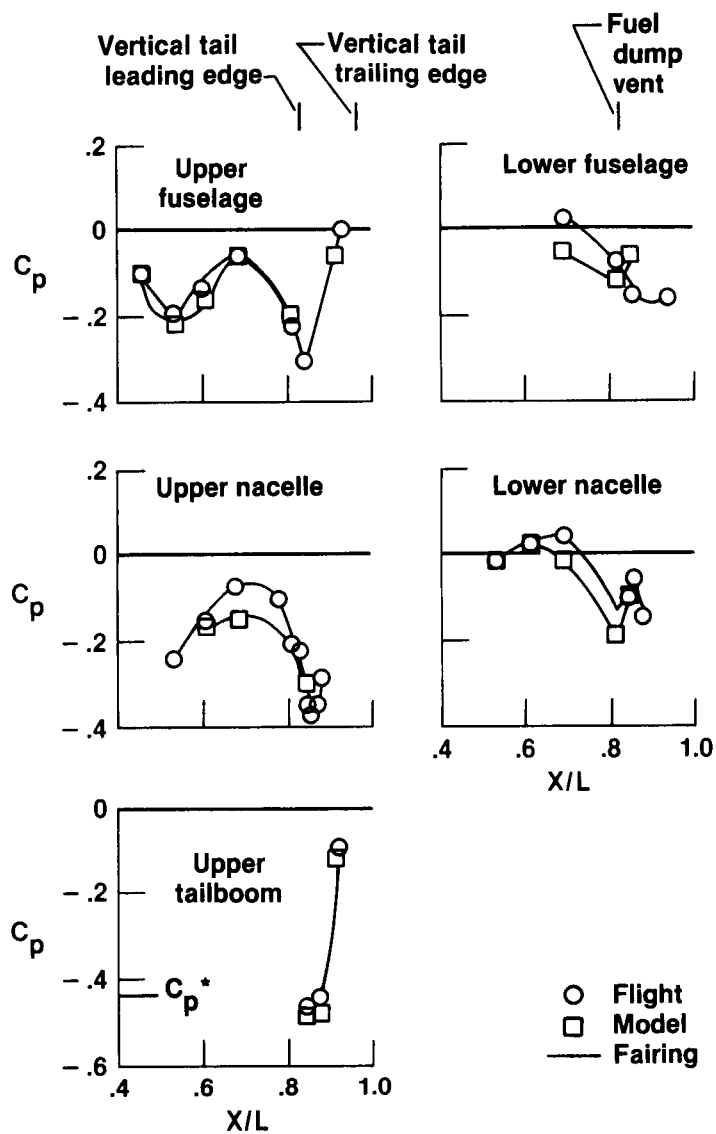
Figure 22. Continued.

(c) $\alpha \approx 5°$; BTL $\approx 18.4°$; BTR $\approx 18.4°$ to 19.2°; and NPRL ≈ 2.5 to 3.7.
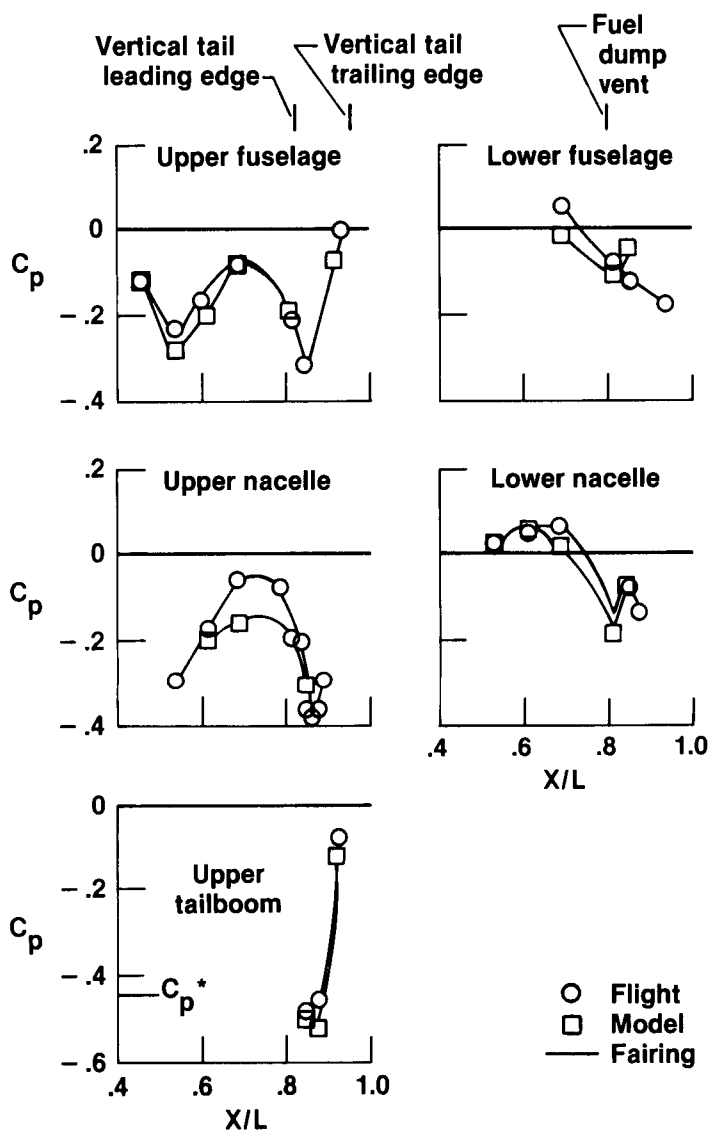
(d) α ≈ 6° to 7°; BTL ≈ 17.8° to 18.4°;
BTR ≈ 18.4; and NPRL ≈ 3.0 to 3.5.

Figure 22. Concluded.
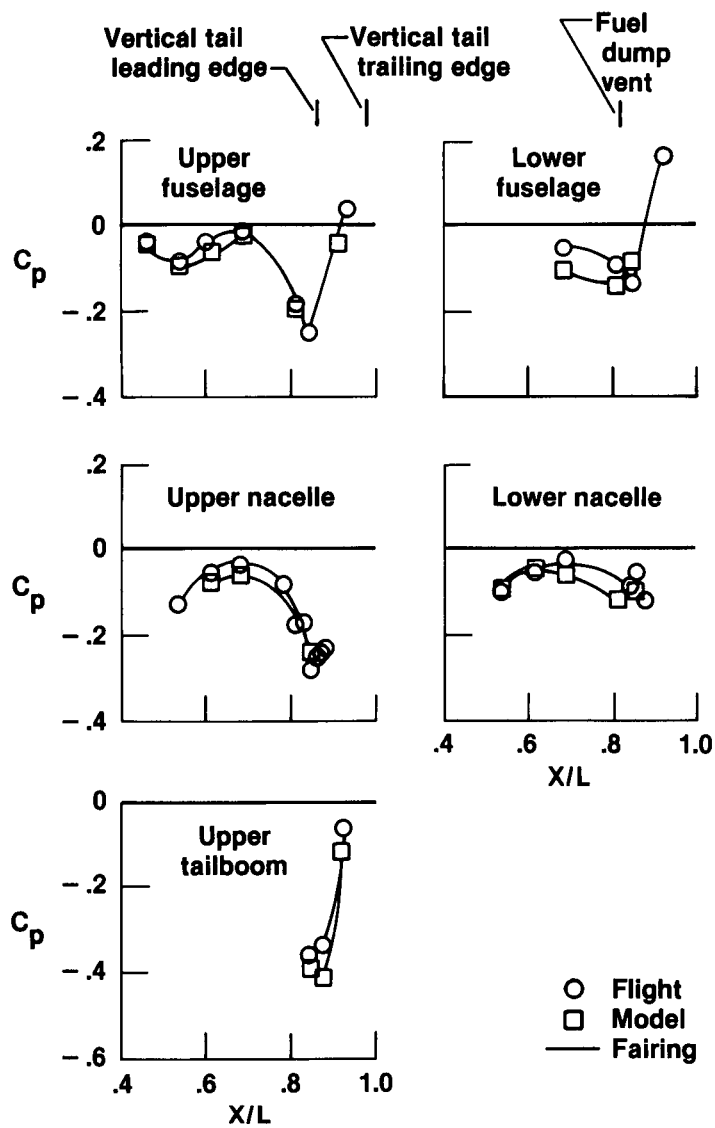
(a) $M_\infty \approx 0.6$; BTL $\approx 15.1°$; BTR $\approx 18.4°$ to 19.5°; and NPRL ≈ 4.0.

Figure 23. Comparison of afterbody pressure coefficient distributions as left nozzle boattail angle is varied at α ≈ 1° to 2°.
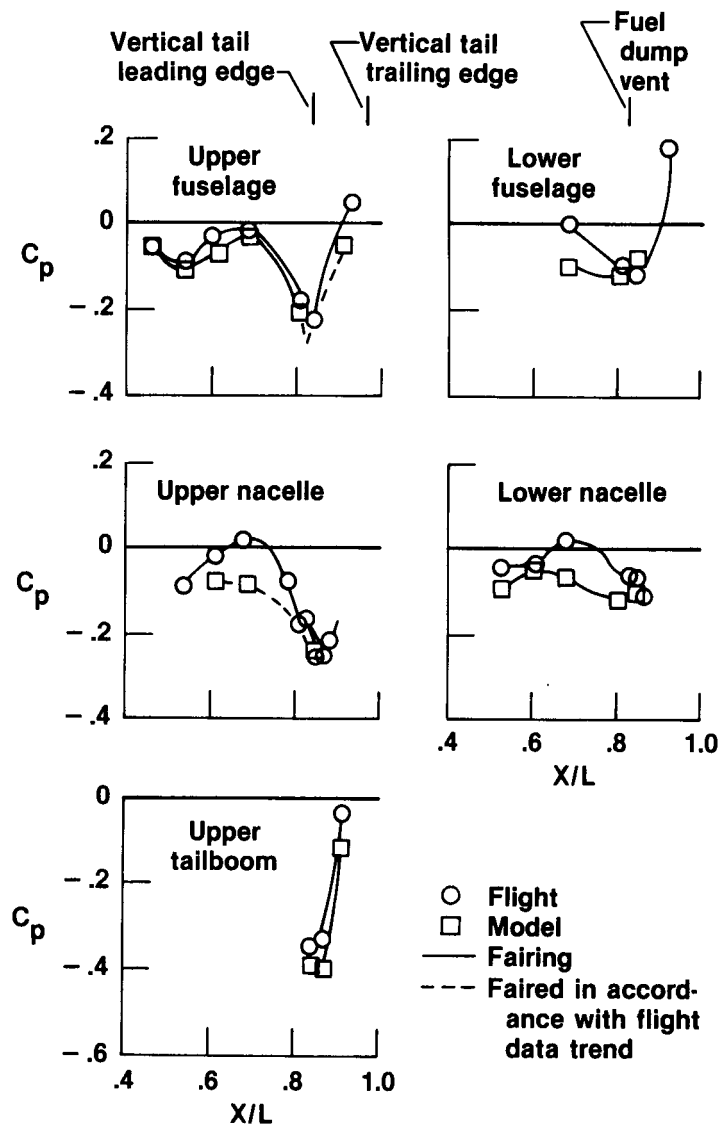
(b) $M_{\infty} \approx 0.6$; *BTL* $\approx 18.4°$; *BTR* $\approx 18.4°$ *to* $19.5°$; *and NPRL* ≈ 3.0.

Figure 23. Continued.
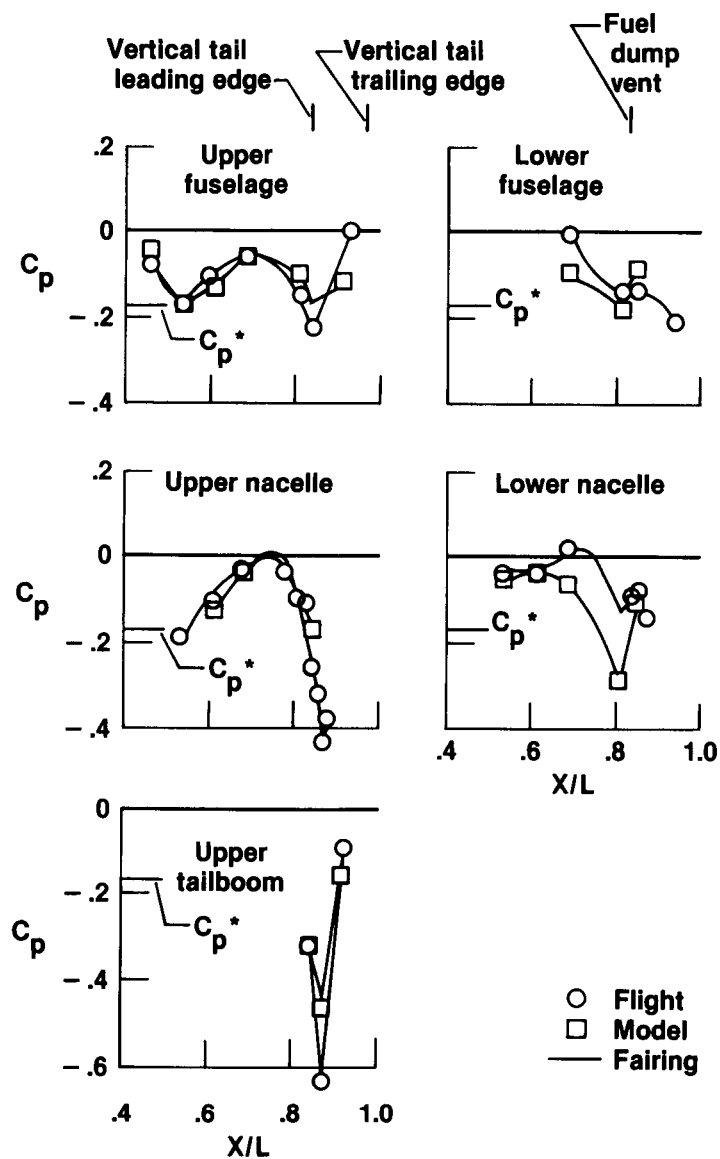
(c) $M_\infty \approx 0.9$; BTL $\approx 15.1°$; BTR $\approx 18.4°$ to
19.5°; and NPRL ≈ 5.0.

Figure 23. Continued.
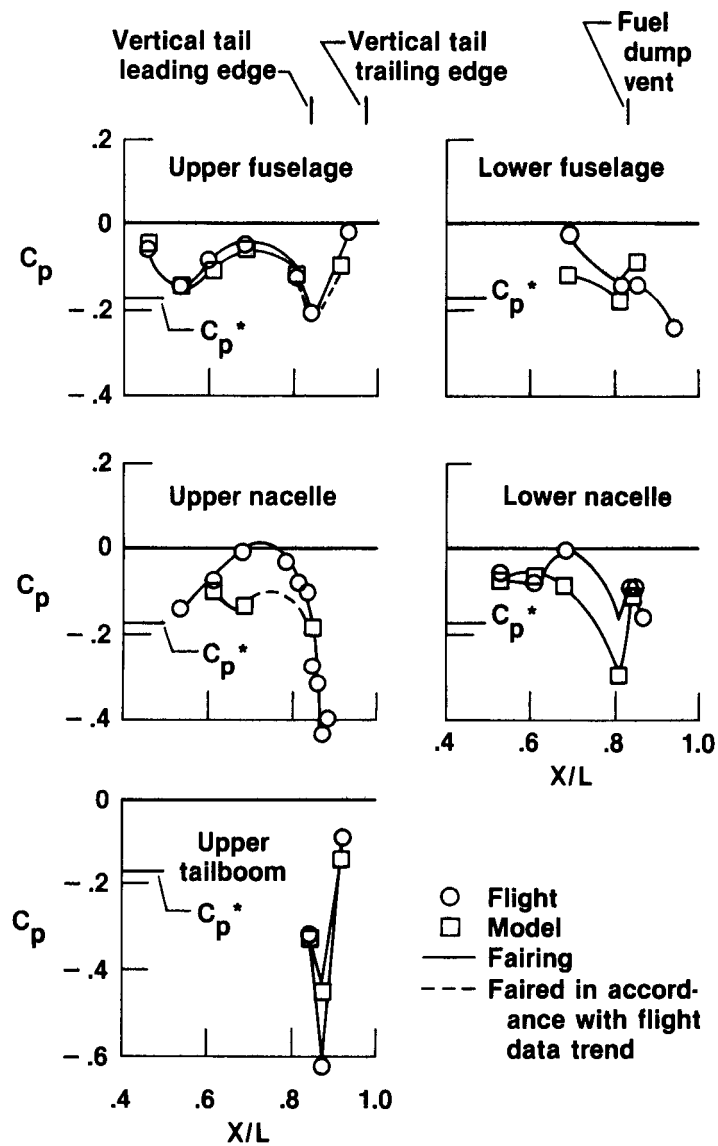
(d) $M_\infty \approx 0.9$; BTL $\approx 18.4°$; BTR $\approx 18.4°$ to 15.4°; and NPRL ≈ 2.5 to 2.9.

Figure 23. Concluded.

(a) Forward rake, X/L = 0.684.

Figure 24. Comparison of boundary layer profiles and thicknesses as Mach number is varied. α ≈ 3°; BTL ≈ 12.3° to 18.4°; BTR ≈ 9.7° to 19.6°; and NPRL ≈ 2.0 to 5.0.

(b) Aft rake, X/L = 0.867.

Figure 24. Concluded.

(a) Forward rake, X/L = 0.684.

Figure 25. Comparison of boundary layer profiles and thicknesses as angle of attack is varied. $M_\infty \approx 0.8°$; BTL $\approx 18.4°$ to 17.9°; BTR $\approx 18.4°$ to 19.6°; and NPRL ≈ 2.0 to 4.4.

Legend:
- ○ Flight
- □ Model, scaled
- --- 1/9-power profile, flight
- ▬ Boundary layer thickness, flight
- ▨ Approximate thickness, model, scaled
- —— Fairing
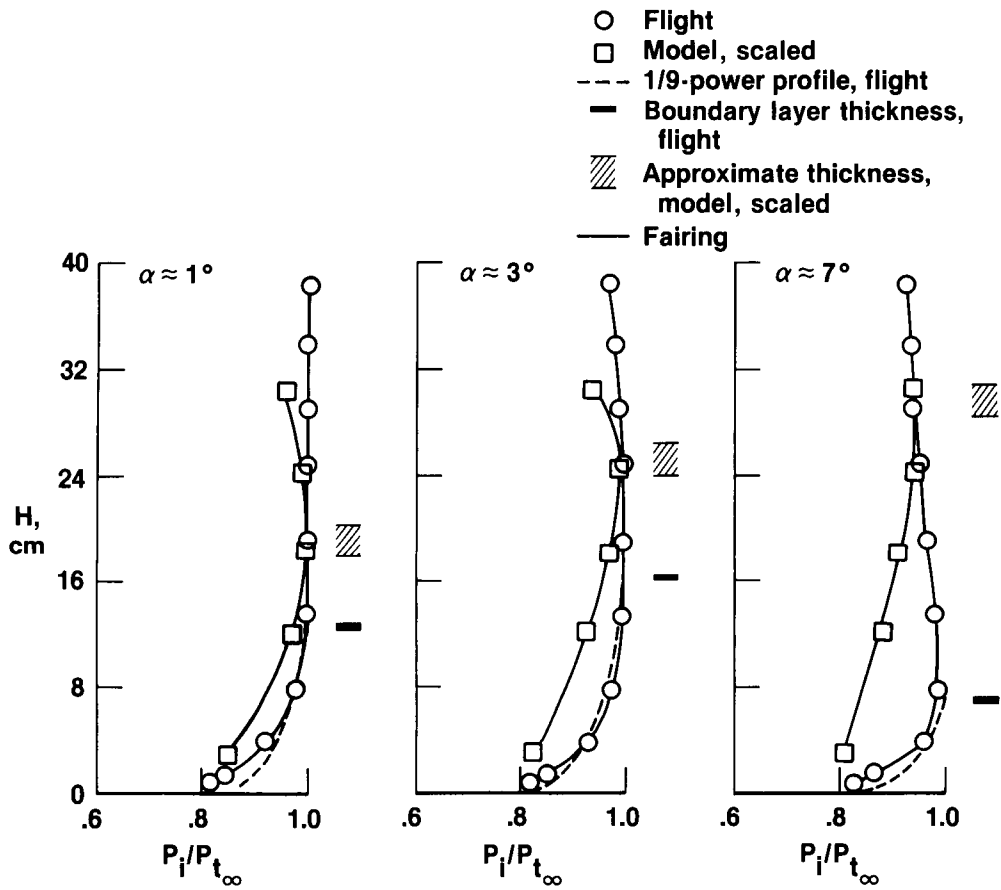
(b) Aft rake, X/L = 0.867.

Figure 25. Concluded.
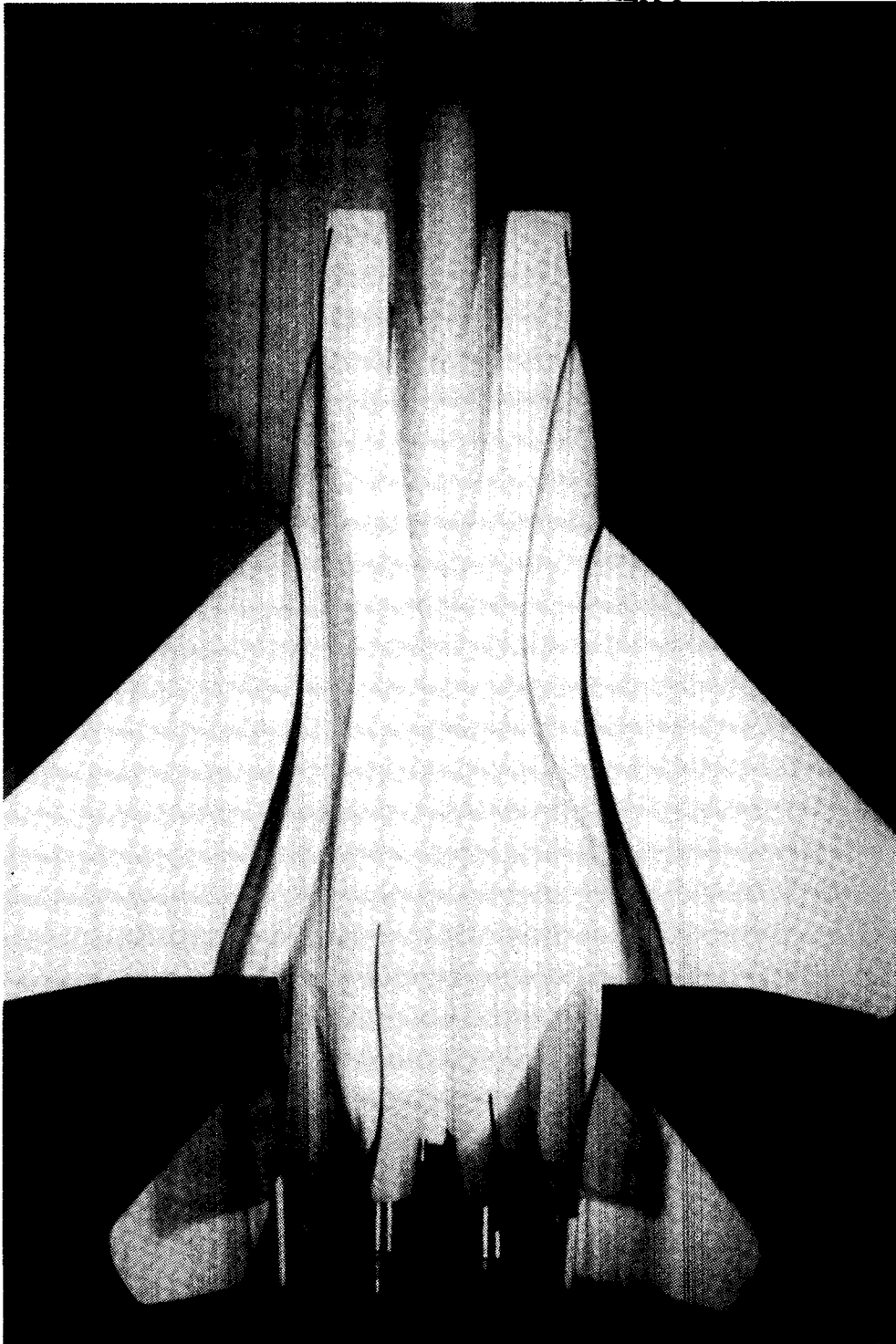
ECN 25684

(a) Plan view at $\alpha = 1°$.

Figure 26. Effect of angle of attack on flow patterns of
flowing-inlet configuration.
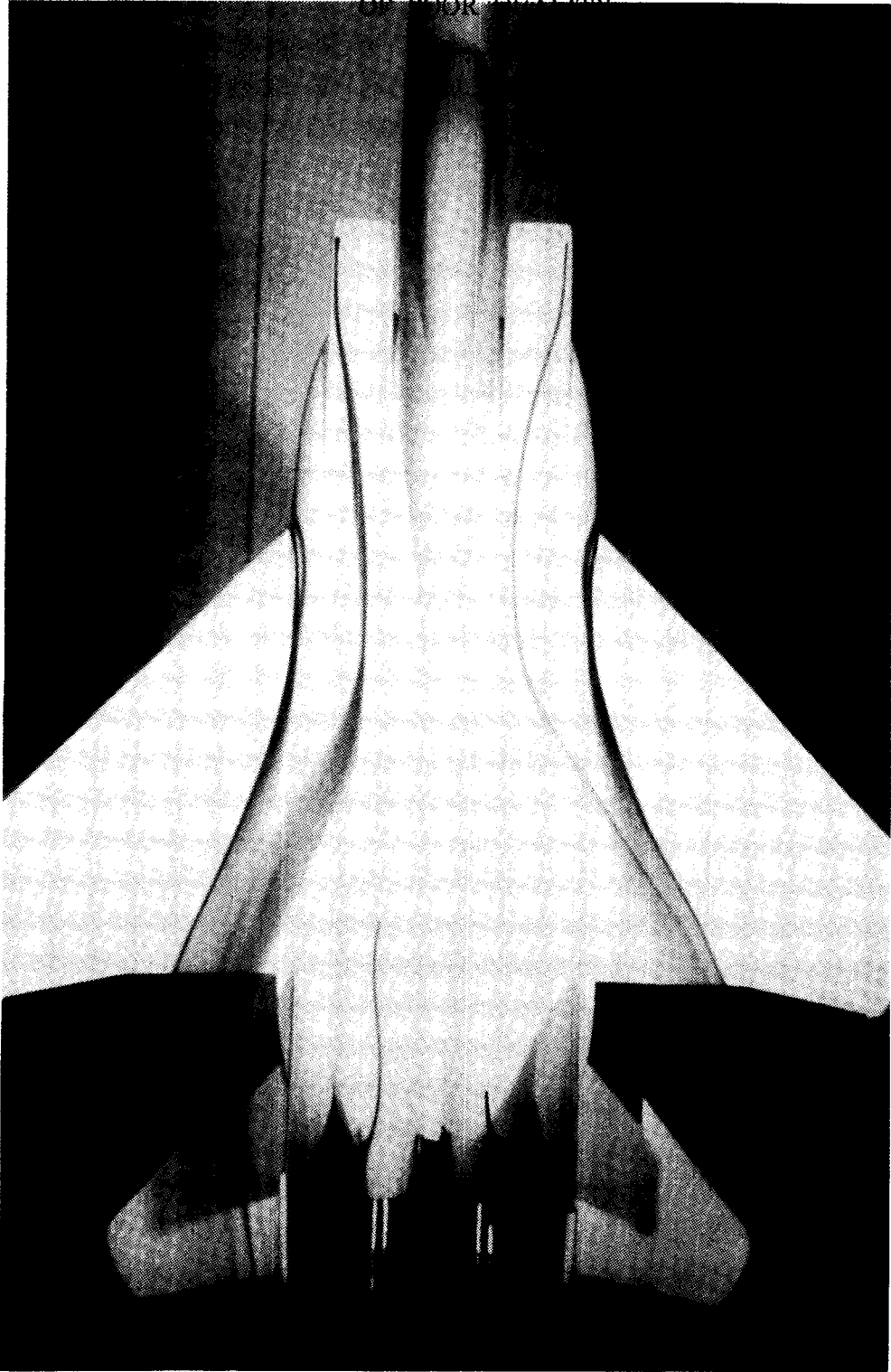
ECN 25686

(b) Plan view at α = 3°.

Figure 26. Continued.
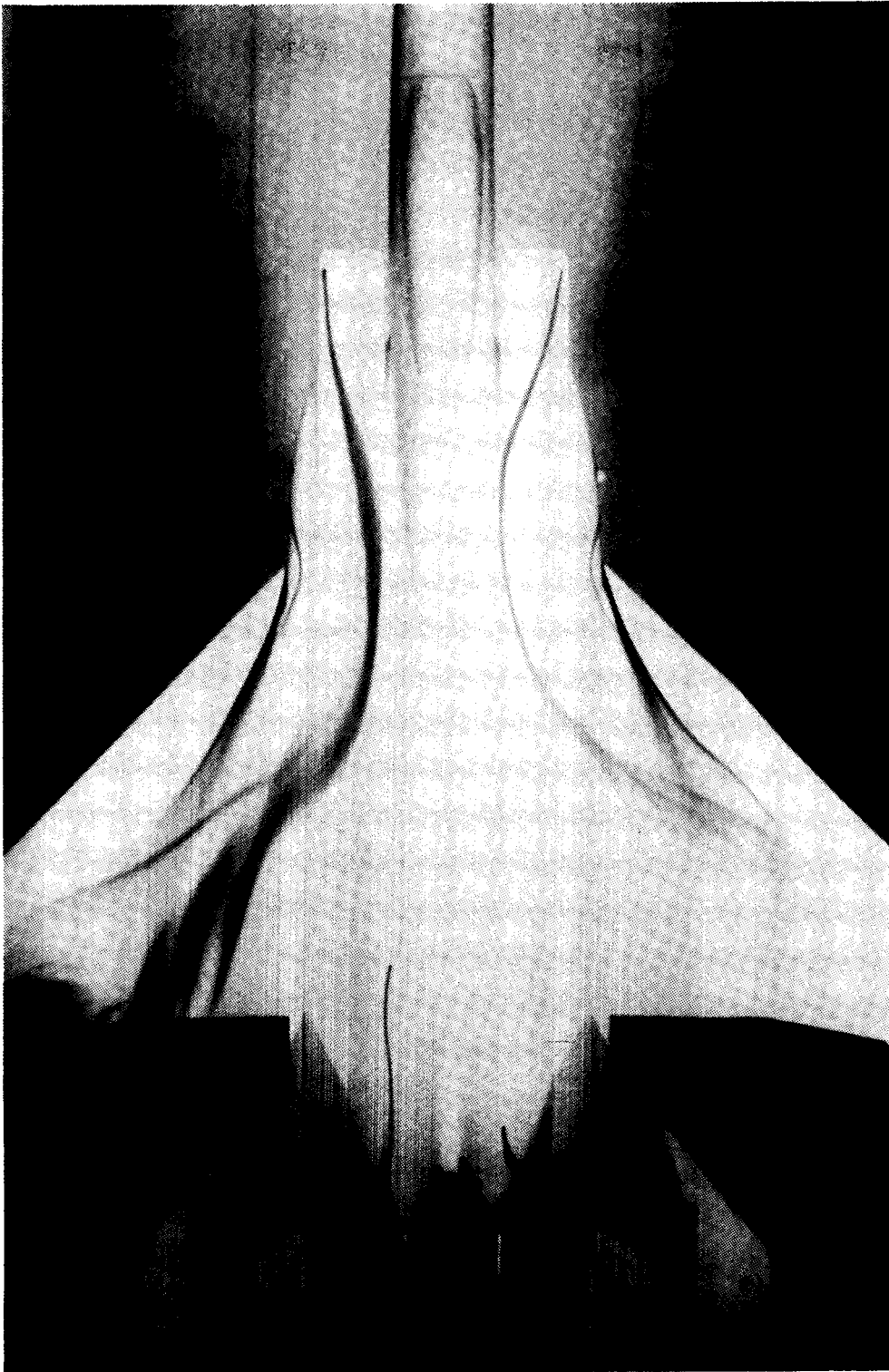
ECN 25687

(c) Plan view at α = 7°.

Figure 26. Continued.
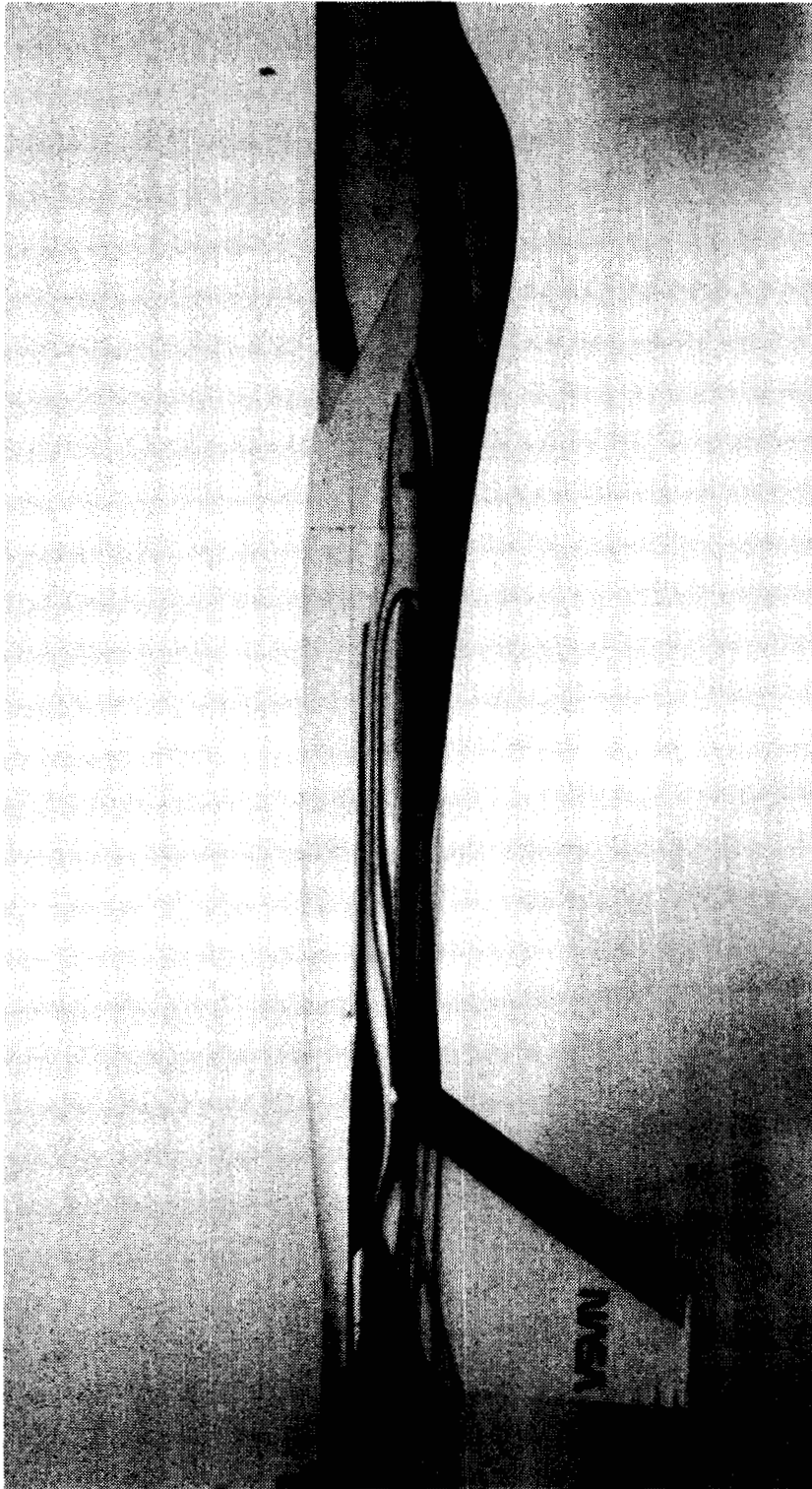
ECN 25693

(d) Side view at α = 1°.

Figure 26. Continued.
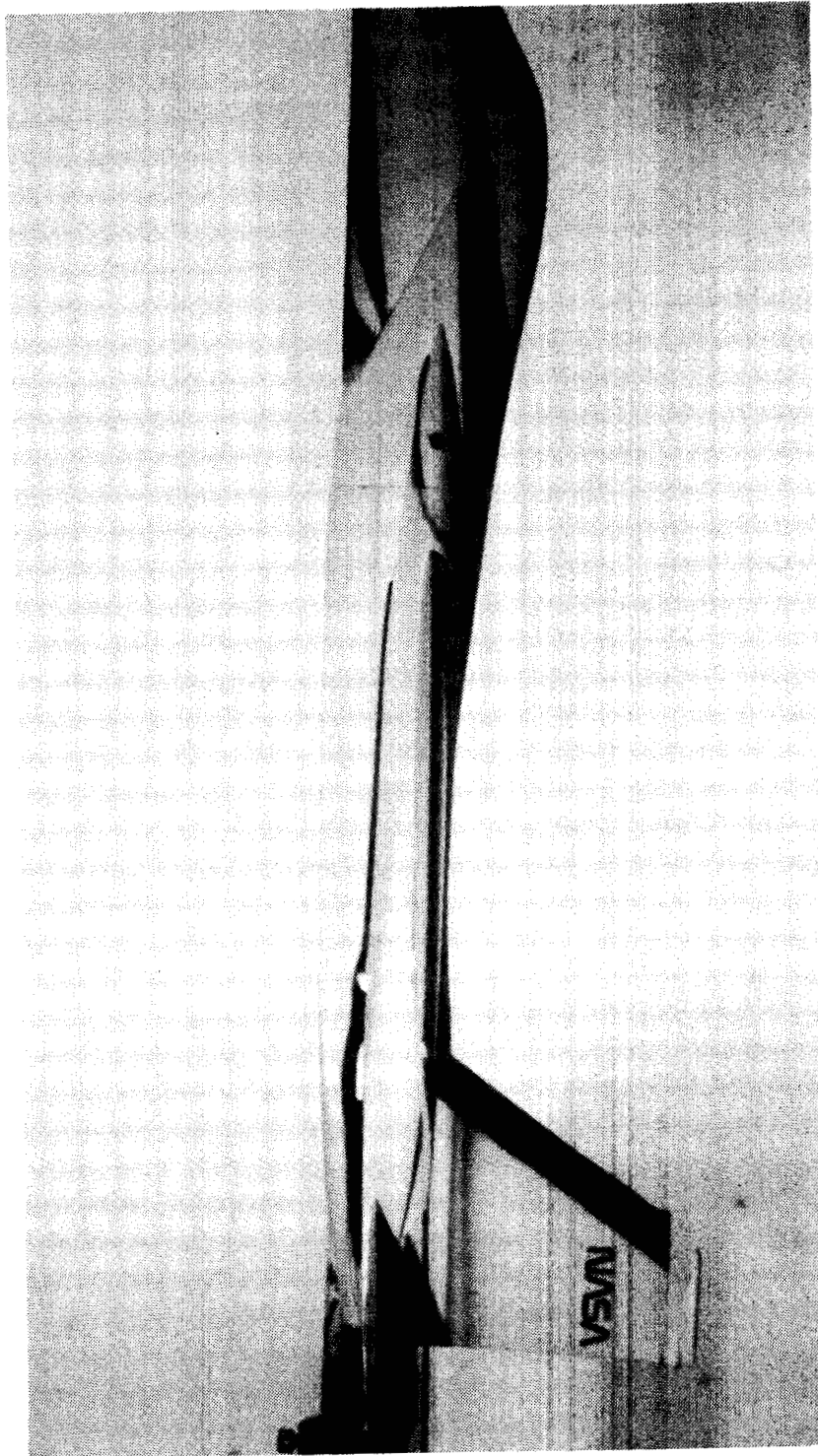
ECN 25694

(e) *Side view at α = 3°.*

Figure 26. Continued.
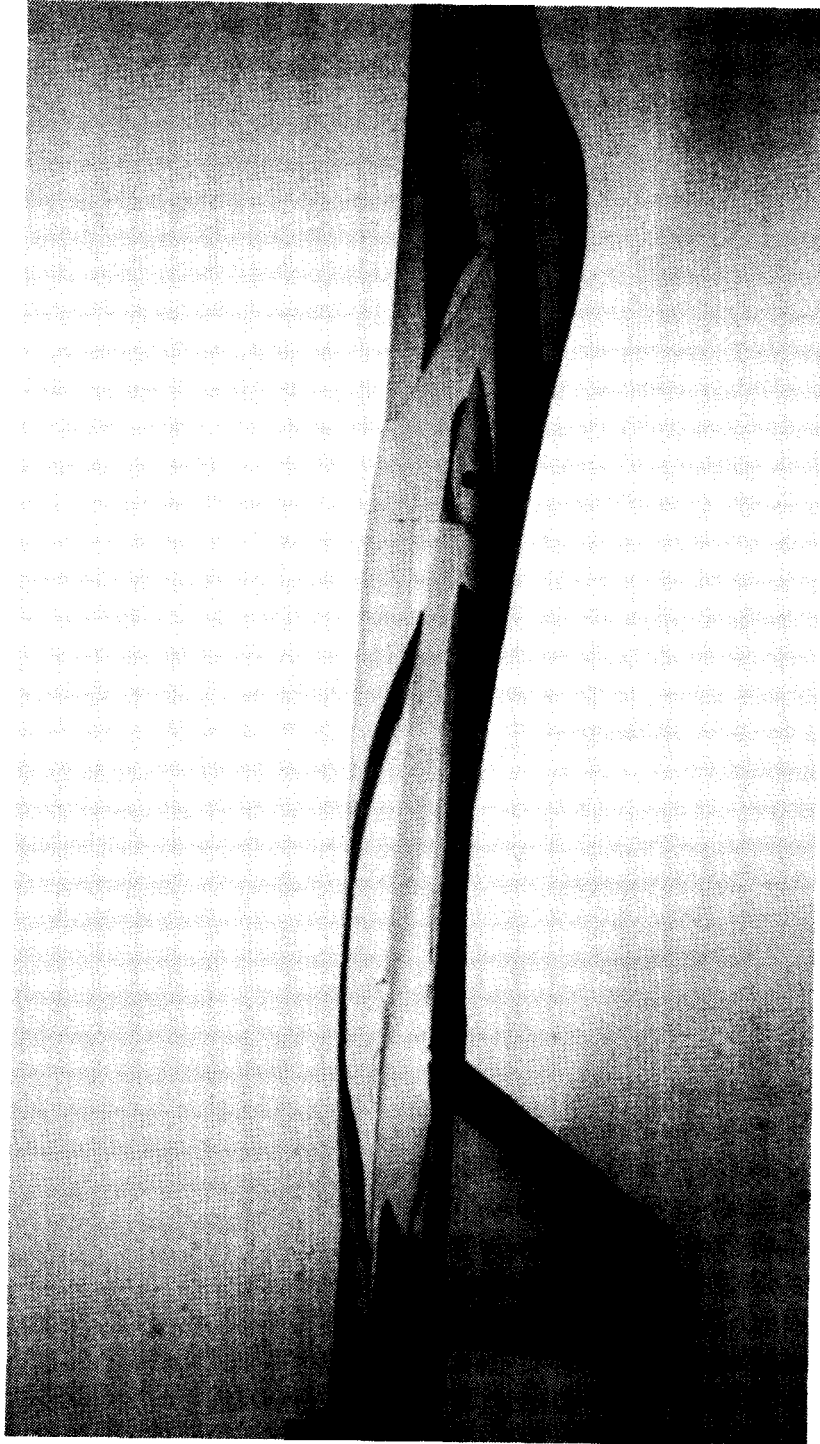
ECN 25696

(f) Side view at α = 7°.

Figure 26. Concluded.
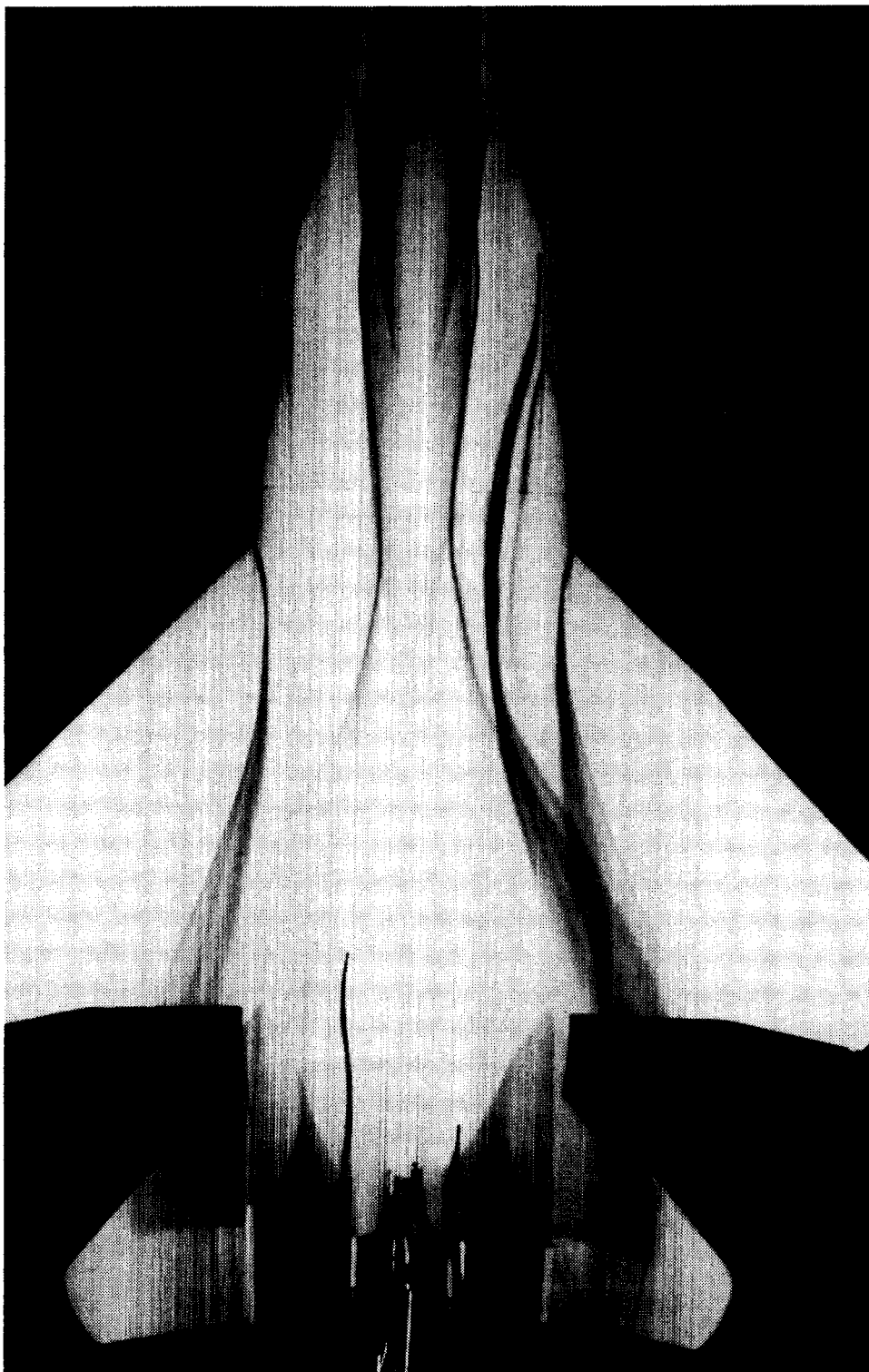
ECN 25688

(a)   Plan view at α = 1°.

Figure 27.   Effect of angle of attack on flow patterns of faired-inlet configuration.
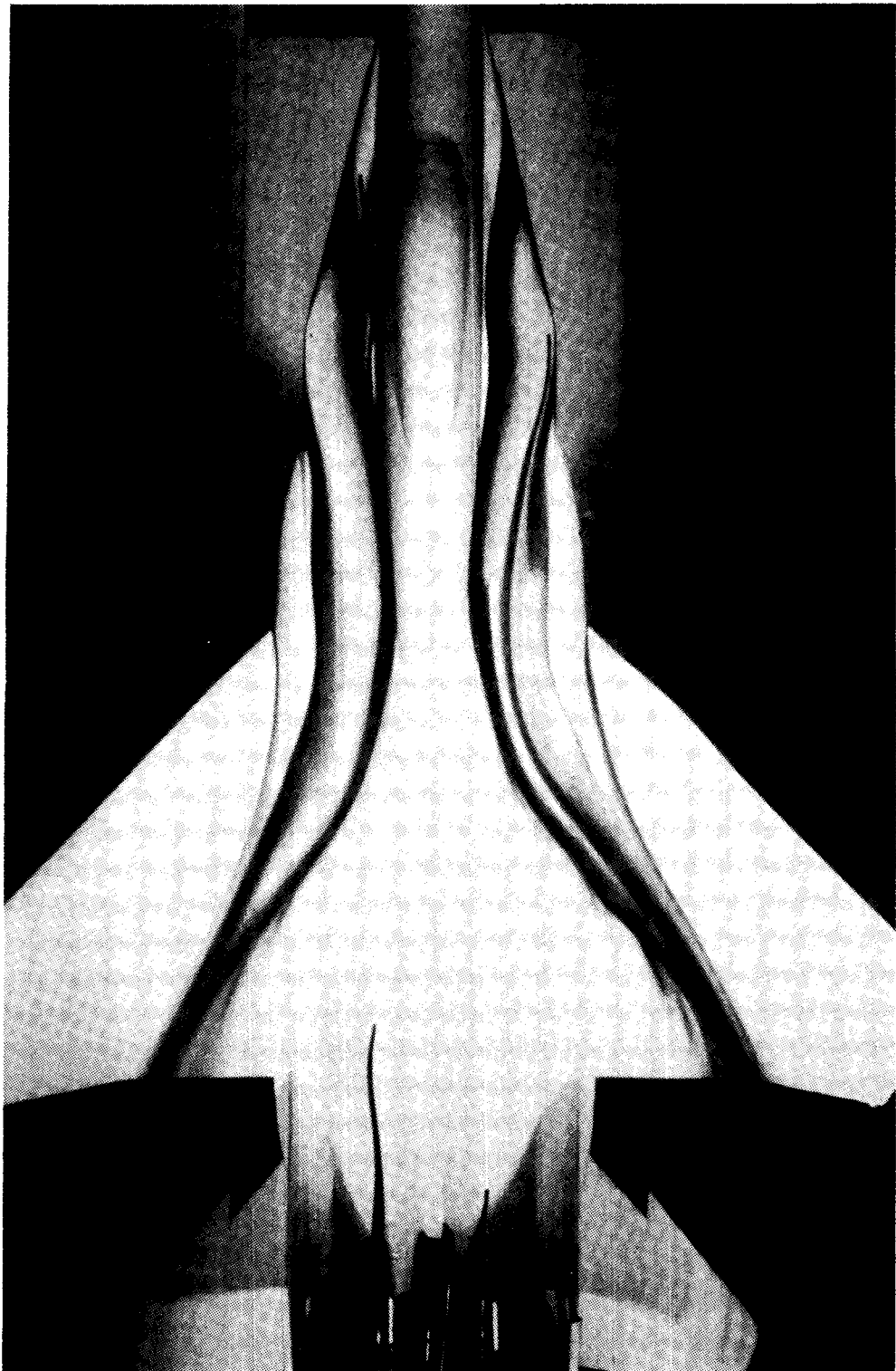
ECN 25689

(b) Plan view at α = 3°.
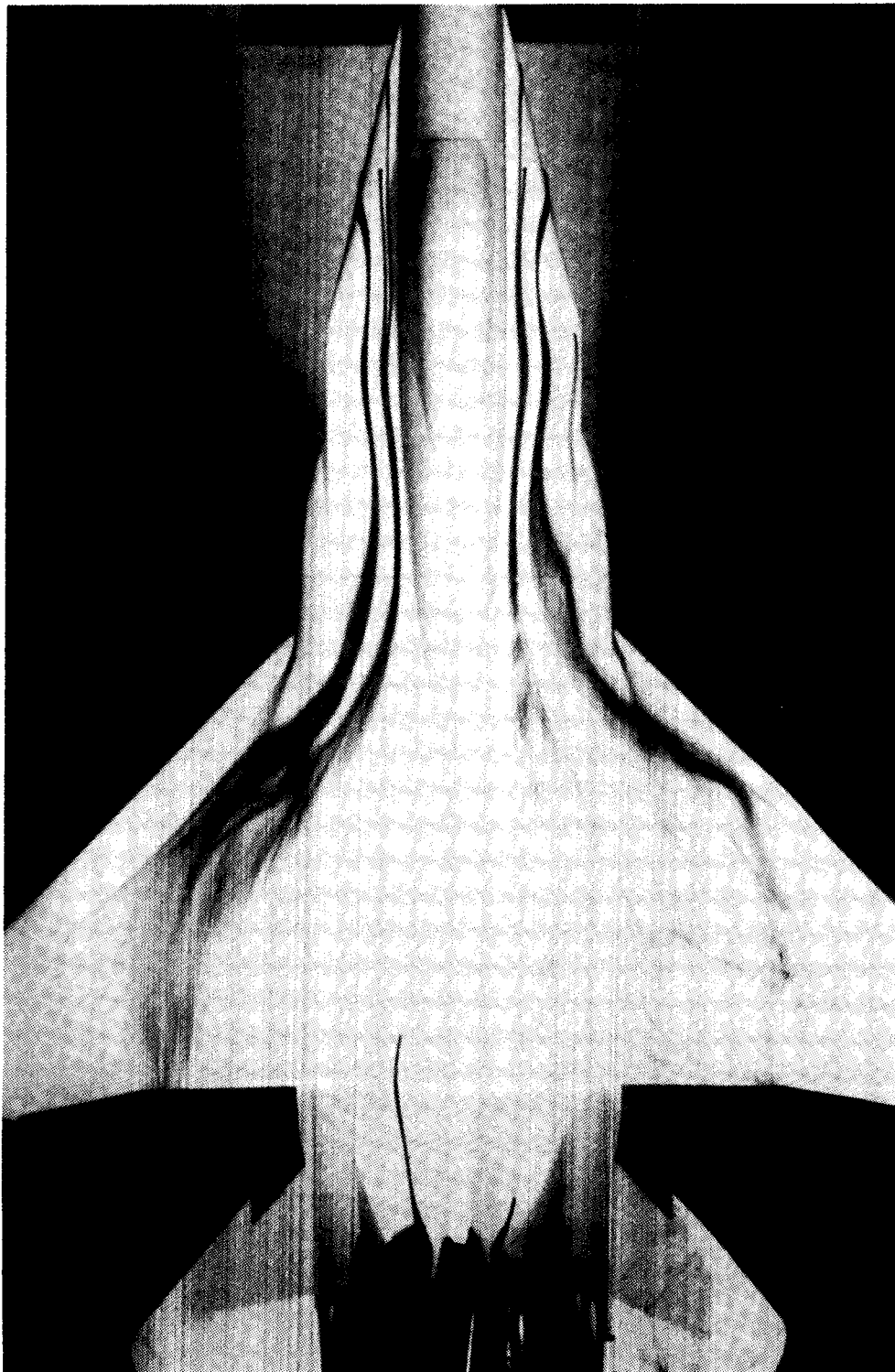
Figure 27. Continued.

ECN 25683

(c) Plan view at α = 7°.

Figure 27. Continued.
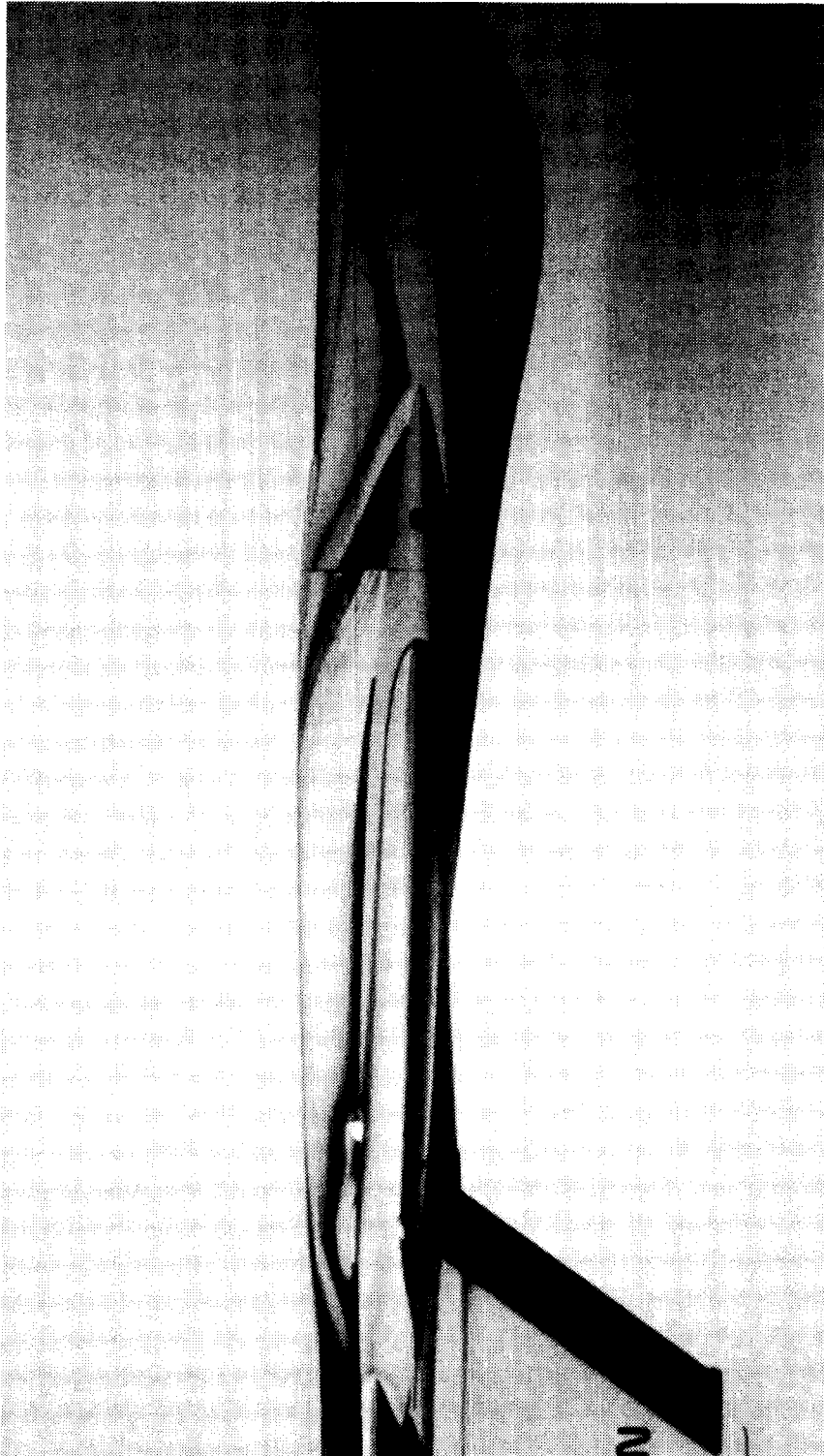
ECN 25697

(d)   Side view at α = 1°.

Figure 27.   Continued.
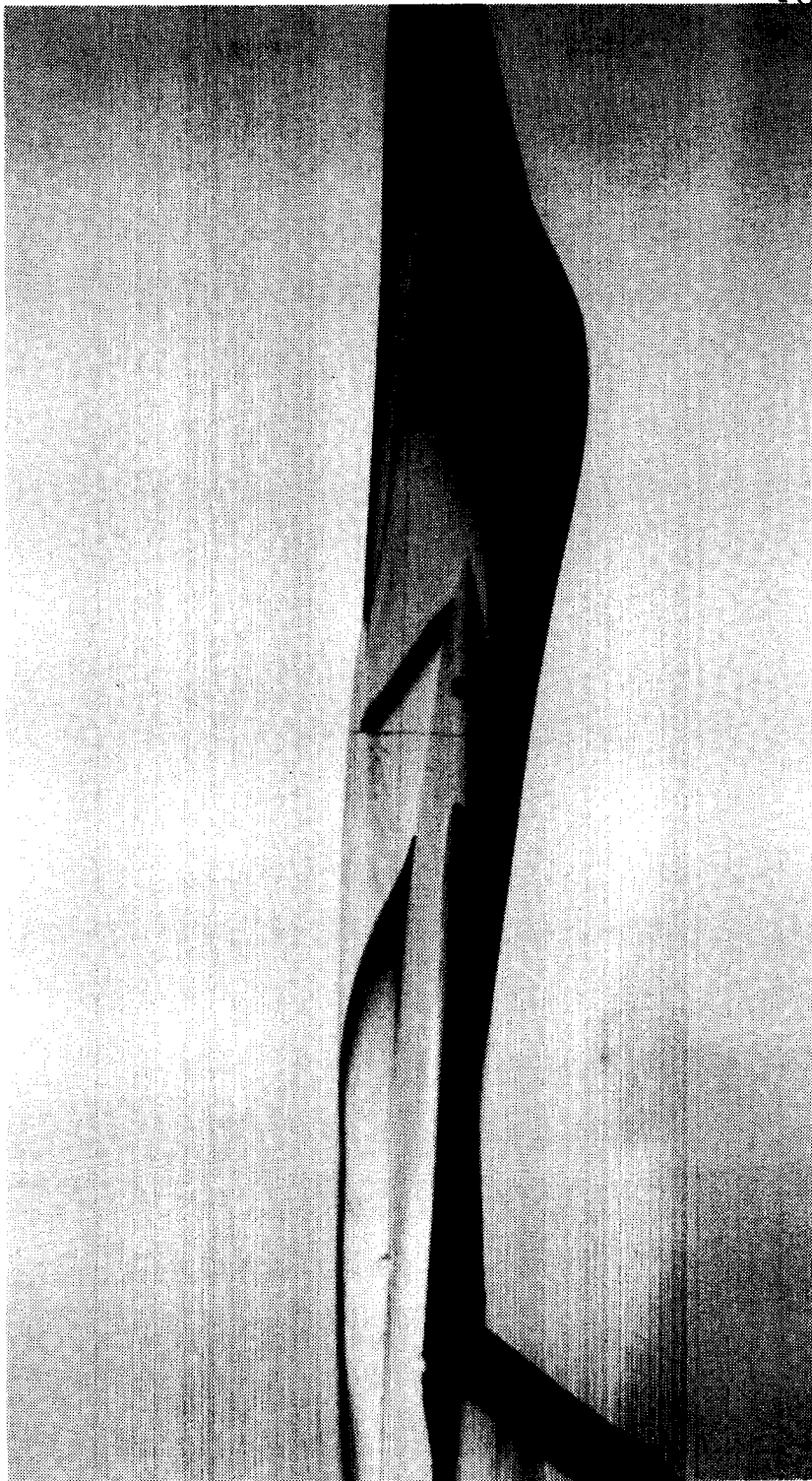
ECN 25698

(e) *Side view at* α = 3°.

Figure 27. Continued.
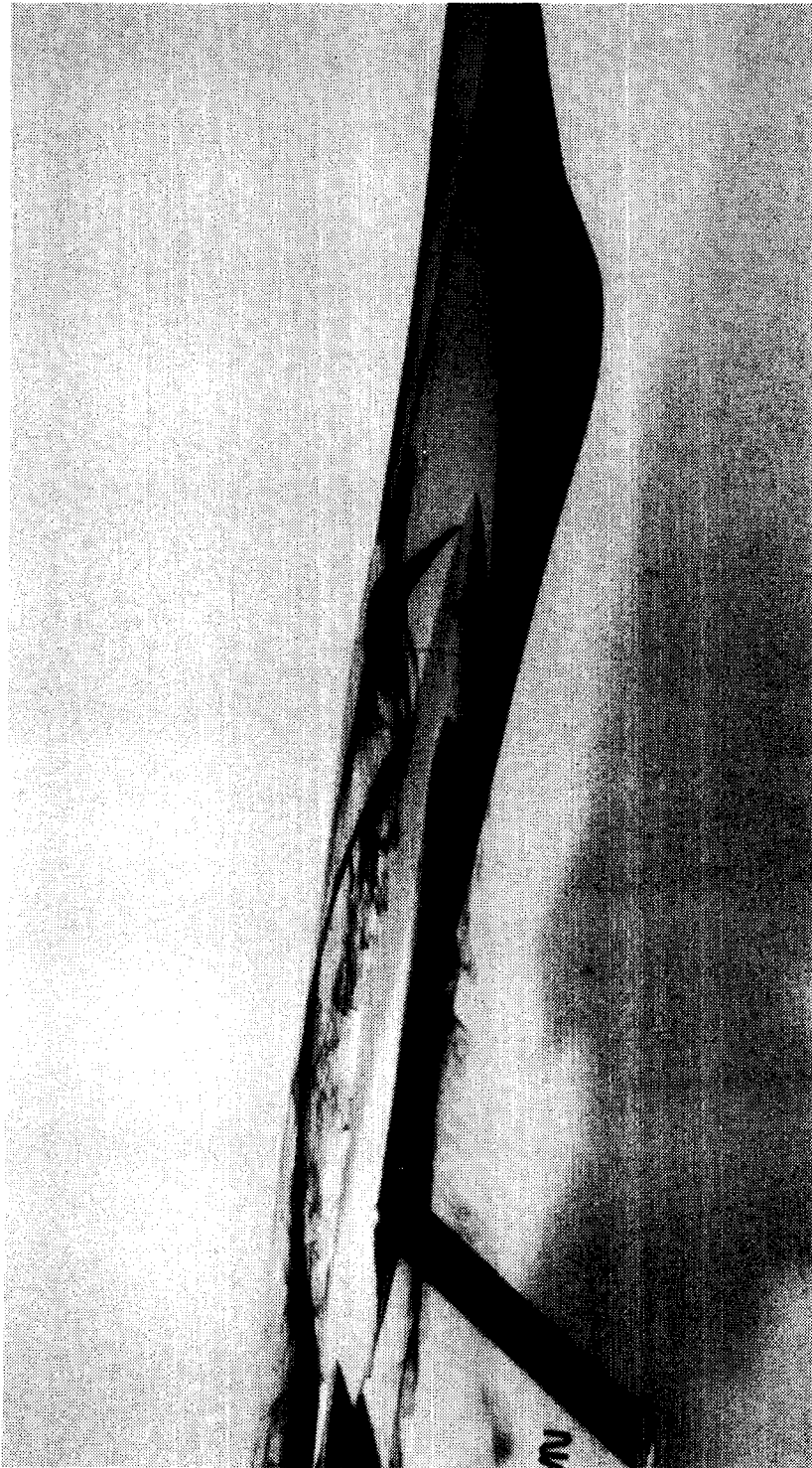
ECN 25692

(f) Side view at α = 7°.

Figure 27. Concluded.
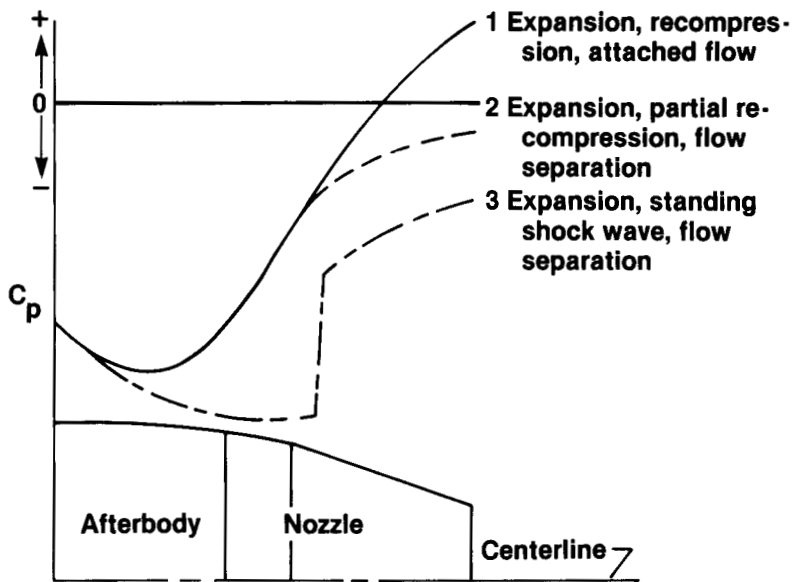
Figure 28. Variations in pressure coefficient associated with afterbody and nozzle flow interactions.
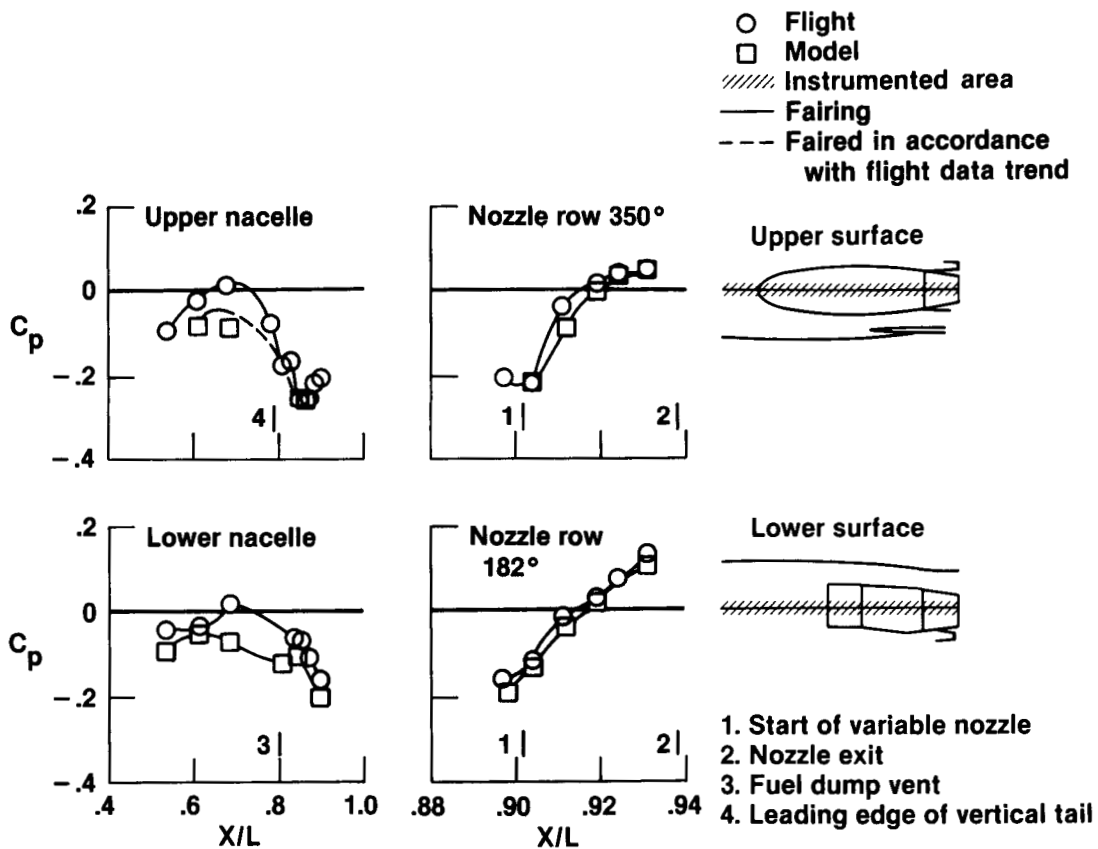
(a) $M_{\infty} \approx 0.6$; BTL $\approx 18.4°$; BTR $\approx 18.4°$; and NPRL ≈ 2.0 to 3.0.

Figure 29. Comparison of afterbody and nozzle pressure coefficient distributions as Mach number is varied at $\alpha \approx 1°$.

O Flight
□ Model
/////// Instrumented area
—— Fairing
– – – Faired in accordance
       with flight data trend

Upper nacelle

Nozzle row 350°

Upper surface

Lower nacelle

Nozzle row 182°

Lower surface

1. Start of variable nozzle
2. Nozzle exit
3. Fuel dump vent
4. Leading edge of vertical tail

(b) $M_\infty \approx 0.8$; BTL $\approx 18.4°$; BTR $\approx 18.4°$ to $19.5°$; and NPRL ≈ 2.0
to 3.0.

Figure 29. Continued.

Legend:
- O Flight
- □ Model
- ///// Instrumented area
- —— Fairing
- --- Faired in accordance with flight data trend

Upper nacelle / Nozzle row 350° / Upper surface

Lower nacelle / Nozzle row 182° / Lower surface

1. Start of variable nozzle
2. Nozzle exit
3. Fuel dump vent
4. Leading edge of vertical tail

(c) $M_\infty \approx 0.9$; $BTL \approx 18.4°$; $BTR \approx 18.4°$ to $19.7°$; and $NPRL \approx 2.0$ to 3.0.

Figure 29. Continued.

O   Flight
□   Model
////// Instrumented area
——— Fairing
— — — Faired in accordance
        with flight data trend

(d) $M_\infty \approx 1.2$; BTL $\approx 7.7°$; BTR $\approx 7.7°$; and NPRL ≈ 5.0.

Figure 29. Concluded.

(a) $\alpha \approx 1°$; BTL $\approx 18.4°$; BTR $\approx 18.4°$ to $19.5°$; and NPRL ≈ 3.0.

Figure 30. Comparison of afterbody and nozzle pressure coefficient distributions as angle of attack is varied at $M_\infty \approx 0.8$.

Legend:

○ Flight
□ Model
░░░ Instrumented area
—— Fairing
– – – Faired in accordance with flight data trend

Upper nacelle

Nozzle row 350°

Upper surface

Lower nacelle

Nozzle row 182°

Lower surface

1. Start of variable nozzle
2. Nozzle exit
3. Fuel dump vent
4. Leading edge of vertical tail

(b) $\alpha \approx 3°$; $BTL \approx 18.4°$; $BTR \approx 18.4°$ to $16.0°$; and $NPRL \approx 2.5$.

Figure 30. Continued.

Legend:
- ○ Flight
- □ Model
- ▨ Instrumented area
- ── Fairing

Upper nacelle

Nozzle row 350°

Upper surface

Lower nacelle

Nozzle row 182°

Lower surface

1. Start of variable nozzle
2. Nozzle exit
3. Fuel dump vent
4. Leading edge of vertical tail

(c) $\alpha \approx 5°$; *BTL* $\approx 18.4°$; *BTR* $\approx 18.4°$ *to* $19.2°$; *and NPRL* ≈ 2.5 *to* 3.7.

Figure 30.   Continued.
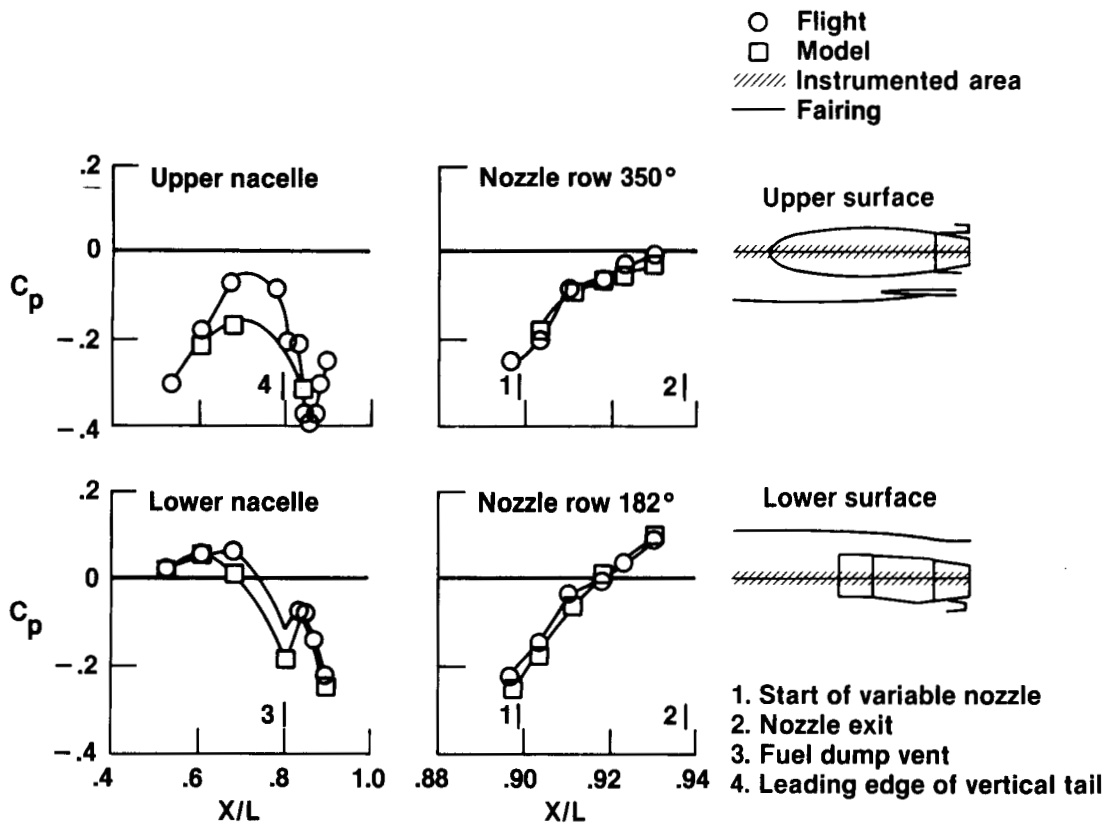
(d) $\alpha \approx 6°$ to $7°$; $BTL \approx 18.4°$; $BTR \approx 18.4°$; and $NPRL \approx 3.0$ to 3.5.

Figure 30. Concluded.

Figure 31. Comparison of afterbody and nozzle pressure coefficient distributions as left nozzle boattail angle is varied at $\alpha \approx 1°$ to $2°$.

(a) $M_\infty \approx 0.6$; $BTL \approx 15.1°$; $BTR \approx 18.4°$ to $19.5°$; and $NPRL \approx 4.0$.

Figure legend:
- ○ Flight
- □ Model
- ░░ Instrumented area
- —— Fairing
- – – – Faired in accordance with flight data trend

Graphs: Upper nacelle, Nozzle row 350°, Upper surface, Lower nacelle, Nozzle row 182°, Lower surface

1. Start of variable nozzle
2. Nozzle exit
3. Fuel dump vent
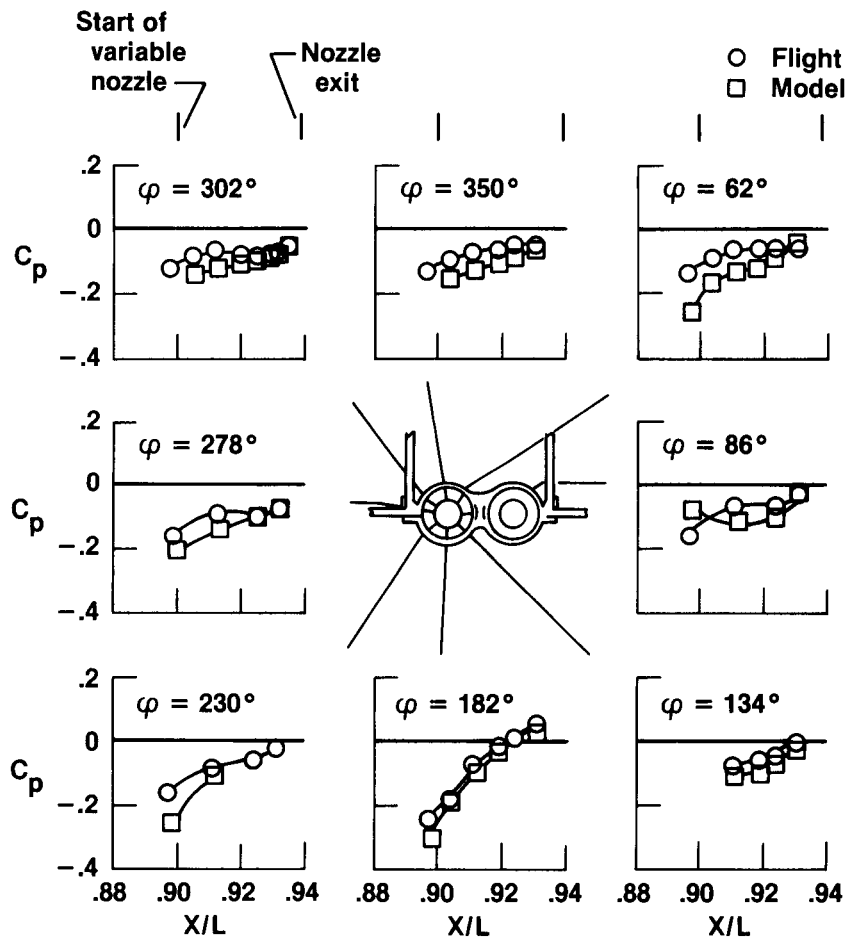4. Leading edge of vertical tail
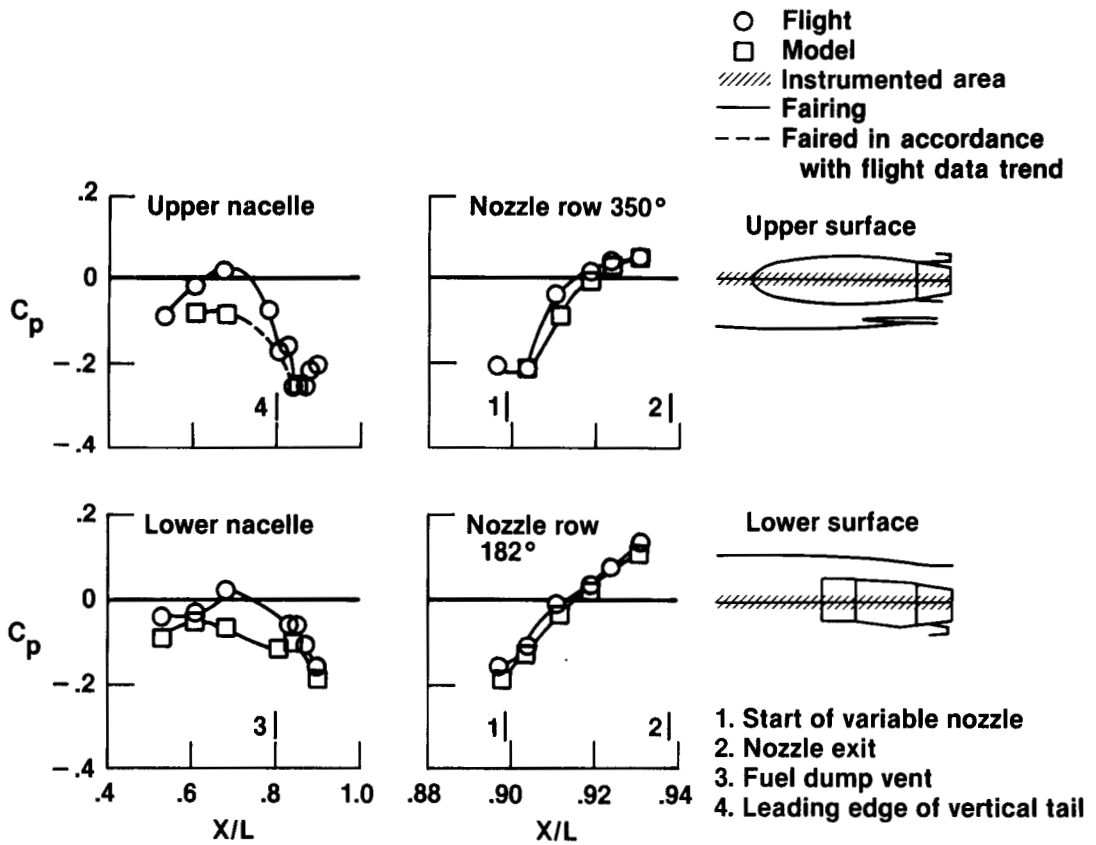
(b) $M_\infty \approx 0.6$; $BTL \approx 18.4°$; $BTR \approx 18.4°$ to $19.5°$; and $NPRL \approx 3.0$.

Figure 31. Continued.

$C - 2$
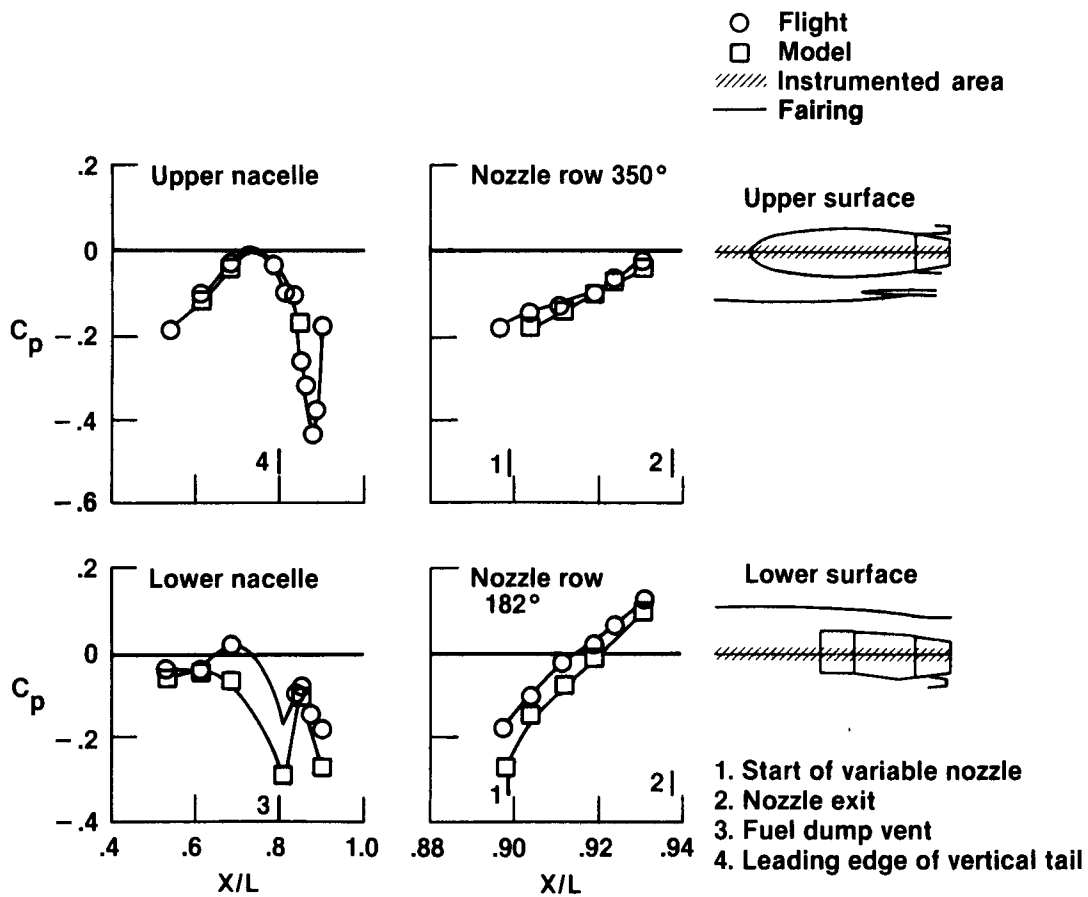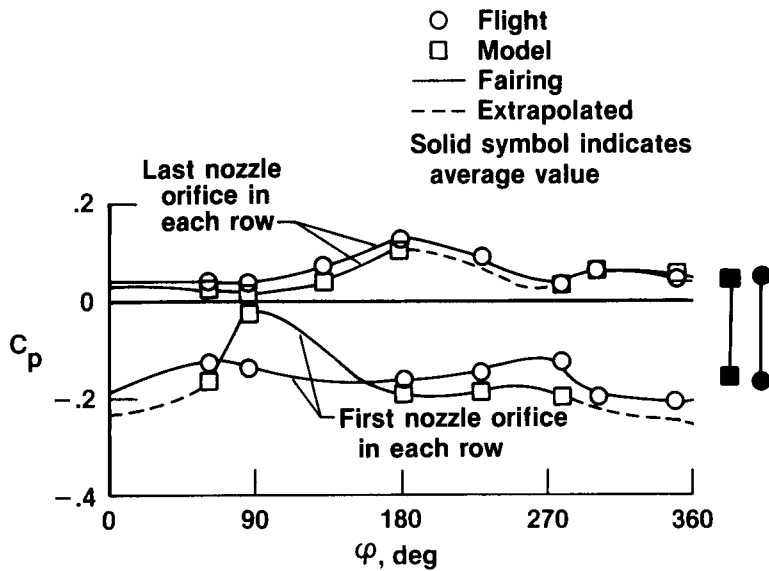
(c) $M_\infty \approx 0.9$; $BTL \approx 15.1°$; $BTR \approx 18.4°$ to $19.5°$; and $NPRL \approx 5.0$.
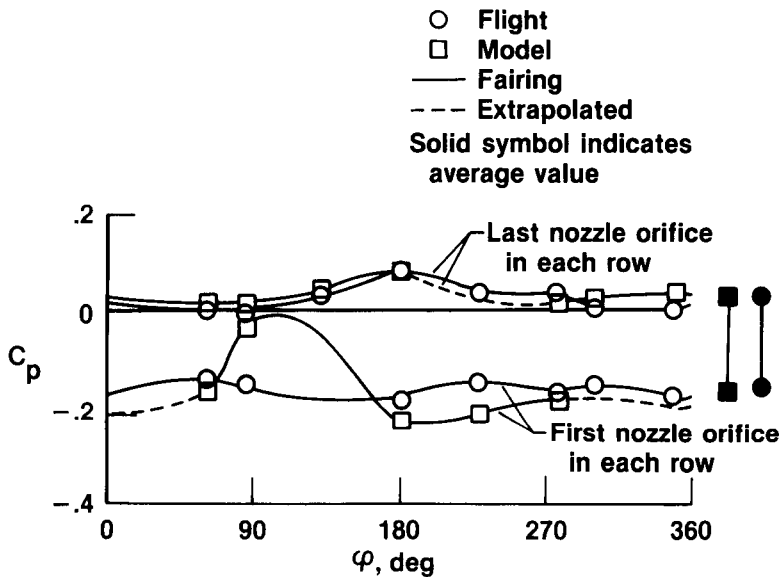
Figure 31. Continued.
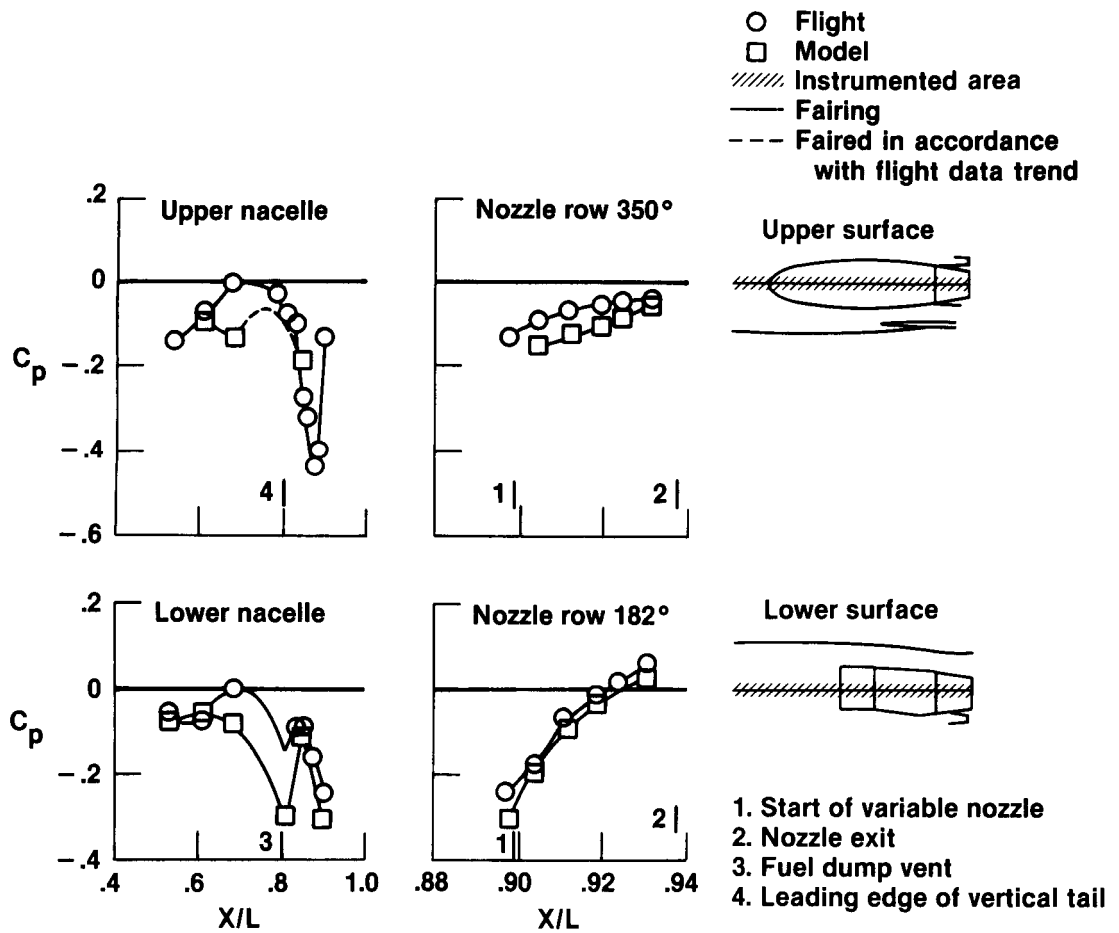
(d) $M_\infty \approx 0.9$; BTL $\approx 18.4°$; BTR $\approx 18.4°$ to $15.4°$; and NPRL ≈ 2.5 to 2.9.
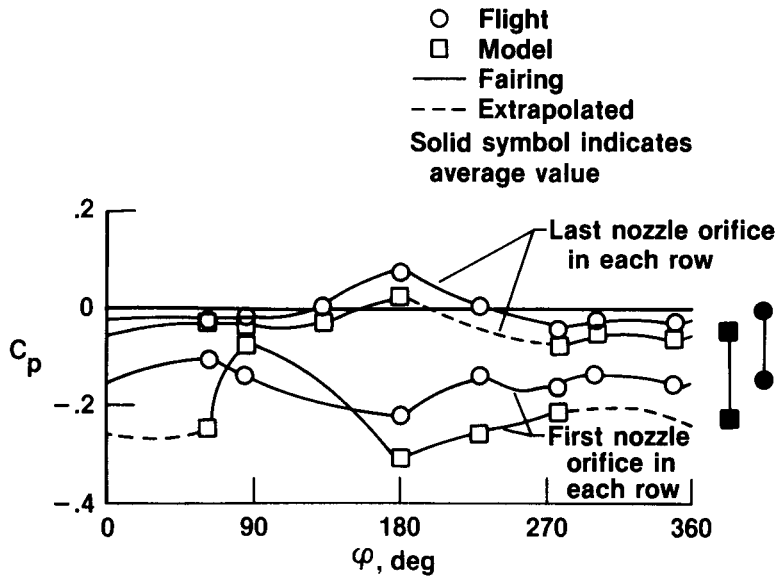
Figure 31. Concluded.
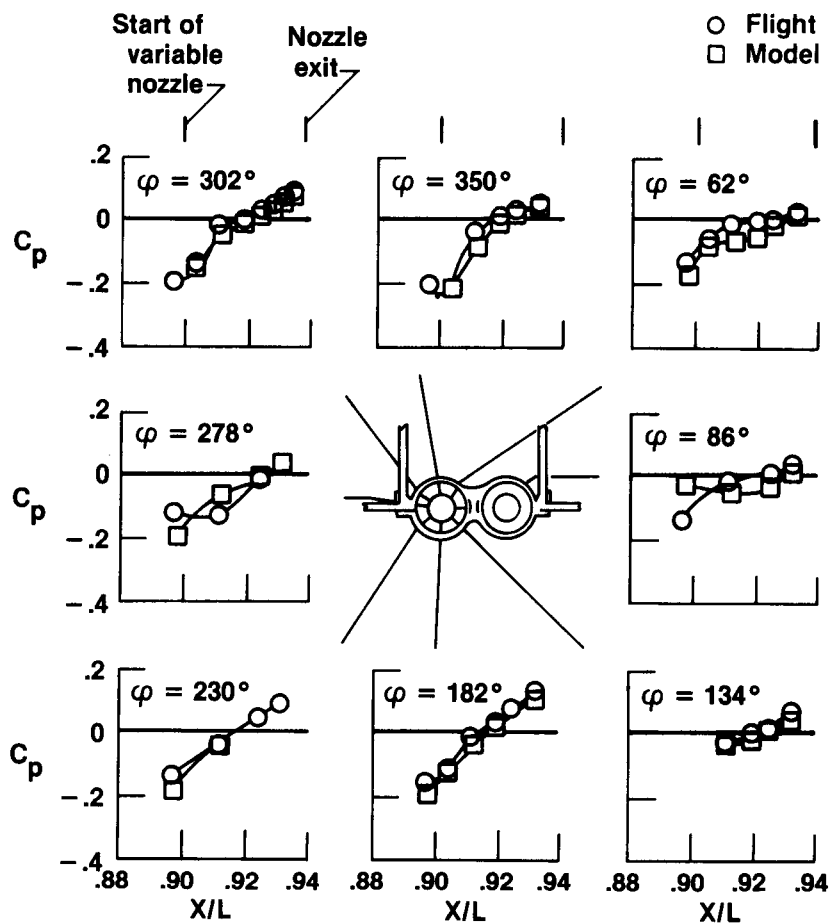
(a) $M_\infty \approx 0.6$; BTL $\approx 18.4°$; BTR $\approx 18.4°$; and
NPRL ≈ 3.0.

Figure 32. Comparison of nozzle pressure coefficient distributions as Mach number is varied at α ≈ 1°.
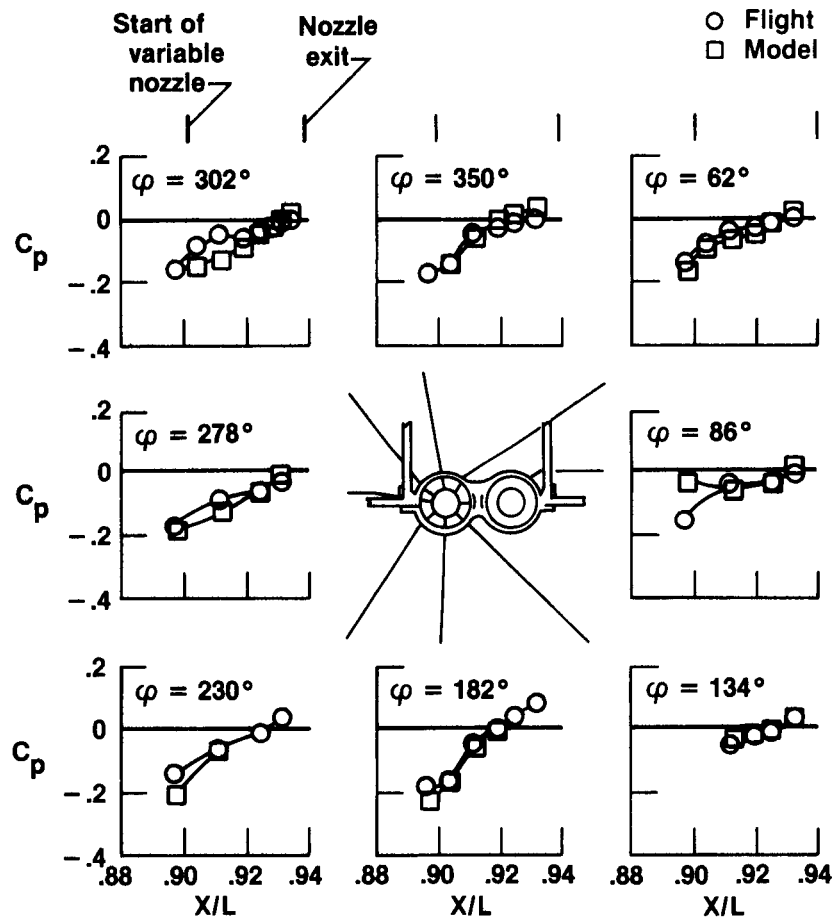
(b) $M_\infty \approx 0.8$; BTL $\approx 18.4°$; BTR $\approx 18.4°$ to $19.5°$;
and NPRL ≈ 2.0 to 3.0.

Figure 32. Continued.
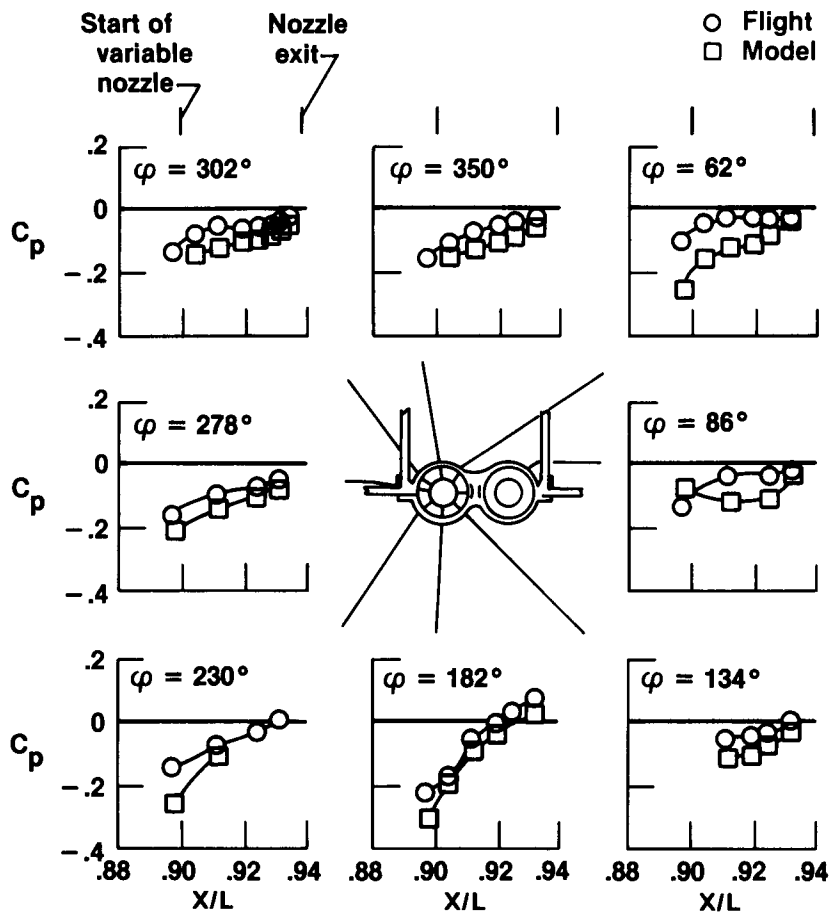
(c) $M_\infty \approx 0.9$; BTL $\approx 18.4°$; BTR $\approx 18.4°$ to $19.7°$; and NPRL ≈ 2.0 to 3.0.

Figure 32. Continued.
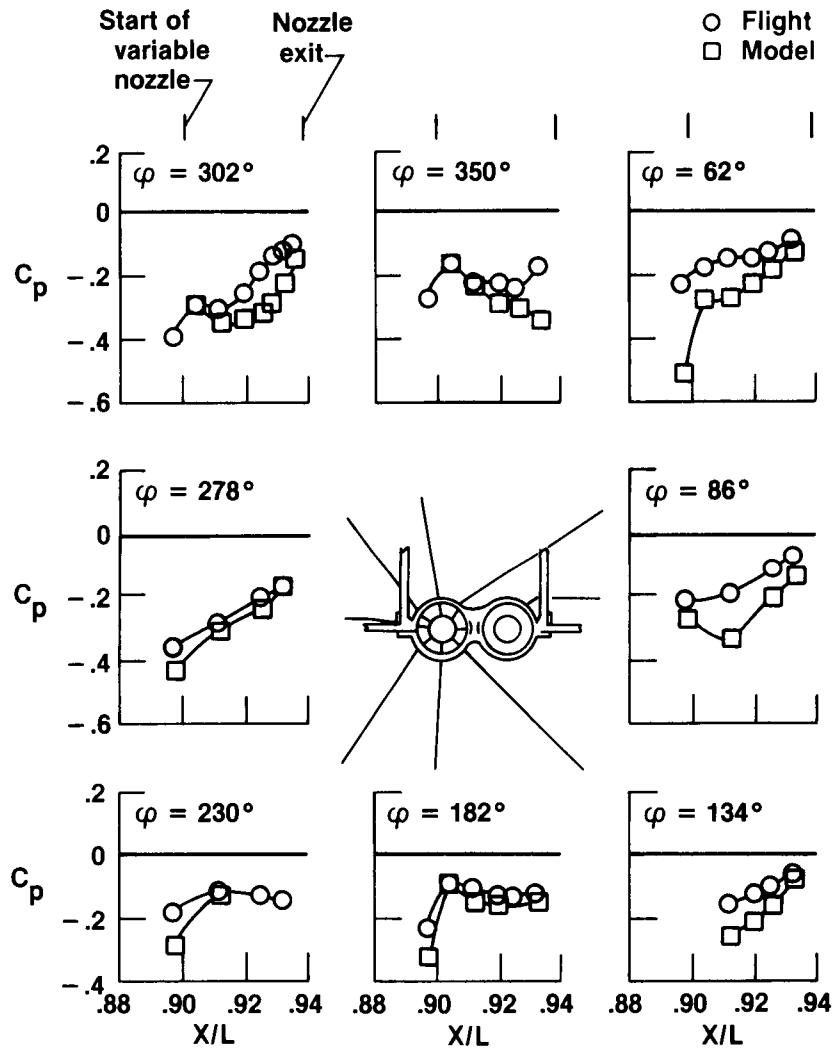
(d) $M_{\infty} \approx 1.2;\ BTL \approx 7.7°;\ BTR \approx 7.7°;\ and$
$NPRL \approx 5.0.$

Figure 32. Concluded.
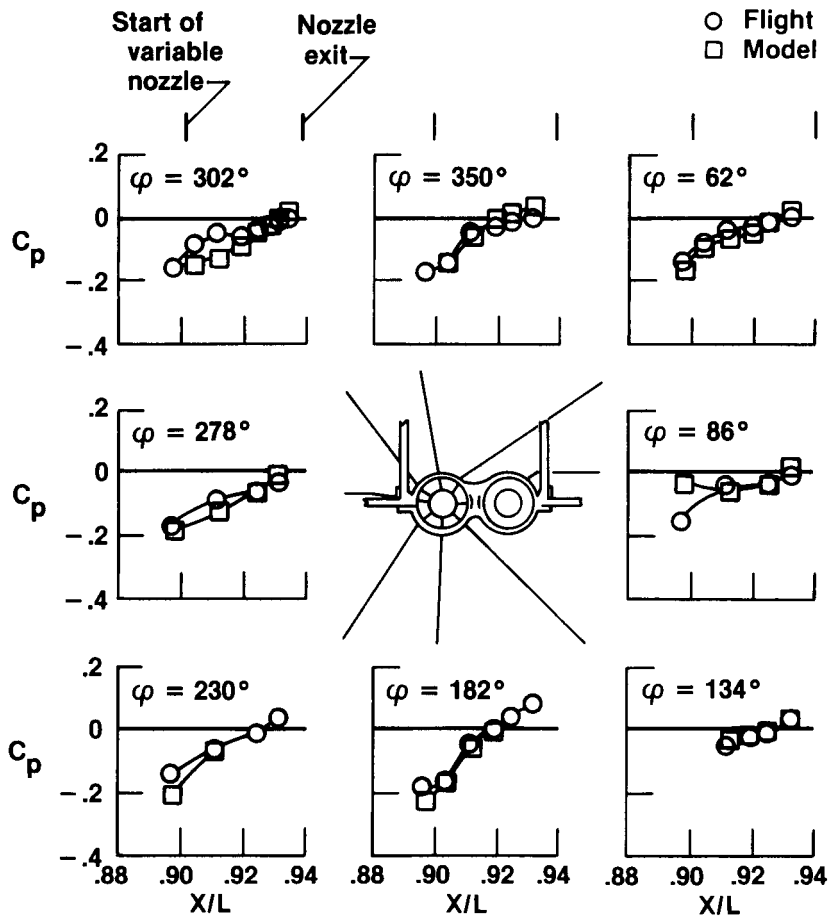
(a) α ≈ 1°; BTL ≈ 18.4°; BTR ≈ 18.4° to 19.5°; and
NPRL ≈ 3.0.

Figure 33. Comparison of nozzle pressure coefficient distributions as angle of attack is varied at M_∞ ≈ 0.8.
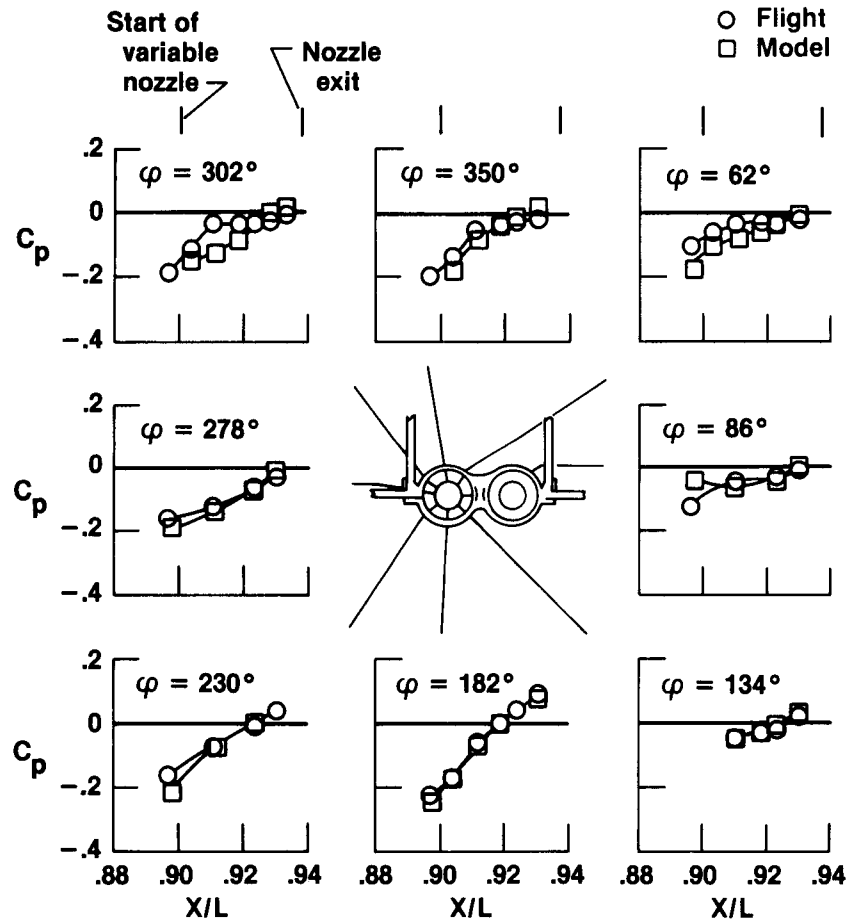
(b) α ≈ 3°; BTL ≈ 18.4°; BTR ≈ 18.4° to 16.0°; and
NPRL ≈ 2.5.

Figure 33.   Continued.
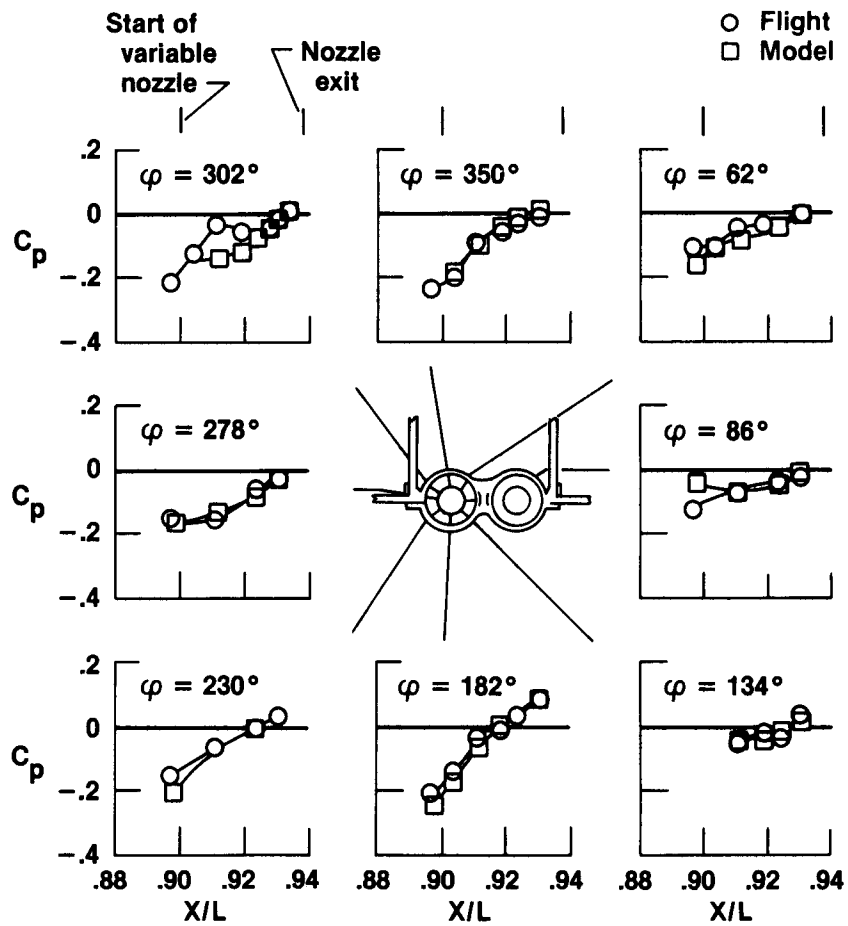
(c) α ≈ 5°; BTL ≈ 18.4°; BTR ≈ 18.4° to 19.2°; and NPRL ≈ 2.5 to 3.7.

Figure 33. Continued.
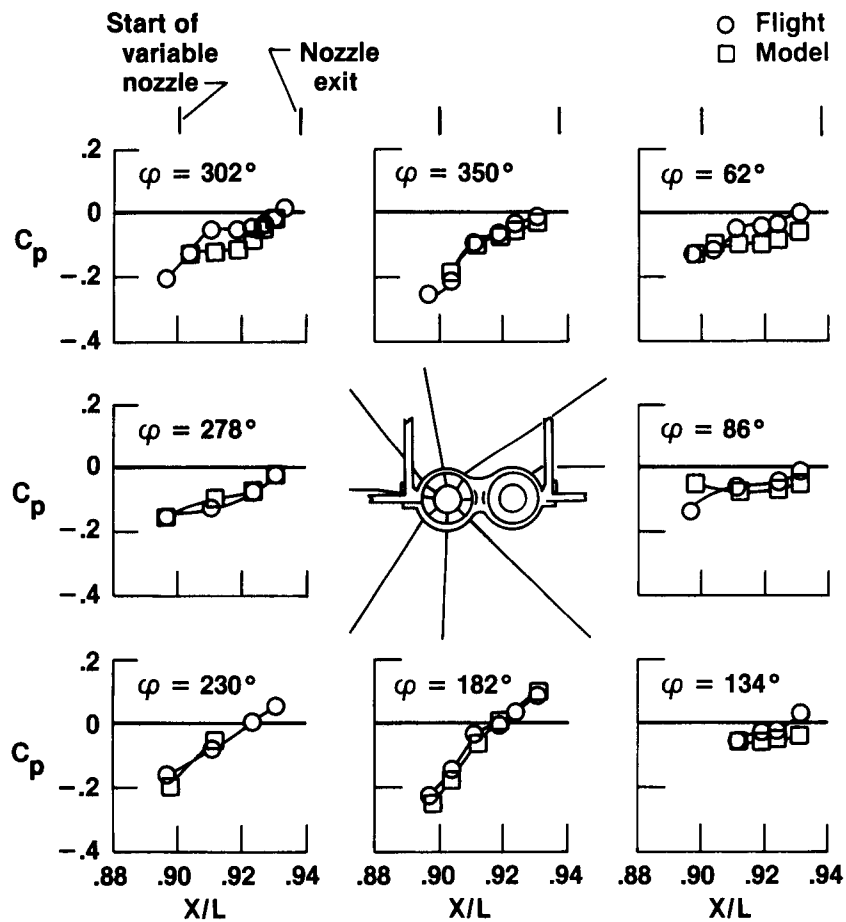
(d) $\alpha \approx 6°$ to $7°$; $BTL \approx 18.4°$; $BTR \approx 18.4°$; and $NPRL \approx 3.0$ to 3.5.

Figure 33. Concluded.
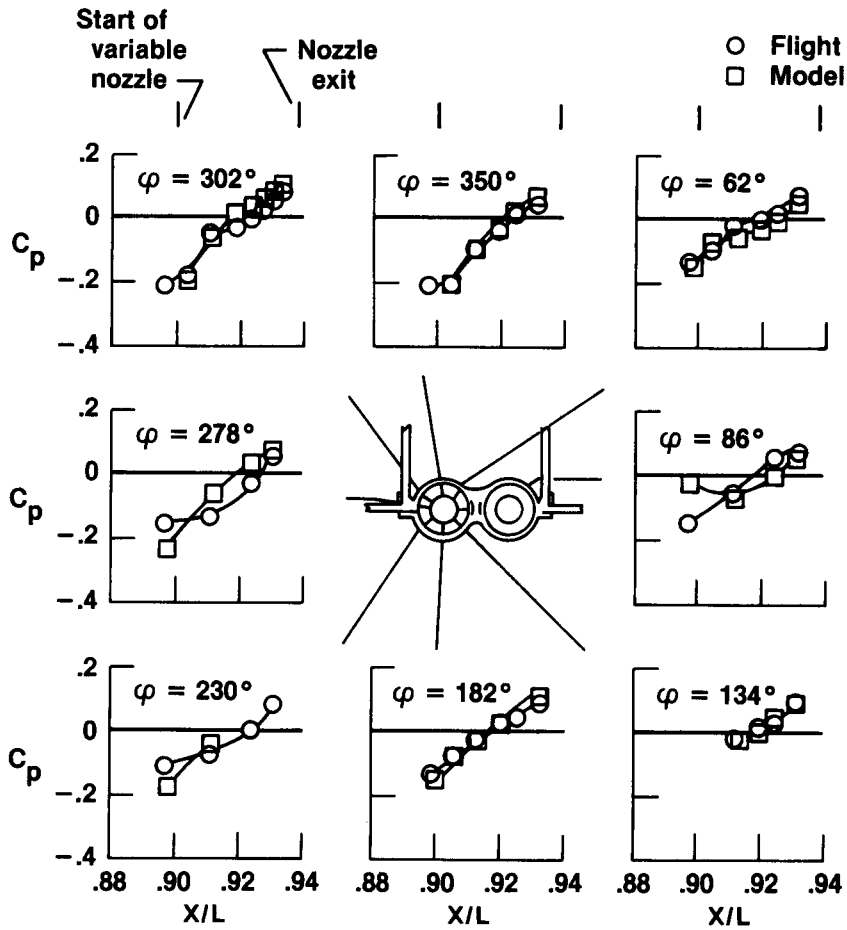
(a) $M_\infty \approx 0.6$; $BTL \approx 15.1°$; $BTR \approx 18.4$ to $19.5°$; and $NPRL \approx 4.0$.

Figure 34. Comparison of nozzle pressure coefficient distributions as the left nozzle boattail angle is varied at $\alpha \approx 1°$ to $2°$.
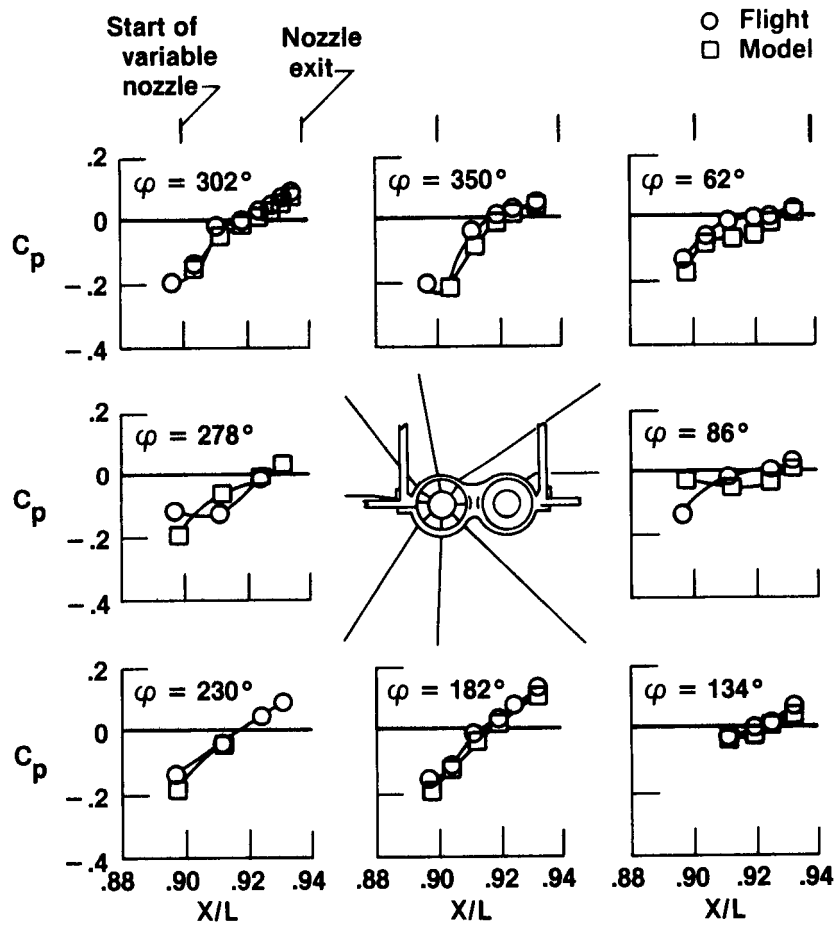
(b) $M_\infty \approx 0.6$; $BTL \approx 18.4$; $BTR \approx 18.4$ to $19.5°$; and $NPRL \approx 3.0$.

Figure 34. Continued.
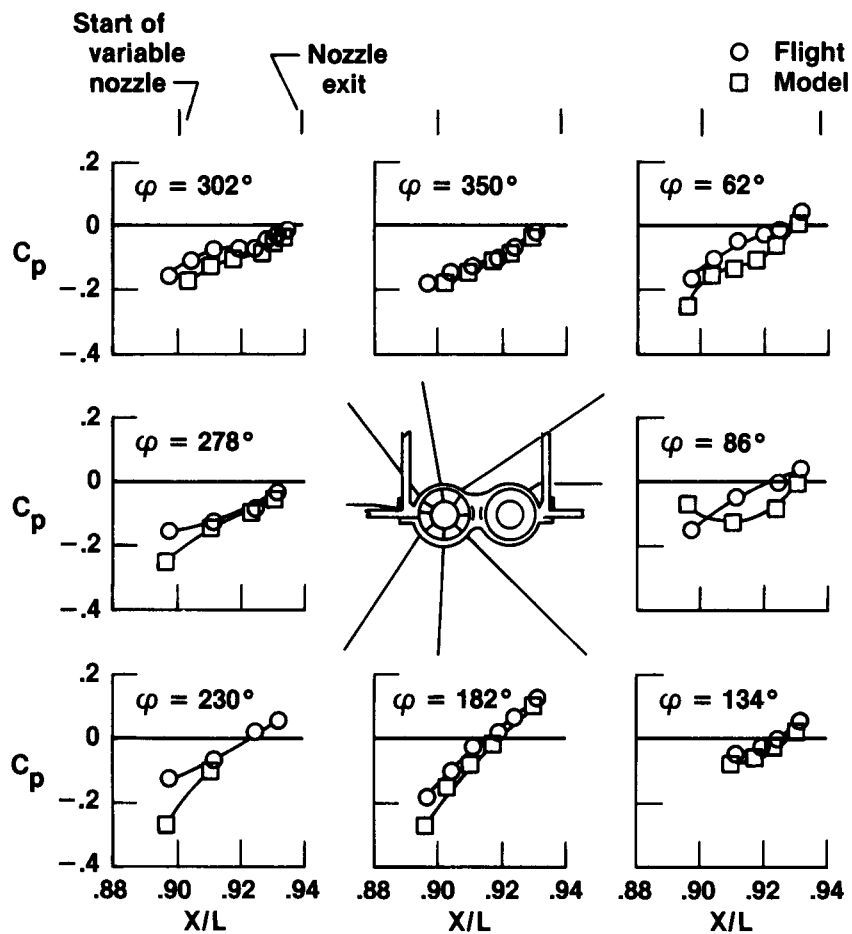
(c) $M_\infty \approx 0.9$; BTL $\approx 15.1°$; BTR $\approx 18.4°$ to $19.5°$; and NPRL ≈ 5.0.

Figure 34. Continued.

(d) $M_\infty \approx 0.9$; BTL $\approx 18.4°$; BTR ≈ 18.4 to $15.4°$; and NPRL ≈ 2.5 to 2.9.

Figure 34. Concluded.

○ Flight
□ Model
—— Fairing
— — Extrapolated
Solid symbol indicates
average value

.2

Last nozzle
orifice in
each row

C_p

0

−.2

First nozzle orifice
in each row

−.4

0   90   180   270   360

φ, deg

(a) $M_\infty \approx 0.6$; BTL $\approx 18.4°$; BTR $\approx 18.4°$ to
19.5°; and NPRL ≈ 2.7 to 3.0.

○ Flight
□ Model
—— Fairing
— — Extrapolated
Solid symbol indicates
average value

.2

Last nozzle orifice
in each row

C_p

0

−.2

First nozzle orifice
in each row

−.4

0   90   180   270   360

φ, deg

(b) $M_\infty \approx 0.8$; BTL $\approx 18.4°$; BTR $\approx 18.4°$ to
19.5°; and NPRL ≈ 2.5 to 3.0.

Figure 35.   Comparison of recompression on the
nozzle circumference as Mach number is varied
at $\alpha \approx 1°$ to 2°.

(c) $M_\infty \approx 0.9$; BTL $\approx 18.4°$; BTR $\approx 18.4°$ to 19.7°; and NPRL ≈ 2.5 to 3.0.
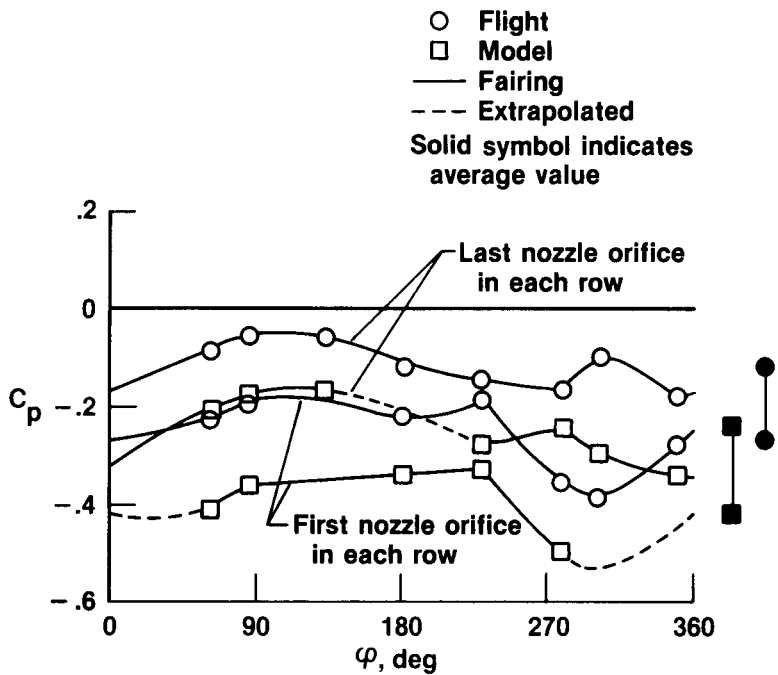
(d) $M_\infty \approx 1.2$; BTL $\approx 7.7°$; BTR $\approx 7.7°$; and NPRL $\approx 5.0°$.

Figure 35. Continued.

$$\Delta C_p = \left(C_{p_{avg}} \text{ at last orifice} \right) - \left(C_{p_{avg}} \text{ at first orifice} \right)$$
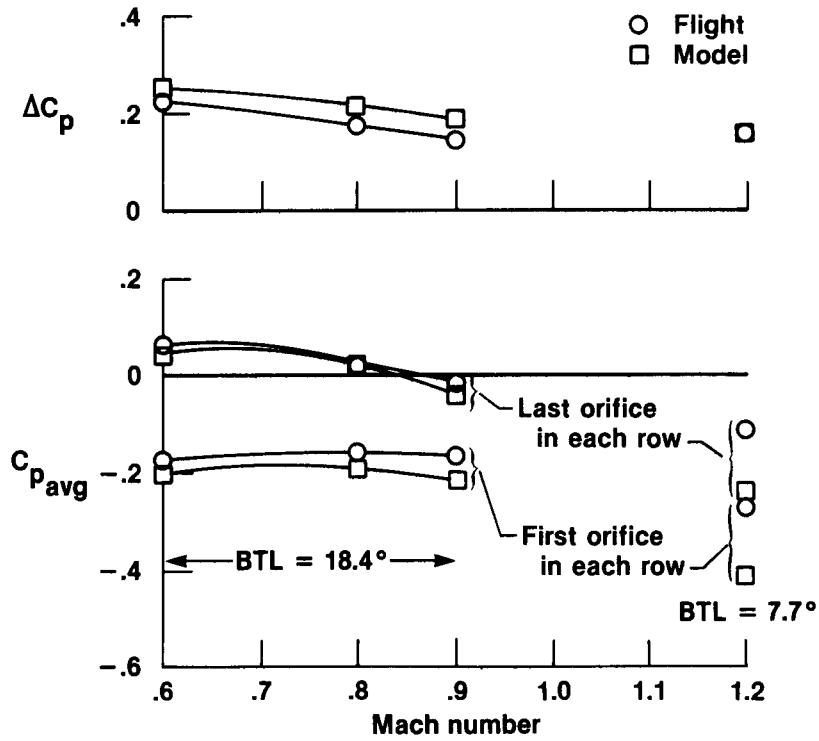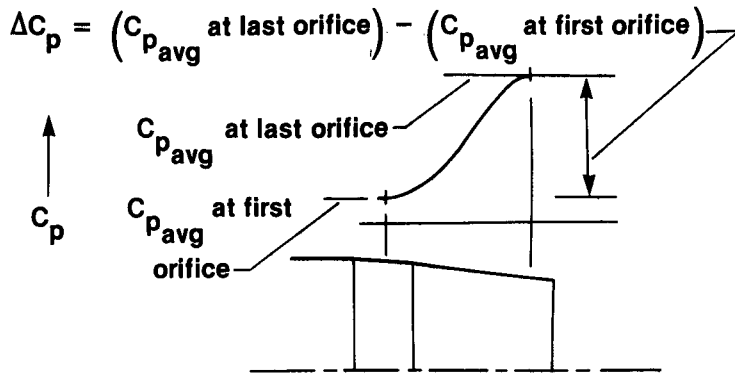
(e) Summary plot; BTL ≈ 18.4° and 7.7°; and
NPRL ≈ 2.0 to 5.0.

Figure 35. Concluded.

○ Flight
□ Model
Solid symbol indicates
average value

(a) $M_\infty \approx 0.6$; BTL $\approx 15.1°$; BTR $\approx 18.4°$ to
19.5°; and NPRL ≈ 4.0.

○ Flight
□ Model
Solid symbol indicates
average value
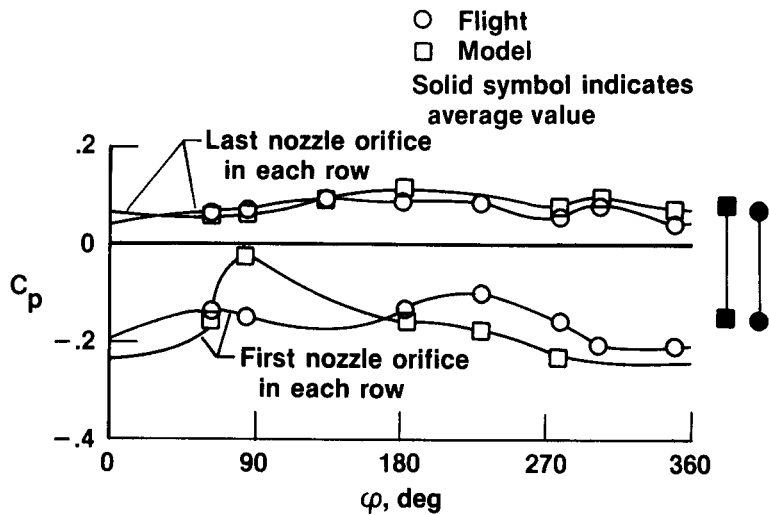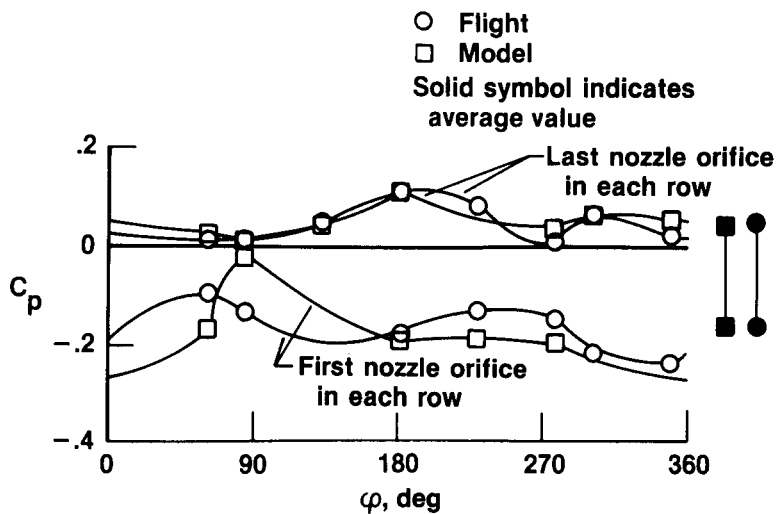
(b) $M_\infty \approx 0.6$; BTL $\approx 18.4°$; BTR $\approx 18.4°$ to
19.5°; and NPRL ≈ 3.0.

Figure 36. Comparison of recompression on the
nozzle circumference as the left nozzle boat-
tail angle is varied at $\alpha = 1°$ to $2°$.
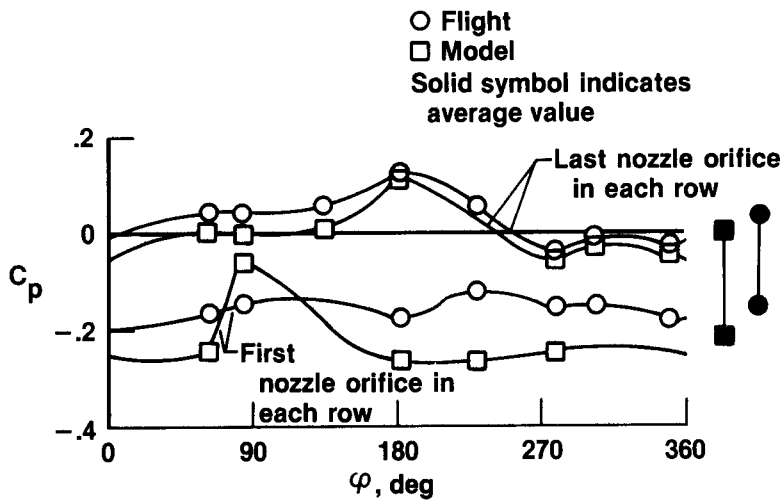
(c) $M_\infty \approx 0.9$; BTL $\approx 15.1°$; BTR $\approx 18.4°$ to 19.5°; and NPRL ≈ 5.0.
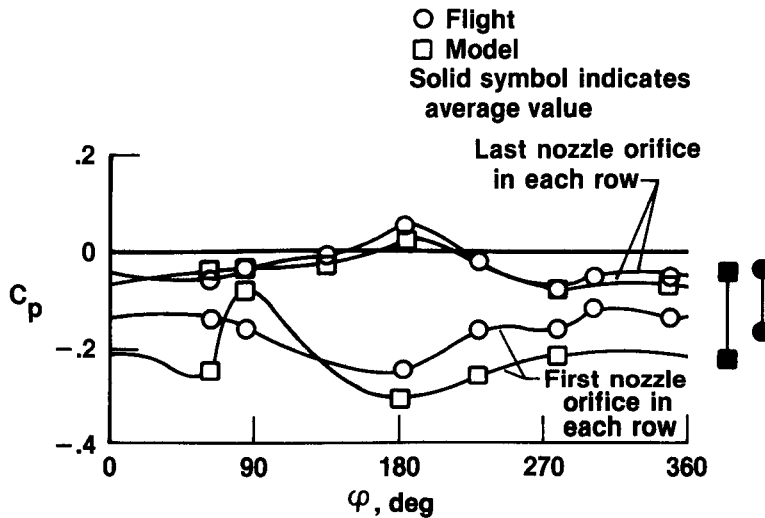
(d) $M_\infty \approx 0.9$; BTL $\approx 18.4°$; BTR $\approx 18.4°$ to 15.4°; and NPRL ≈ 2.5 to 2.9.

Figure 36. Concluded.
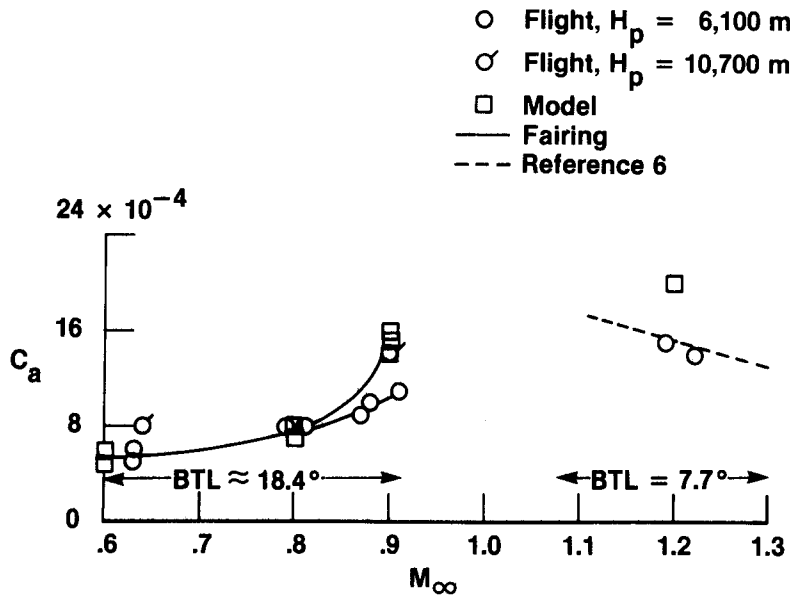
(a)   *Effect of Mach number.*
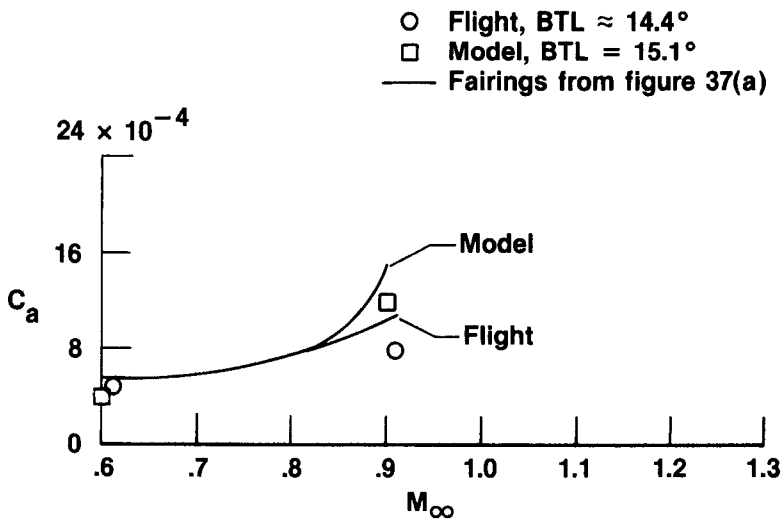
(b)   *Effect of left nozzle boattail angle.*

Figure 37.   Effect of Mach number and left nozzle boattail angle on the comparison of nozzle axial force coefficient at α ≈ 1° to 2° and NPRL ≈ 2.5 to 5.0.
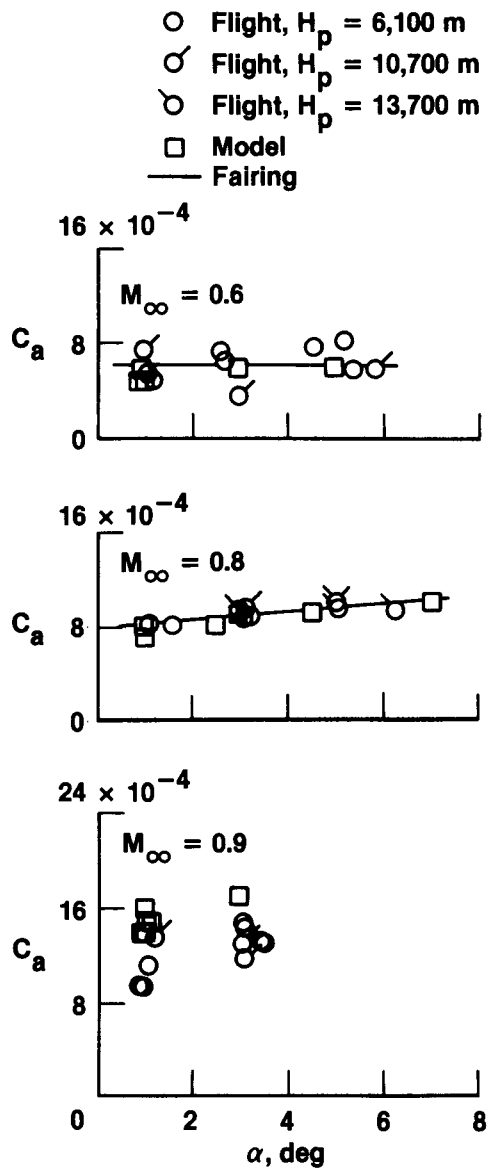
Figure 38. Effect of angle of
attack on the comparison of
nozzle axial force coefficient
at BTL ≈ 18.4° and NPRL ≈ 2.5
to 5.0.

O   Flight, H_p = 6,100 m

σ Flight, H_p = 10,700 m

□   Model

———   Fairing

❘   Design pressure ratio

Solid symbols indicate test
points for which jet
parameters are given

12×10^{-4}

C_a

T_a = 541 °K,

● MFRA = 1.25

8

4

T_m = 307 °K,
MFRM = 2.39

0   1   2   3   4   5

NPRL

(a) $M_\infty \approx 0.6$;   BTL $\approx 18.4°$.

O   Flight, H_p = 6,100 m

□   Model

———   Fairing

❘   Design pressure ratio

Solid symbols indicate test
points for which jet
parameters are given

16×10^{-4}

C_a

12

T_a = 580 °K,
MFRA = 1.04

8

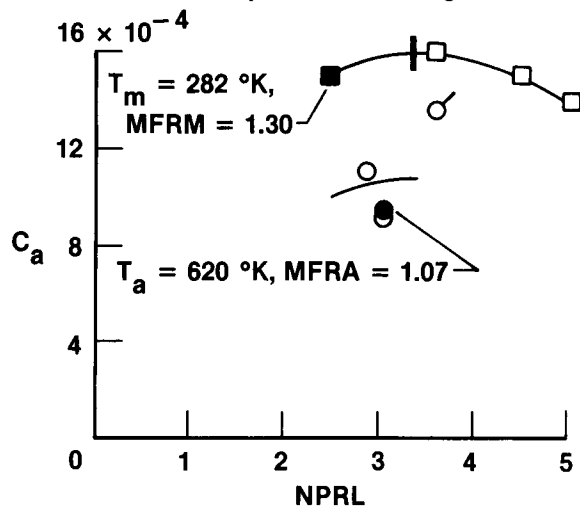T_m = 317 °K,
MFRM = 1.44

4

0   1   2   3   4   5

NPRL
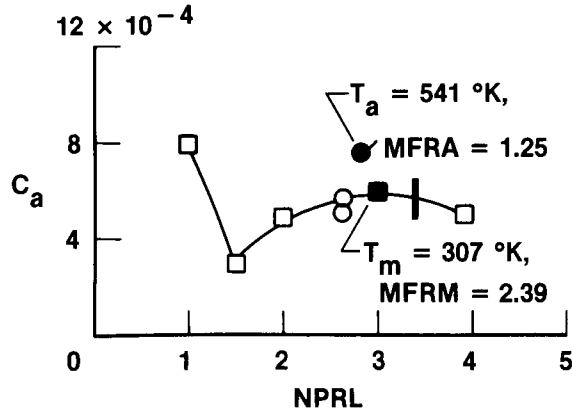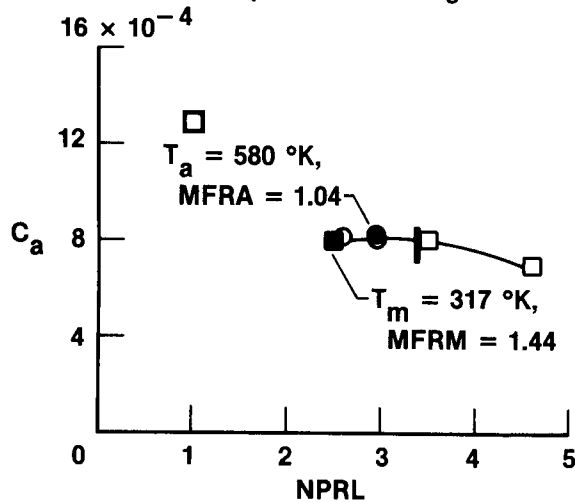
(b) $M_\infty \approx 0.8$;   BTL $\approx 18.4°$.

Figure 39.   Effect of nozzle pressure ratio on the comparison of nozzle axial force coefficient at $\alpha \approx 1°$ to 2°.

16×10^{-4}

T_m = 282 °K,
MFRM = 1.30

C_a

T_a = 620 °K, MFRA = 1.07

(c) $M_\infty \approx 0.9$;   *BTL* $\approx 18.4°$.
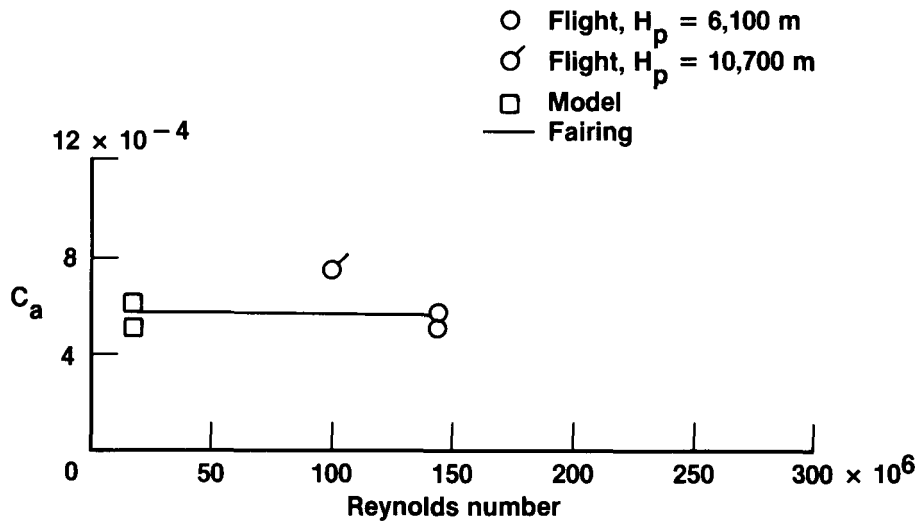
O   Flight, H_p = 6,100 m

□   Model

—— Fairing

| Design pressure ratio

Solid symbols indicate test
points for which jet
parameters are given
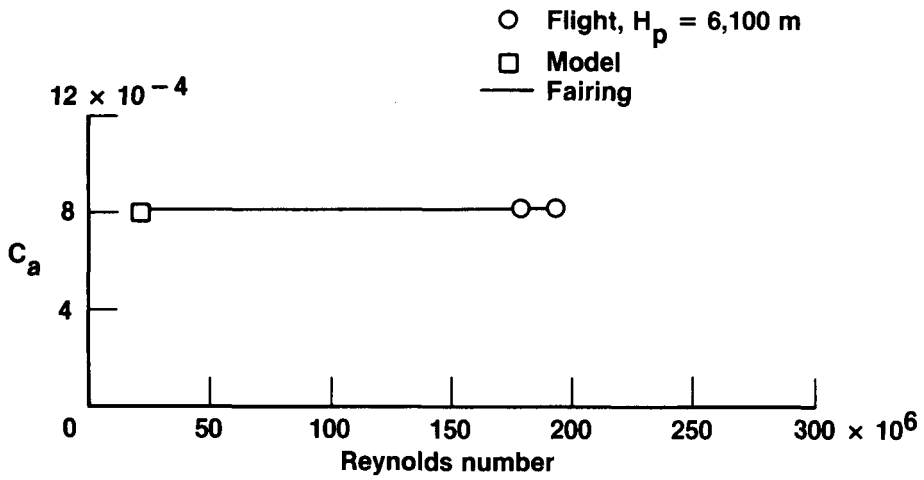
24×10^{-4}

C_a

T_m = 298 °K, MFRM = 1.44

T_a = 1824 °K, MFRA = 0.54
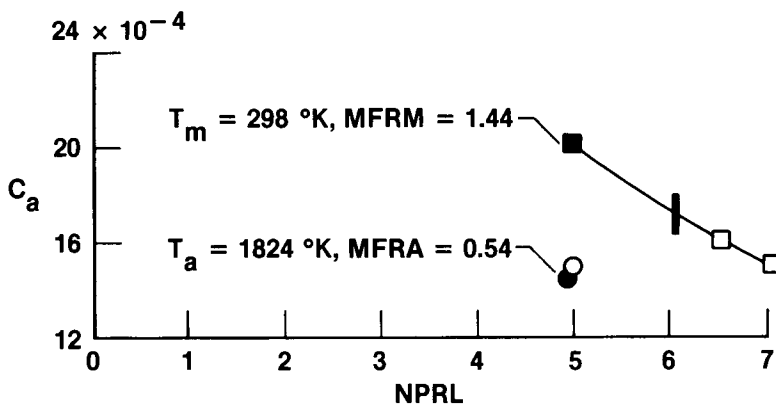
(d) $M_\infty \approx 1.2$;   *BTL* $\approx 7.7°$.

Figure 39. Concluded.
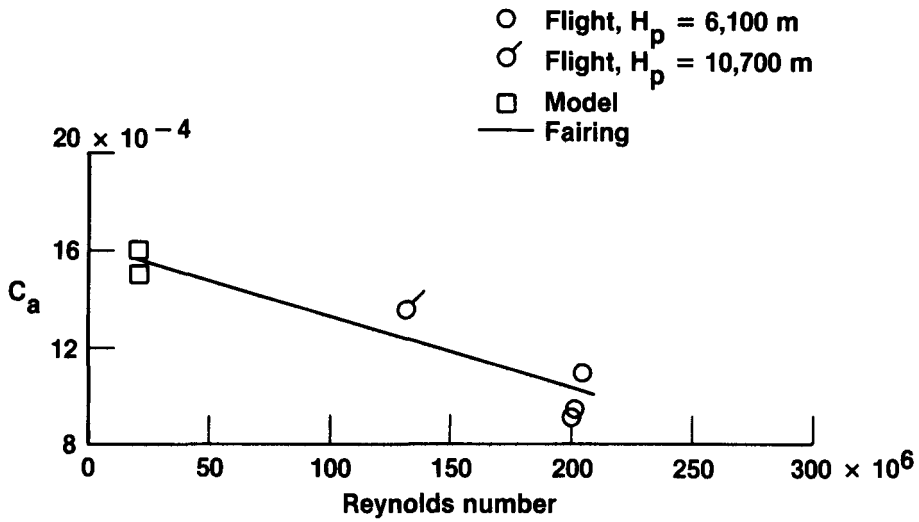
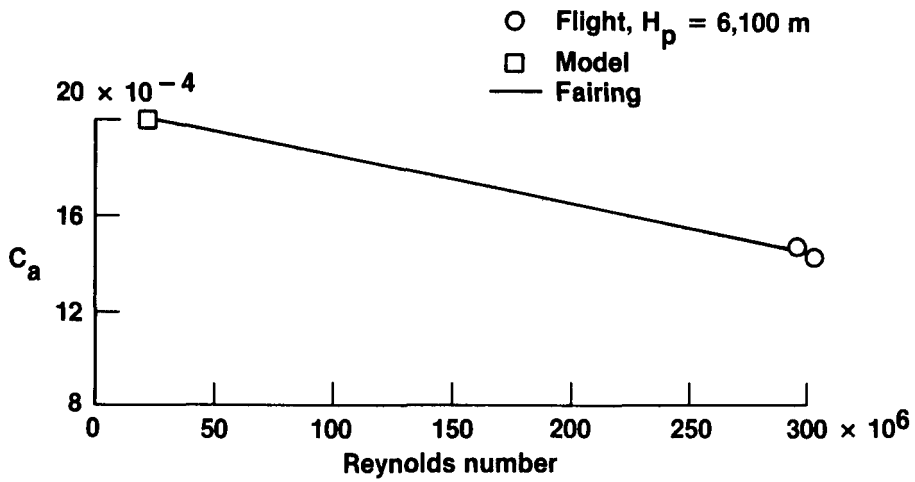(a) $M_\infty \approx 0.6$; BTL $\approx 18.4°$; and NRPL ≈ 2.0 to 3.0.

(b) $M_\infty \approx 0.8$; BTL $\approx 18.4°$; and NPRL ≈ 2.5 to 3.5.

Figure 40. Effect of Reynolds number on nozzle axial force coefficient at $\alpha \approx 1°$ to $2°$.

(c) $M_\infty \approx 0.9$; BTL $\approx 18.4°$; and NPRL ≈ 2.5 to 3.6.

(d) $M_\infty \approx 1.2$; BTL $\approx 7.7°$; and NPRL $= 5.0$.
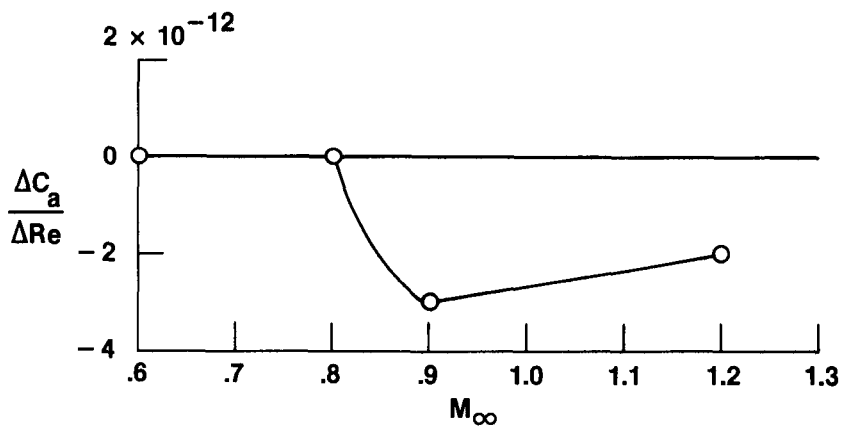
Figure 40. Concluded.

Figure 41. Effect of Mach number on the rate of change of nozzle axial force coefficient with Reynolds number.

1. Report No. NASA TP-2588	2. Government Accession No.	3. Recipient's Catalog No.
4. Title and Subtitle Comparison of Wind Tunnel and Flight Test Afterbody and Nozzle Pressures for a Twin-Jet Fighter Aircraft at Transonic Speeds		5. Report Date MARCH 1987
		6. Performing Organization Code
7. Author(s) Jack Nugent and Odis C. Pendergraft, Jr.		8. Performing Organization Report No. H-1214
		10. Work Unit No. RTOP 533-02-21
9. Performing Organization Name and Address NASA Ames Research Center Dryden Flight Research Facility P.O. Box 273 Edwards, CA 93523-5000		
		11. Contract or Grant No.
		13. Type of Report and Period Covered Technical Paper
12. Sponsoring Agency Name and Address National Aeronautics and Space Administration Washington, D.C. 20546		
		14. Sponsoring Agency Code

15. Supplementary Notes

Odis C. Pendergraft, Jr., is affiliated with NASA Langley Research Center, Hampton, Virginia.

16. Abstract

Afterbody and nozzle pressures measured on a 1/12-scale model and in flight on a twin-jet fighter aircraft were compared as Mach number varied from 0.6 to 1.2, Reynolds number varied from 17.5 million to 302.5 million, and angle of attack varied from 1° to 7°.

At Mach 0.6 and 0.8, nozzle pressure coefficient distributions and nozzle axial force coefficients agreed and showed good recompression.

At Mach 0.9 and 1.2, flow complexity caused a loss in recompression for both flight and wind tunnel nozzle data. The flight data exhibited less negative values of pressure coefficient and lower axial force coefficients than did the wind tunnel data. Reynolds number effects were noted only at these Mach numbers. Jet temperature and mass flux ratio did not affect the comparisons of nozzle axial force coefficient.

At subsonic speeds, the levels of pressure coefficient distributions on the upper fuselage and lower nacelle surfaces for flight were less negative than those for the model.

The model boundary layer thickness at the aft rake station exceeded that for the forward rake station and increased with increasing angle of attack. The flight boundary layer thickness at the aft rake station was less than that for the forward rake station and decreased with increasing angle of attack.

17. Key Words (Suggested by Author(s)) Nozzle-afterbody flow interactions Reynolds number effects Wind tunnel and flight comparison	18. Distribution Statement Unclassified — Unlimited Subject category 02

19. Security Classif. (of this report) Unclassified	20. Security Classif. (of this page) Unclassified	21. No. of Pages 124	22. Price* A06